UNIVERSITÉ DU QUÉBEC À TROIS-RIVIÈRES

UTILISATION DE MÉTHODES GÉOPHYSIQUES ET DE TÉLÉDÉTECTION POUR EXPLORER LES RELATIONS SPATIALES ENTRE LES CONDITIONS DU COUVERT DE GLACE ET LA VÉGÉTATION AQUATIQUE SUBMERGÉE AU LAC SAINT-PIERRE

MÉMOIRE PRÉSENTÉ

COMME EXIGENCE PARTIELLE DE LA

MAÎTRISE EN SCIENCES DE L'ENVIRONNEMENT

PAR

DAVE MONGRAIN

AOÛT 2026

Université du Québec à Trois-Rivières

Service de la bibliothèque

Avertissement

L'auteur de ce mémoire, de cette thèse ou de cet essai a autorisé l'Université du Québec à Trois-Rivières à diffuser, à des fins non lucratives, une copie de son mémoire, de sa thèse ou de son essai.

Cette diffusion n'entraîne pas une renonciation de la part de l'auteur à ses droits de propriété intellectuelle, incluant le droit d'auteur, sur ce mémoire, cette thèse ou cet essai. Notamment, la reproduction ou la publication de la totalité ou d'une partie importante de ce mémoire, de cette thèse et de son essai requiert son autorisation.

UNIVERSITÉ DU QUÉBEC À TROIS-RIVIÈRES

MAÎTRISE EN SCIENCES DE L'ENVIRONNEMENT (M. Sc.)

Direction de recherche :

Christophe Kinnard, Ph. D. — Université du Québec à Trois-Rivières (UQTR)
Directeur de recherche

Andrea Bertolo, Ph. D. — Université du Québec à Trois-Rivières (UQTR)
Codirecteur de recherche

Jury d'évaluation :

Christophe Kinnard, Ph. D. — Université du Québec à Trois-Rivières (UQTR)
Directeur de recherche

Alexandre Roy, Ph. D. — Université du Québec à Trois-Rivières (UQTR)
Évaluateur

Saeid Homayouni, Ph. D. — Institut national de la recherche scientifique (INRS)
Évaluateur

Dépôt final : 17 août 2026

REMERCIEMENTS

La réalisation de ce mémoire n'aurait pas été possible sans le soutien et la contribution de nombreuses personnes.

Je tiens d'abord à remercier mon directeur de recherche, Christophe Kinnard, ainsi que mon codirecteur, Andrea Bertolo, professeurs au département des sciences de l'environnement de l'Université du Québec à Trois-Rivières, pour m'avoir offert l'opportunité de travailler sur ce projet. Je leur suis reconnaissant pour leurs nombreux conseils, leurs encouragements et leur patience tout au long de mon cheminement.

J'aimerais aussi remercier les membres de mon comité d'encadrement, Alexandre Roy et Stéphane Campeau, professeurs au même département. Merci à Alexandre de m'avoir recommandé ce projet, et particulièrement à Stéphane de m'avoir initié à la recherche et pour son accompagnement depuis mon baccalauréat en géographie.

Je remercie également mes collègues et amis du Glaciolab, du Remote-Nord et des autres labos pour leurs idées et leur soutien. Merci à Rodrigo et Arthur pour les échanges autour de nos projets connexes, ainsi qu'à Charlotte, Gabrielle et David pour leur soutien moral.

Merci aux membres du volet « sciences participatives » du regroupement « Mon pays c'est l'hiver », dans lequel s'inscrit ce projet financé par le Réseau Québec maritime (RQM) et le Réseau inondations intersectoriel du Québec (RIISQ), pour leur contribution.

Ce projet a bénéficié du soutien logistique et technique de l'Institut national de la recherche scientifique (INRS) et du ministère de l'Environnement, de la Lutte contre les changements climatiques, de la Faune et des Parcs (MELCCFP). Je remercie Erwan Gloaguen, Saeid Homayouni et Jimmy Poulin de l'INRS, ainsi que Martin Laporte, Rémy Pouliot, Philippe Brodeur, Marie-Josée Gagnon, Guillaume Canac-Marquis et Thierry Gariépy du MELCCFP pour leur expertise et leur aide précieuse.

Merci aux professionnels du RIVE, notamment Chantal Fournier et Pierre-André Bordeleau, ainsi qu'à Catarina Leote Franco Pio pour leur soutien technique et administratif.

Enfin, j'aimerais remercier ma famille et ma copine Angélique pour leur soutien, ainsi que Gros Chat pour sa présence réconfortante lors de la rédaction.

RÉSUMÉ

La végétation aquatique submergée (VAS) constitue un habitat essentiel pour les poissons et assure de nombreuses fonctions écologiques dans les écosystèmes aquatiques. Au lac Saint-Pierre, plus grand lac de plaine inondable du fleuve Saint-Laurent (Québec, Canada), les habitats de VAS, menacés par des pressions en provenance du bassin versant pendant la saison estivale, ont vu leur superficie diminuer considérablement au cours des dernières décennies. La variabilité spatiale du couvert de glace hivernal, par ses effets physiques et physiologiques potentiels sur la VAS, a été évoquée comme facteur additionnel de ce déclin. Cette étude vise à déterminer si les conditions du couvert de glace (épaisseur et durée) sont associées à des changements interannuels de la répartition de la VAS, et dans quelle mesure la profondeur de l'eau, un facteur commun à l'épaississement de la glace et à la croissance de la VAS, influence cette association en modulant l'espace libre sous la glace. Le biovolume de la VAS, défini comme la proportion de la colonne d'eau qu'elle occupe, a été cartographié à l'aide de relevés hydroacoustiques réalisés aux étés 2021 et 2022, tandis que l'épaisseur de glace et la durée d'englacement ont été cartographiées au moyen d'un géoradar et d'images satellitaires Sentinel-2 pendant l'hiver 2022. Des modèles de régression par forêts aléatoires ont été entraînés afin de tester la capacité des variables cryosphériques et de la profondeur de l'eau à prédire la variation interannuelle du biovolume de la VAS (ΔBIOV) entre 2021 et 2022, à une résolution spatiale de 20 m. La durée d'englacement a été la variable la plus négativement associée à ΔBIOV, tandis que l'épaisseur de glace n'y a été que faiblement associée, et seulement dans les zones peu profondes ; comme pour la profondeur d'eau, cette association n'a pas été généralisable spatialement lorsque le prédicteur a été considéré seul. Les prédicteurs cryosphériques ont en partie agi comme des proxys du gradient hydro-morphologique (profondeur d'eau et conditions d'écoulement), et le dispositif sur deux ans n'a pas permis de distinguer un effet hivernal différé des facteurs concomitants non modélisés de la saison de croissance, notamment la crue printanière. La contribution des conditions du couvert de glace au déclin de la VAS ne peut donc être que partiellement établie. Néanmoins, cette étude offre une première exploration des effets physiques et physiologiques potentiels du couvert de glace sur la VAS.

Mots-clés : végétation aquatique submergée ; biovolume ; lac Saint-Pierre ; couvert de glace lacustre ; géoradar ; modèle de forêts aléatoires

TABLE DES MATIÈRES

REMERCIEMENTS ..... **III**
RÉSUMÉ ..... **IV**
LISTE DES TABLEAUX ..... **VII**
LISTE DES FIGURES ..... **VIII**
CHAPITRE I **1**
INTRODUCTION GÉNÉRALE **1**
1.1 Mise en contexte **1**
1.1.1 Les macrophytes et leurs rôles écologiques 1
1.1.2 Le lac Saint-Pierre 2
1.1.3 Déclin de la VAS et répercussions trophiques 3
1.1.4 Facteurs déterminant la distribution estivale de la VAS 4
1.1.5 Le rôle des processus hivernaux 5
1.2 Problématique **7**
1.3 Objectifs, hypothèses et cadre analytique **10**
CHAPITRE II **14**
USING GEOPHYSICAL AND REMOTE SENSING METHODS TO EXPLORE THE SPATIAL RELATIONSHIPS BETWEEN ICE COVER CONDITIONS AND SUBMERGED AQUATIC VEGETATION IN A SHALLOW FLUVIAL LAKE **14**
Abstract **14**
2.1 Introduction **15**
2.2 Methods **22**
2.2.1 Study area 22
2.2.2 Mapping interannual SAV biovolume change 23
2.2.3 Mapping ice thickness 24
2.2.4 Mapping water depth 27
2.2.5 Mapping ice cover duration 27
2.2.6 Mapping under-ice clearance 30
2.2.7 Statistical analyses 30
2.3 Results **32**
2.3.1 Borehole observations 32
2.3.2 Kriging cross-validation and prediction uncertainty for ice thickness and water depth 33
2.3.3 Ice cover phenology and classification accuracy 34

2.3.4 Spatial variability of ΔBIOV and explanatory variables 36
2.3.5 Pairwise predictor relationships and collinearity 38
2.3.6 Random Forest regression models 39
2.3.7 Predictor variable importance and variation partitioning 40
2.3.8 Modeled responses of ΔBIOV and interactions among predictors 42

2.4 Discussion 46

2.4.1 Spatial datasets: reliability of hydroacoustic, GPR, and satellite sources 46
2.4.2 Conditional effects of ice thickness on SAV biovolume change 49
2.4.3 Ice cover duration and concurrent growing-season drivers of SAV 52

2.5 Conclusion 54

2.6 Supplementary Material 56

CHAPITRE III 64

CONCLUSION GÉNÉRALE 64

3.1 Retour sur la démarche et les principaux résultats 64

3.2 Retombées et perspectives 66

RÉFÉRENCES 68

LISTE DES TABLEAUX

Table **Page**

2.1. Validation metrics for THK and WD. LOOCV: leave-one-out cross-validation; BH: boreholes (n = 36); CHS: Canadian Hydrographic Service bathymetry (n = 6716)..... 34

2.2. Prediction performance metrics from out-of-bag (OOB) validation (R^2 and RMSE) and spatial block cross-validation (Block CV; R^2 and r^2) for random forest regression models of ΔBIOV. R^2 is the coefficient of determination and r^2 is the squared correlation coefficient 39

S1. Sentinel-2 scenes acquisition summary and per-class counts used for validation of ice-cover classification through confusion matrices 61

S2. Per-scene classification performance on independent validation samples. OA: overall accuracy, K: kappa coefficient, PA: Producer's accuracy, UA: User accuracy 62

S3. Threshold values of daily ice cover fraction (%) used to define lake ice phenological phases at Lake Saint-Pierre, based on the methodology proposed by Yang et al. (2019) 63

LISTE DES FIGURES

Figure **Page**

1.1. Répartition théorique des groupes fonctionnels des macrophytes le long d'un gradient éco-morphologique en zone littorale. Adaptée de Gratton et Dubreuil (1990) et Hudon et al. (2018)..... 1

2.1. Location of the study site in the southwestern portion of LSP. (a) Location of LSP within the St. Lawrence River in southern Québec, Canada (blue star and rectangle). Main tributaries within the map extent include MASK (Maskinongé River), LOUP (du Loup River), YAMA (Yamachiche River), NICO (Nicolet River), STFR (Saint-François River), and YSKA (Yamaska River). Symbols indicate the hydrometric (ID 15975) and climate stations (IDs 7026043, 701LP0N) as purple stars; ice monitoring stations (C1–C3) as red triangles; and ice management structures (booms, stabilization islets, and the navigation channel) as green lines and orange icons. (b) Site covered by the hydroacoustic and GPR surveys (in red), with GPR transects (black lines) and ice borehole observation sites (yellow dots). Boreholes are labeled by grid position (e.g., 6B); TA, TB, and TC indicate additional boreholes between grid lines. The Tardif channel is also shown. Hydroacoustic transects were omitted for clarity (cf. Section 2.2.2). Basemap: Copernicus Sentinel-2 true-color imagery, January 20, 2022 23

2.2. Spatial distribution of photo-interpreted training samples grouped by class. (a) Distribution of training samples for a model scene. Frozen wetlands are shown in gray. Tones and spatial patterns of the surrounding pixels for training samples assigned to the (b) ice, (c) ice floes, and (d) water classes. Basemap: Copernicus Sentinel-2 true-color imagery, January 20, 2022..... 29

2.3. Borehole ice stratigraphy and snow thickness. Site IDs on the x axis are ordered by their group position from the shoreline, from farthest (1) to closest (6) along or off transects (letters) (see Figure 2.1b for site locations). Drilling dates are shown at the base of each bar (black symbols): February 14 (square); February 15 (diamond); February 21 (triangle). Under-ice SAV presence is marked above the latter (blue symbols): observed (filled circle); not observed (open circle); lakebed not visible (cross) 33

2.4. Prediction standard error rasters for the interpolated explanatory variables. (a) ice thickness (THK); (b) water depth (WD) 34

2.5. Ice cover phenology and classification accuracy. (a) Lake ice fraction from classified images (n = 24; white dots). CCG ice management activities are indicated by symbols (lake-wide icebreaking: diamond; navigation channel clearing: triangle; ice reconnaissance patrol: square). (b) Overall accuracy (black dots) and kappa coefficient (blue dots) calculated against each scene's validation samples. Phenological cycle phases (annotations) are displayed above both panels. Dashed lines indicate freeze-up (FUS, FUE) and break-up (BUS, BUE); arrows denote transition (FUD, BUD) and frozen durations (FD, CFD) 35

2.6. Rasters of ΔBIOV and the potential explanatory variables investigated. (a) ΔBIOV, i.e., the difference between interpolated values from 2022 and 2021; (b) ice thickness (THK); (c) water depth (WD); (d) ice cover duration (ICD); (e) under-ice clearance (UIC); (f) field photo of the longitudinal crack, also displayed in panel (b). The red outline delineates the ΔBIOV analysis extent (n = 56,171 grid cells); cells outside were excluded 37

2.7. Pairwise correlation matrix and variable distributions. Histograms are displayed on the diagonal panels, density scatterplots with trends on the lower panels (blue to red: low to high dot density), and Spearman's rank correlation coefficients on the upper panels. Red asterisk: response variable; blue asterisk: potential predictors 38

2.8. Permutation-based variable importance for the multivariate random forest regression models. Relative importance values were rescaled on a 0–1 range, where higher values implied more influence of a predictor within a given model. Predictors (colors) not included in a model are shown as crosses. These values should be interpreted cautiously, as partial collinearity among predictors may distort relative importance 40

2.9. Proportions of variation of ΔBIOV. Fractions [a], [b], and [c] are the variation explained exclusively by THK, WD, and ICD, respectively. Fractions [d]–[f] are the shared variation between each predictor pair, and fraction [g] is the shared variation among all three predictors. Fraction [h] is the variation unexplained by the predictors..... 41

2.10. Partial dependence plots for ΔBIOV by predictor (columns, colors) from the multivariate models M1, M2, and M3 (rows). (a, d): THK; (b, e, f): WD; (c, g): ICD; The horizontal dashed line serves as a visual reference where ΔBIOV = 0. Predictors not included in a model are shown as crosses. PDPs were computed with the full range of each predictor's values shown in Figure 2.6; however, in the present figure, the y-axis limits were fixed to match the common range of marginal effects, while the ICD x-axis tick labels were rounded for visual clarity 42

2.11. Response curves for ΔBIOV by predictor (columns, colors) from the univariate models U1, U2, and U3. (a) THK; (b) WD; (c) ICD. Axis scales and tick values are identical to those in Figure 2.10 for comparison between multivariate and univariate model responses 44

2.12. Two-dimensional partial dependence plots of the modeled interactions between predictors and their effect on ΔBIOV (colors) from the multivariate model M1. (a) THK and WD; (b) ICD and WD. Partial dependence was computed over a 100 × 100 predictor grid 45

S1. Hydroclimatic conditions over each survey year. (a) 2020-2021; (b) 2021-2022. Mean air temperature (gray line), total rainfall (orange bars), total snowfall (light blue bars), and water level (dark blue line), all daily. Vertical green dashed lines indicate summer fieldwork dates. Vertical gray dashed lines in (b) indicate winter fieldwork dates, and vertical blue dashed lines delimit the ice season. Air temperature data: LSP station (ID 701LP0N); precipitation data: Pierreville station (ID 7026043); water level data: LSP hydrometric station (ID 15975) 56

S2. Wind roses with wind direction frequency (% per 30° sector) and wind speed classes (m s^{-1}; upper bound included, note the wider upper class) from November 2021 to April 2022 (ice season). Panels (a)–(f) correspond to individual months, while panel (g) is the full ice season. The inset table reports the monthly mean wind direction (°). All data are from hourly records at the LSP climate station (ID 701LP0N; Environment Canada)..... 57

S3. Location of SAV survey transects in the southwestern portion of LSP. Basemap: Copernicus Sentinel-2 true-color imagery, November 11, 2021 58

S4. Independent validation scatterplot of kriging predicted water depth (m), adjusted to daily water levels, against water depth measured at borehole locations during winter fieldwork (n=36). The 1:1 identity line (blue) and the regression line (black) are shown. Y: Regression equation; R^2: coefficient of determination; RMSE: Root mean square error; and MAE: Mean absolute error..... 58

S5. Leave-one-out cross-validation scatterplot of kriging predicted ice thickness (m) against ice thickness measured at borehole locations (n=36). The 1:1 identity line (blue) and the regression line (black) are shown. Y: Regression equation; R^2: coefficient of determination; RMSE: Root mean square error; and MAE: Mean absolute error 59

S6. Two-dimensional partial dependence plot of the modeled interaction between ICD and THK and its effect on ΔBIOV (colors), computed from M1 60

S7. Two-dimensional partial dependence plot of the modeled interaction between THK and WD and its effect on ΔBIOV (colors), computed from M2..... 60

CHAPITRE I

INTRODUCTION GÉNÉRALE

1.1 Mise en contexte

1.1.1 Les macrophytes et leurs rôles écologiques

Les macrophytes constituent une composante écologique essentielle des écosystèmes aquatiques peu profonds (e.g., Thomaz et al., 2025). Ces organismes photosynthétiques, visibles à l'œil nu, regroupent les angiospermes (i.e., plantes vasculaires à graines et à fleurs), certaines fougères, les bryophytes (i.e., mousses) et des algues (Chambers et al., 2008). Par exemple, en zone littorale fluviale, leur répartition suit un gradient éco-morphologique qui se divise en trois groupes fonctionnels (Figure 1.1), définis selon leur position par rapport à la rive et leur relation avec le substrat (Barbe, 1984). Les hélophytes colonisent les berges et les marais, tandis que les amphiphytes tolèrent une submersion partielle ou prolongée. Les hydrophytes, qui regroupent l'essentiel de la végétation aquatique submergée (VAS) ou flottante, s'organisent en mosaïques mono- ou plurispécifiques (syn. herbiers).

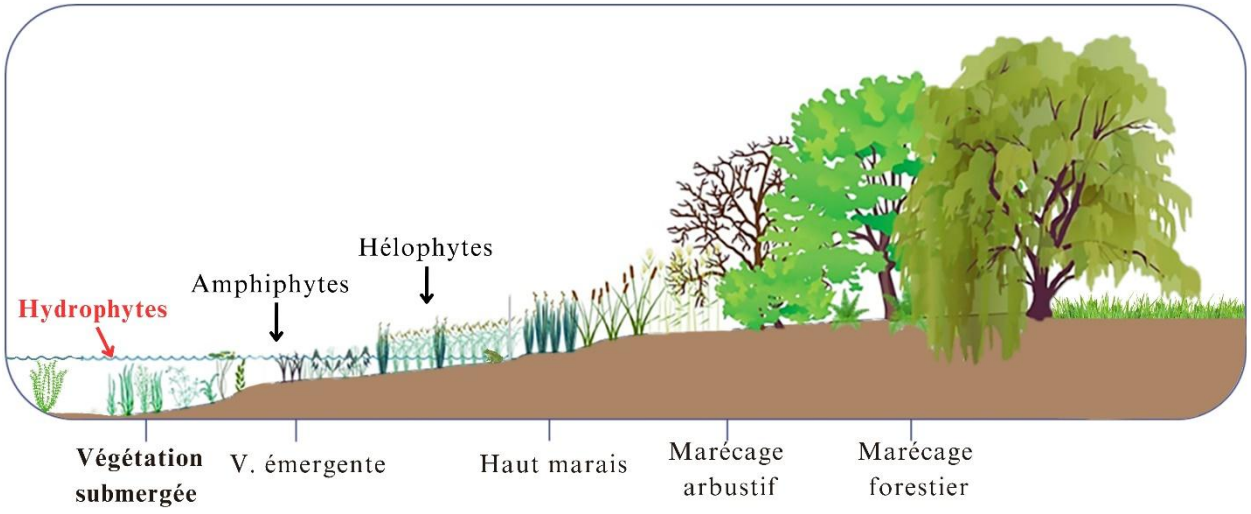


Figure 1.1. *Répartition théorique des groupes fonctionnels des macrophytes le long d'un gradient éco-morphologique en zone littorale. Adaptée de Gratton et Dubreuil (1990) et Hudon et al. (2018).*

En tant que producteurs primaires, les macrophytes développent une biomasse enracinée ou en suspension dans la colonne d'eau, qui soutient le fonctionnement des écosystèmes (Chambers et al., 2008; Schneider et al., 2012). En réduisant la vitesse du courant, cette biomasse favorise la sédimentation intra-herbier et améliore la transparence de l'eau (Vermaat et al., 2000; Madsen et al., 2001; Cornacchia et al., 2020). Elle participe également aux cycles biogéochimiques en régulant les flux d'azote, de phosphore, de carbone et d'oxygène, par photosynthèse et transferts passifs ou actifs, agissant comme biofiltre (Marion et Paillisson, 2003; Binzer et al., 2006; Newete et Byrne, 2016). En parallèle, elle occupe une interface trophique majeure, en tant qu'habitat structurant et ressource alimentaire pour de nombreuses espèces, notamment les invertébrés, les poissons, les oiseaux aquatiques et les organismes épiphytes (Lodge, 1991; Newman, 1991; Lauridsen et Lodge, 1996; Rudstam et al., 2004).

1.1.2 Le lac Saint-Pierre

L'importance écologique des macrophytes se manifeste de façon marquée dans les milieux fluviaux, à l'image du lac Saint-Pierre (LSP). Situé entre Sorel-Tracy et Trois-Rivières, le LSP représente le plus grand élargissement fluvial du Saint-Laurent avant son estuaire. Désigné site Ramsar en 1998 et réserve de biosphère de l'UNESCO en 2000, le LSP abrite une mosaïque d'habitats (e.g., chenaux, fosses, marais) interconnectés couvrant 197 km^2 de milieux humides contigus (Hudon et al., 2018). Ces milieux soutiennent 288 espèces d'oiseaux et constituent la plus importante halte migratoire de la sauvagine du Canada (MDDEFP, 2013). Ils accueillent également 79 espèces de poissons, incluant la perchaude (*Perca flavescens*), espèce autrefois abondante et emblématique des pêcheries locales (Hudon et al., 2018; Magnan et al., 2022).

Cependant, cette richesse écologique s'inscrit dans un contexte de pressions croissantes. Le bassin versant du LSP couvre environ 990 000 km^2, répartis entre les États-Unis (58 %), l'Ontario (28 %) et le Québec (14 %) (MDDEFP, 2013). En territoire québécois, ce bassin versant regroupe près de six millions d'habitants et subit les effets conjugués de l'agriculture intensive, des rejets domestiques et industriels, de la navigation commerciale, des espèces exotiques envahissantes et des changements climatiques (Hudon et Carignan, 2008; Marcogliese et al., 2015; Hudon et al., 2018). L'apport de nutriments d'origine diffuse (e.g., phosphates et nitrates), issus de l'érosion des sols et du ruissellement agricole, stimule la croissance des macrophytes (Duarte, 1995). Toutefois, en excès, ces apports favorisent la prolifération du phytoplancton et des cyanobactéries benthiques

(*Lyngbya wollei*), ce qui accroît la turbidité et la compétition pour la lumière (Vis et al., 2008; Hudon et al., 2012; Søndergaard et al., 2017). En complément, la matière organique dissoute, d'origine allochtone (e.g., affluents forestiers, effluents municipaux) ou autochtone (e.g., sénescence et décomposition des macrophytes), contribue à la tannisation et à la coloration des eaux (Frenette et al., 2003; Vis et al., 2007). Selon Laporte et al. (2023), la détérioration des conditions optiques de la colonne d'eau par une diminution de la transparence compromet progressivement la capacité de colonisation en profondeur des herbiers dominés par la vallisnérie d'Amérique (*Vallisneria americana*) et le potamot de Richardson (*Potamogeton richardsonii*). Une tendance similaire a été documentée dans des lacs à l'échelle mondiale par Botrel et Maranger (2023), qui rapportent une diminution de la VAS dans 41 % des cas analysés, souvent en réponse à l'eutrophisation. Selon les mêmes auteurs, le portrait s'avère plus contrasté en Amérique du Nord, avec la prolifération d'espèces exotiques envahissantes, comme le myriophylle à épis (*Myriophyllum spicatum*).

1.1.3 Déclin de la VAS et répercussions trophiques

Depuis les années 1990, le déclin de la VAS au LSP engendre des répercussions en cascade sur les niveaux trophiques supérieurs (Giacomazzo et al., 2020). Malgré l'application préalable de quotas et de tailles minimales légales (Magnan, 2002), l'effondrement du stock de perchaude, attribuable à un recrutement juvénile insuffisant, a motivé l'instauration d'un moratoire sur les pêches commerciale et sportive, en vigueur depuis 2012 et prolongé jusqu'en 2027 (Magnan et al., 2022). Selon Giacomazzo et al. (2020), la diminution des débarquements de perchaude s'explique en partie par une réduction de l'abondance de la VAS. En parallèle, la perte de connectivité hydrologique, les variations du niveau d'eau et la prédation par le cormoran à aigrettes (*Nannopterum auritum*) exercent une pression supplémentaire sur les habitats disponibles et les populations (de la Chenelière et al., 2014; Magnan et al., 2017; Hudon et al., 2018; Magnan et al., 2022). En raison de son importance écologique et de sa sensibilité aux pressions environnementales, la VAS sert d'indicateur pour orienter les efforts de conservation et de restauration (Orth et al., 2017; Giacomazzo et al., 2020).

En s'appuyant sur 496 observations d'abondance de la VAS issues du Réseau de suivi ichtyologique du ministère de l'Environnement, de la Lutte contre les changements climatiques, de la Faune et des Parcs (MELCCFP), Laporte et al. (2023) identifient les variables

environnementales associées à son déclin. Selon des observations par caméra subaquatique, la probabilité d'occurrence de la VAS a diminué de 75 % à 20 % entre 2002 et 2021. En cohérence avec la littérature (e.g., Vis et al., 2007; Hudon et al., 2012; Giacomazzo et al., 2020), leurs résultats indiquent une réduction de la zone photique, liée à l'augmentation de la turbidité. La distribution spatiale estivale de la VAS à travers le paysage aquatique reflète de multiples interactions entre facteurs environnementaux (Bornette et Puijalon, 2009; Hudon et al., 2018).

1.1.4 Facteurs déterminant la distribution estivale de la VAS

Au LSP, l'augmentation printanière de la température de l'eau rompt l'hivernage et amorce le cycle annuel de la biomasse de VAS, qui s'étend de mai à septembre (Morin et Champoux, 2006). La reprise de la croissance mobilise les réserves de glucides stockées dans les organes végétatifs (i.e., turions, rhizomes, stolons) (Adamec, 2018). Chez la vallisnérie d'Amérique, la croissance débute lorsque la température de l'eau atteint environ 13 °C (Rybicki et Carter, 2002). Toutefois, le rôle de la lumière dans la rupture de l'hivernage reste limité, les turions demeurant enfouis sous une fine couche de sédiments organiques (Kadono, 1988; Adamec, 2018). La croissance végétative subséquente dépend de l'intensité lumineuse qui décroît exponentiellement le long de la colonne d'eau (i.e., loi de Beer-Lambert) (Kirk, 1994). Les traits morphologiques des espèces en rosette (e.g., vallisnérie) accentuent leur sensibilité à la photolimitation, contrairement aux espèces caulescentes (e.g., myriophylle à épis), dont les tiges érigées facilitent l'accès à la lumière en surface (Hudon et al., 2000; Arthaud et al., 2021). En 2007, la vallisnérie colonisait jusqu'à 8,3 m de profondeur, contre 3,25 m en 2021, conséquence d'un triplement de la turbidité à l'échelle du lac (Giacomazzo et al., 2020; Laporte et al., 2023). La variabilité des contraintes lumineuses reflète l'hétérogénéité hydrodynamique et une morphologie altérée par les aménagements anthropiques.

Depuis le milieu du XIXe siècle, le dragage du chenal central pour la navigation concentre près de 70 % du débit en provenance des Grands Lacs dans un corridor d'environ 500 m de large (Morin et Côté, 2003; MDDEFP, 2013). Cette configuration crée une masse d'eau centrale rapide (i.e., 0,5 à plus de 1 m s^{-1}), peu turbide et de teinte verdâtre, encadrée par des eaux latérales plus lentes (i.e., < 0,4 m s^{-1}) et brunâtres, alimentées par les affluents nord et sud (Talbot, 2006; Frenette et al., 2006). En l'absence d'études spécifiques sur les effets des vagues générées par la navigation au LSP, des observations réalisées dans d'autres systèmes fluviaux suggèrent qu'il pourrait s'agir

d'un facteur de déclin estival de la VAS. Par exemple, dans le Rhin, Thunnissen et al. (2019) associent la fréquence et l'intensité des passages de navires à une réduction de l'occurrence de la VAS, attribuable aux vagues et à l'accélération du courant. En contexte expérimental, Doyle (2001) simule l'effet de vagues artificielles de 0,15 m sur la croissance de la vallisnérie d'Amérique et observe une diminution de la biomasse totale de 50 %. Ces observations contrastent avec des conditions hydrodynamiques modérées qui, en l'absence de perturbation mécanique, favorisent le développement de la VAS. Les courants faibles (i.e., $< 0{,}2$ m s^{-1}), en prolongeant le temps de résidence, facilitent l'absorption des nutriments, tout en réduisant l'arrachement foliaire et les ruptures des tiges (Chambers et al., 1991; Morin et al., 2000; Crossley et al., 2002; Thunnissen et al., 2019). Par exemple, la vallisnérie, grâce à ses feuilles souples et allongées, s'aligne avec le courant et profite de l'atténuation de la traînée qu'offre un herbier dense (Hudon, 1997; Morin et al., 2000). À l'inverse, des espèces comme l'élodée du Canada (Elodea canadensis), qui s'implantent sur des substrats meubles (Nichols, 1999), développent un enracinement superficiel, associé à une tolérance moindre aux courants rapides (Puijalon et al., 2005; Wu et al., 2023). Paradoxalement, les travaux de dragage du chenal central entraînent la relocalisation des sédiments en périphérie du corridor navigable et dans le delta des îles de Sorel, en amont (Morin et Côté, 2003). Entre 2000 et 2016, le déclin de la VAS a particulièrement affecté le nord-est du LSP, presque dépourvu de VAS (Hudon et al., 2018), une situation attribuée à l'érosion des dépôts de dragage et à l'augmentation subséquente de la turbidité (Hudon et Carignan, 2008). Une dynamique opposée a été observée au nord-ouest du chenal, où la VAS a recolonisé les hauts-fonds formés par les déblais de dragage (Hudon et al., 2018). Selon Laporte et al. (2023), les hauts-fonds situés dans la masse d'eau centrale pourraient offrir un refuge photique à la VAS, alors que sa distribution actuelle reste majoritairement confinée au sud-ouest du lac.

1.1.5 Le rôle des processus hivernaux

La littérature documente abondamment les facteurs responsables du déclin estival de la VAS au LSP (Laporte et al., 2023). En revanche, la contribution des processus hivernaux, ainsi que les effets saisonniers différés (i.e., *winter legacy effect*) sur la dynamique de croissance estivale, demeurent peu explorés. Pourtant, le cycle saisonnier d'englacement expose les herbiers submergés à des conditions hivernales prolongées, généralement entre décembre et avril (Cunjak et al., 1998; Talbot, 2006). Or, une cartographie estivale réalisée entre 1999 et 2001 a révélé la

présence de chenaux d'écoulement dépourvus de VAS au sud-ouest du chenal de navigation, en dehors des principales dépressions morphométriques (Morin et Champoux, 2006). La cooccurrence spatiale de la VAS et de la glace au LSP suggère une interaction potentielle, possiblement médiée par des conditions hydromorphologiques communes. Morin et Champoux (2006) soulignent un manque de données empiriques sur l'hydrodynamique hivernale, les propriétés physiques du couvert de glace (i.e., épaisseur, type) et la profondeur réelle de la colonne d'eau en période d'englacement. Laporte et al. (2023) suggèrent également que l'influence des perturbations mécaniques exercées par les glaces sur la VAS demeure mal comprise. La documentation limitée des dynamiques sous-glace s'explique par les contraintes logistiques et méthodologiques propres à la limnologie hivernale. Block et al. (2019) reconnaissent que les travaux menés en milieu aquatique gelé nécessitent un équipement spécialisé, des protocoles de sécurité stricts et une organisation adaptée aux conditions hivernales, ce qui restreint l'acquisition de données à grande échelle et sur des périodes prolongées. Le LSP s'inscrit dans un contexte de gestion active des glaces, incluant des estacades, des îlots de stabilisation, le déglaçage du chenal central par brise-glaces et celui des zones latérales en fin de saison par aéroglisseurs (Bastien, 1976; Morin et Côté, 2003; La Violette, 2004; Côté et Morin, 2007). En plus de prévenir les embâcles causés par l'amoncellement de glace à l'exutoire du lac, ces aménagements modifient localement l'hydrodynamique hivernale (Morin et Côté, 2003; Scalabrini et Morse, 2021) et pourraient favoriser la présence de chenaux d'écoulement préférentiels dépourvus de VAS (Morin et Champoux, 2006).

La variabilité spatiale des interactions entre la VAS et le couvert de glace nécessite une approche intersaisonnière, capable de capter les dynamiques physiques de l'englacement et les réponses écologiques associées. Les échosondeurs, qui fonctionnent même en eau turbide, mesurent la hauteur de la canopée et la couverture de la VAS à haute résolution, à partir desquelles est calculé le biovolume (i.e., hauteur moyenne × proportion de couverture), qui sert de proxy à la biomasse estivale. Ils enregistrent également la profondeur de la colonne d'eau, utile pour décrire les gradients bathymétriques liés à la distribution spatiale de la VAS (Vis et al., 2003; Stocks et al., 2019; Botrel et al., 2023). En période d'englacement, le géoradar (GPR) peut produire, à l'image de l'échosondeur en période d'eau libre, des profils continus géoréférencés de l'épaisseur de glace (Stevens et al., 2009; Kämäri et al., 2017; Fu et al., 2018). Des mesures ponctuelles in situ de variables physico-chimiques, hydrologiques et cryosphériques peuvent appuyer les relevés

spatiaux, tant pour valider les profils que pour comprendre les conditions influençant l'englacement et la distribution de la VAS (Block et al., 2019). La télédétection satellitaire optique offre une perspective saisonnière pour le suivi spatio-temporel du couvert de glace. Les capteurs optiques permettent d'estimer la durée d'englacement et l'étendue de la glace à partir des contrastes spectraux entre l'eau libre, la glace et la neige (Hall et Riggs, 2007; Duguay et al., 2015; Liu et al., 2021). En revanche, l'utilisation des capteurs optiques demeure contrainte par la couverture nuageuse (Tarrio et al., 2020). Pour le suivi de la VAS, s'ajoutent une résolution spatiale souvent insuffisante pour détecter les herbiers fragmentés et l'atténuation optique par la turbidité et la profondeur de l'eau (Nelson, 2006; Rowan et Kalacska, 2021; De Grandpré et al., 2022). L'absence d'approches intégrées combinant les conditions d'englacement et la dynamique de la VAS freine la compréhension des effets différés de l'englacement sur la VAS, en milieu fluvial soumis à une gestion active des glaces. Dans une démarche exploratoire, documenter ces interactions contribue aux efforts de conservation et de restauration des herbiers du LSP.

1.2 Problématique

L'un des principaux défis liés à l'étude hivernale de la VAS réside dans la perception selon laquelle cette période, marquée par la sénescence et la dormance, constitue une phase d'activité biologique négligeable. Renforcée par la difficulté d'observer les herbiers sous la glace, elle marginalise les effets potentiels de la dynamique d'englacement sur leur résilience. La littérature scientifique hivernale met traditionnellement l'accent sur les espèces ripariennes, dont la présence reste perceptible en surface (Lind et al., 2014). Cette marginalisation pourrait découler de l'idée implicite que la colonne d'eau offre un environnement relativement stable en raison de son inertie thermique. Contrairement aux hélophytes et amphiphytes, directement soumis aux variations de température de l'air, les hydrophytes submergées bénéficient de la capacité thermique massique élevée de l'eau, qui atténue les fluctuations thermiques journalières et saisonnières dans la colonne d'eau (Barbe, 1984; Vavrus et al., 1996; Bornette et Puijalon, 2009; Kirillin et Shatwell, 2016). Or, cette stabilité n'exclut pas l'exposition de la VAS à des perturbations induites par la formation et la dynamique du couvert de glace.

Selon Lind et al. (2014), la dynamique phénologique des glaces (i.e., congélation de l'eau, épaississement et rupture de la glace) contribue à la dégradation de la végétation aquatique et riparienne (i.e., perte de biomasse et de couverture végétale). Plus précisément, ils décrivent, dans

leur revue de la littérature, les impacts physiques associés au retrait et aux mouvements de la glace, tels que l'abrasion, l'arrachement de la VAS et l'érosion du substrat. D'autres études rapportent également des effets physiologiques, notamment la déshydratation cellulaire causée par le gel, à l'origine d'un stress hypoxique, ainsi qu'une réduction de l'activité photosynthétique (Renman, 1989; Pearce, 2001). Au LSP, Hudon et al. (2018) rapportent une baisse progressive d'environ 1 m du niveau moyen de l'eau à Sorel entre 1970 et 2016, pendant la saison de croissance de la VAS. En hiver, pour sa part, une diminution du niveau d'eau, combinée à la variabilité spatiale de l'épaisseur de glace, augmente le risque de contact entre la glace, les structures végétatives résiduelles et le substrat (Carmignani et Roy, 2017). Callaghan et al. (2016) évoquent une perturbation semblable dans un lac nordique des Territoires du Nord-Ouest, où une épaisseur de glace parfois supérieure à 2 m pourrait limiter l'espace sous-glace et compromettre l'incubation dans les frayères de salmonidés.

En contexte fluvial-lacustre, l'hétérogénéité des conditions hydrodynamiques favorise la formation de types de glace variés, tels que la glace de rive, les plaques de glace flottantes, le frasil et la glace de fond (Michel et Ramseier, 1971; Ashton, 1986; Leppäranta, 2015). Parmi ces types, le frasil pourrait contribuer, par son action mécanique, à l'apparition des chenaux préférentiels décrits par Morin et Champoux (2006). Le frasil correspond à des cristaux en suspension, formés dans des eaux turbulentes en surfusion (i.e., < 0 °C). Dans ces conditions actives, les cristaux aux propriétés adhésives peuvent s'agglomérer sur un substrat rugueux ou des objets submergés (Prowse et Gridley, 1993; Hicks, 2009; Stickler et Alfredsen, 2009), comme les infrastructures d'adduction d'eau potable (Richard et Morse, 2008), suggérant un potentiel d'ancrage similaire sur les structures végétatives résiduelles. Lorsque l'augmentation de la température de l'eau (i.e., $>$ 0 °C) surmonte les forces de liaison, la glace de fond résultant de cette agglomération risque d'entraîner, lors de sa remontée, les structures végétatives et le substrat auxquels elle adhère (Pan et al., 2020). Ces mécanismes demeurent toutefois difficiles à observer sous le couvert avec les instruments disponibles, et sont évoqués ici comme pistes d'explication plutôt que comme hypothèses testées dans ce mémoire (cf. Section 1.3). Enfin, l'accroissement de l'épaisseur totale du couvert de glace, incluant la superposition de glace noire (i.e., congélation de l'eau) et de glace blanche (i.e., métamorphisme de la neige), atténue la lumière transmise (Adams et Roulet, 1980; Yang et al., 2012). Selon Weyhenmeyer et al. (2022), chaque centimètre de glace blanche ou de

neige réduit l'irradiance sous-glace d'environ 9 %, compromettant ainsi la croissance des producteurs primaires.

Au-delà des impacts physiques directs, il est également envisageable que la remise en suspension des sédiments par la glace de fond ou la friction exercée par le retrait du couvert de glace remobilisent les propagules végétatives enfouies et contribuent à la recolonisation printanière (Scrimgeour et al., 1994; Lind et al., 2014; Pan et al., 2020). Néanmoins, la viabilité des propagules transportées par hydrochorie dépend de leur tolérance aux contraintes physiques, telles que le gel, ainsi que de leur aptitude à coloniser des habitats hydromorphologiques distincts (Bornette et Puijalon, 2009; Adamec, 2018). Par exemple, Adamec (2018) a recensé plusieurs cas expérimentaux où des turions, comme ceux de l'utriculaire commune (*Utricularia vulgaris*) et du potamot capillaire (*Potamogeton trichoides*), piégés dans la glace, tolèrent des températures comprises entre −6 et −10 °C (Glück, 1906, cité dans Adamec, 2018). Bien que les espèces étudiées ne soient pas représentatives du LSP (Laporte et al., 2023), ces expérimentations appuient l'idée d'une tolérance au gel chez certains turions. Faute d'observations hivernales, l'impact du déplacement des propagules sur la recolonisation printanière demeure incertain, notamment en raison d'effets différés potentiels pouvant interagir avec d'autres facteurs environnementaux.

À l'échelle locale, la configuration sinueuse du chenal de navigation pourrait accentuer certaines perturbations physiques exercées sur la VAS. Bastien (1976) identifie notamment la première courbe située en aval des îles de Sorel comme une zone propice à l'accumulation de glace et à la formation d'embâcles. Le transport des glaces en dérive vers le lac Saint-Pierre s'effectue principalement par la masse d'eau centrale, partiellement dégagée; par une analyse diagnostique des vulnérabilités aux arrêts de glace, Scalabrini et Morse (2021) indiquent qu'à l'approche de cette courbe, le changement de direction contraint les plaques de glace dérivantes à ralentir sous l'effet de la friction exercée entre les fragments. En conditions de concentration élevée des fragments (e.g., > 70 % de la surface recouverte) et de décélération, une partie du débit dévie latéralement sous le couvert de glace adjacent au chenal. L'accrétion de glace (i.e., empilement irrégulier) pourrait intensifier la turbulence à l'interface eau-glace, un mécanisme reconnu pour favoriser la formation de frasil (Hicks, 2009). Il y a une vingtaine d'années, Morin et Champoux (2006) suggéraient que la production initiale de frasil s'opérait dans l'archipel des îles de Sorel. Cependant, l'absence de données hydrodynamiques hivernales entrave la compréhension des processus d'accumulation et de transport du frasil au LSP, rendant délicate la formulation

d'hypothèses hydroécologiques sur les effets des interventions humaines (Morin et Côté, 2003). Compte tenu de ces dynamiques, il est plausible que le frasil et les plaques de glace en dérive, entraînés par la déviation latérale du débit, migrent sous le couvert de glace adjacent et entretiennent localement des chenaux d'écoulement préférentiels dépourvus de VAS.

Ces perturbations hivernales s'inscrivent dans un contexte de changements climatiques globaux, susceptibles de modifier la phénologie de l'englacement et les conditions hydroclimatiques associées (Woolway et al., 2020; Yang et al., 2020; IPCC, 2023). Depuis 1948, la température moyenne annuelle de l'air a augmenté de 1,3 °C au sud du Québec et les projections prévoient une hausse de 2 à 6 °C d'ici 2100, par rapport à la période de référence 1986–2005, selon les scénarios d'émissions de gaz à effet de serre (Zhang et al., 2019). Cette tendance suggère une arrivée tardive de la saison froide et une augmentation de la fréquence des épisodes de pluie hivernale, ce qui pourrait réduire la durée du couvert de glace et altérer l'intensité des crues printanières (Döll et Zhang, 2010; Bush et Lemmen, 2019; Woolway et al., 2020). Au LSP, de telles modifications pourraient réduire l'amplitude et la durée des crues (Hudon et al., 2018), compromettant ainsi la connectivité avec les habitats de frai des milieux humides riverains (Döll et Zhang, 2010; Rondeau-Genesse, 2020).

En dépit de l'abondance de données sur les pressions estivales exercées sur la VAS au LSP (e.g., Hudon et al., 2018; Giacomazzo et al., 2020; Laporte et al., 2023), les processus hivernaux demeurent peu explorés. La persistance des chenaux d'écoulement dépourvus de VAS, la complexité des interactions entre types de glace et hydrodynamisme, ainsi que les incertitudes liées aux changements climatiques mettent en évidence la nécessité d'explorer les effets différés de l'englacement sur la VAS. La nature multidimensionnelle de cette problématique justifie la mise en place d'une approche intersaisonnière exploratoire centrée sur la variabilité spatiale de l'épaisseur de glace, afin de combler les lacunes empiriques.

1.3 Objectifs, hypothèses et cadre analytique

Ce projet vise à explorer, dans une perspective d'effets différés potentiels, les relations entre les conditions d'englacement hivernal et la variabilité spatiale du biovolume estival de la VAS au LSP, un milieu soumis à une gestion active des glaces et à de multiples pressions anthropiques. Le biovolume de la VAS a été mesuré à l'aide d'un échosondeur lors de campagnes menées en août et septembre 2021 et 2022. L'épaisseur de glace a quant à elle été mesurée avec un GPR à la mi-

février 2022, soit pendant l'hiver entre les deux saisons estivales. Parallèlement, la durée d'englacement a été estimée par télédétection pour contextualiser l'évolution spatiale saisonnière du couvert de glace à l'échelle du lac. Dans les trois cas, les campagnes visaient à capter le maximum saisonnier, soit le pic estival de biovolume, l'épaisseur maximale du couvert de glace et la durée totale d'englacement, sur un secteur localisé dans la partie sud-ouest du LSP. La variation interannuelle du biovolume, calculée comme la différence entre les deux campagnes estivales, a été utilisée comme variable réponse pour explorer l'influence spatiale potentielle de l'épaisseur de glace, de la durée d'englacement et des conditions hydro-morphologiques du milieu.

Pour modéliser les relations entre le biovolume et les variables environnementales hivernales, une approche d'apprentissage automatique par forêts aléatoires (i.e., *random forests*) a été mise en œuvre. Ce modèle empirique non paramétrique n'impose aucune relation fonctionnelle prédéfinie entre les variables explicatives et la variable réponse (Breiman, 2001). Il est adapté à des contextes écologiques complexes (e.g., différentes masses d'eau du LSP), où les relations peuvent être non linéaires, interactives ou spatialement influencées par des effets de seuil (Cutler et al., 2007; Evans et Cushman, 2009). Malgré leur utilisation croissante en télédétection pour classifier des variables cryosphériques telles que l'étendue ou la durée d'englacement à partir de séries temporelles (e.g., Yang et al., 2021), l'application des forêts aléatoires à la prédiction de l'épaisseur de glace demeure marginale. Cette limite s'explique par les incertitudes associées aux approches empiriques prédictives, qui ne modélisent pas les processus thermodynamiques sous-jacents (Murfitt et al., 2018).

De même, bien que les forêts aléatoires aient été appliquées à la modélisation de la présence, de la couverture ou de la distribution spatiale de la VAS (e.g., Midwood et al., 2021), elles restent rarement utilisées pour prédire directement son biovolume. Indépendamment des approches par apprentissage automatique, quelques travaux ont examiné l'impact des variables hivernales, telles que la durée d'englacement, sur des indicateurs de la productivité végétale et de leur variabilité spatiale, comme le biovolume (e.g., Valley, 2016). À ma connaissance, l'intégration explicite de l'épaisseur de glace pour prédire la variabilité spatiale du biovolume demeure absente de la littérature.

L'originalité de ce projet repose sur l'intégration conjointe de l'épaisseur et de la phénologie de la glace pour expliquer la variabilité spatiale du biovolume en tenant compte des gradients hydro-morphologiques, par un croisement de données multi-sources à haute résolution spatiale.

Cette démarche permet d'explorer les liens spatiaux et d'offrir une base empirique pour formuler des hypothèses mécanistes sur les effets différés intersaisonniers, tout en contribuant à repérer des zones potentiellement vulnérables sur le plan écologique, associées à un espace sous-glace restreint ou, indirectement, au transport de frasil et de fragments de glace sous le couvert.

Les objectifs et les hypothèses de ce projet s'inscrivent dans le cadre de la question de recherche suivante : Quelles relations spatiales peut-on observer entre les conditions d'englacement hivernal, notamment l'épaisseur de glace, et la variation interannuelle du biovolume estival de la VAS au LSP ? La profondeur d'eau, qui module à la fois la croissance de la VAS et l'épaisseur de la glace (Hudon et al., 2000; Kirillin et al., 2012), a été intégrée aux modèles afin de caractériser les gradients hydro-morphologiques susceptibles d'influencer ces relations.

À partir de l'objectif général énoncé au début de cette sous-section, quelques objectifs spécifiques ont été formulés :

1. Cartographier la variabilité spatiale de l'épaisseur de glace à son maximum saisonnier (février 2022) à l'aide de mesures obtenues par GPR, validées ponctuellement par forages de la glace, et estimer la durée d'englacement à partir d'images satellitaires.

2. Décrire les patrons spatiaux de variation du biovolume estival de la VAS entre 2021 et 2022, en lien avec les gradients hydro-morphologiques, incluant l'espace libre sous-glace.

3. Développer un modèle exploratoire fondé sur une approche par forêts aléatoires pour expliquer la variation interannuelle du biovolume, en intégrant les variables cryosphériques et hydro-morphologiques, puis évaluer leur importance relative et leurs effets marginaux.

En s'appuyant sur la question de recherche et les objectifs, quelques hypothèses de travail ont été avancées. De nature heuristique, elles visent à orienter l'exploration des relations spatiales entre les conditions d'englacement hivernal et la variation interannuelle du biovolume, sans prétendre établir de lien causal. D'abord, il est attendu que l'épaisseur de glace maximale soit négativement associée à la variation interannuelle du biovolume estival de la VAS, particulièrement dans les zones peu profondes, puisqu'une épaisseur de glace plus importante

réduit l'espace libre sous la glace, ce qui pourrait exercer des contraintes physiques (e.g., contact direct avec le substrat, friction et abrasion) sur les structures végétatives (Lind et al., 2014; Carmignani et Roy, 2017). Ensuite, une durée d'englacement plus longue pourrait être associée à une diminution du biovolume estival, en raison d'une exposition prolongée à des conditions défavorables à la photosynthèse, telles qu'une faible transmission lumineuse (Adams et Roulet, 1980; Weyhenmeyer et al., 2022) ou un gel extracellulaire susceptible d'induire un stress hypoxique sur les structures végétatives, tel que rapporté chez les espèces vasculaires terrestres (Pearce, 2001). Cet effet pourrait être modulé par la profondeur et les masses d'eau locales.

Enfin, la stratigraphie glacielle, notamment les proportions de glace blanche et noire, ainsi que la présence distincte de frasil, de glace de fond ou de fragments de glace transportés sous le couvert, ont été envisagées comme des variables potentielles pouvant contribuer, par photolimitation (Weyhenmeyer et al., 2022) ou perturbations mécaniques (Morin et Champoux, 2006; Hicks, 2009; Pan et al., 2020), à la diminution locale du biovolume. Toutefois, ces variables n'ont pas été intégrées au modèle explicatif principal, leur détection sous le couvert demeurant difficile avec les instruments disponibles et les observations ponctuelles ne permettant pas d'obtenir une couverture spatiale continue.

CHAPITRE II

USING GEOPHYSICAL AND REMOTE SENSING METHODS TO EXPLORE THE SPATIAL RELATIONSHIPS BETWEEN ICE COVER CONDITIONS AND SUBMERGED AQUATIC VEGETATION IN A SHALLOW FLUVIAL LAKE

Abstract

Submerged aquatic vegetation (SAV) provides essential habitat for fish and supports many ecological functions in aquatic ecosystems. At Lake Saint-Pierre, the largest floodplain lake of the St. Lawrence River (Québec, Canada), SAV habitats are threatened by watershed-derived pressures during summer and have lost significant coverage over recent decades. Spatial variability in winter ice cover has been suggested as a potential additional driver of this decline. This study explores whether ice cover conditions (thickness and duration) are associated with interannual changes in SAV distribution, and how water depth, a shared driver of ice thickening and SAV growth, mediates this association through under-ice clearance. SAV biovolume, the proportion of the water column occupied by SAV, was mapped using hydroacoustic surveys in summer 2021 and 2022, while ice thickness and ice cover duration were mapped using ground-penetrating radar and Sentinel-2 imagery during winter 2022. Random forest regression models were trained to test the ability of ice-related variables and water depth to predict the interannual change in SAV biovolume (ΔBIOV) at 20 m resolution between 2022 and 2021. Ice cover duration was most negatively associated with ΔBIOV, whereas ice thickness was only weakly associated in shallow areas and, like water depth, did not generalize spatially when tested alone. The ice-related predictors partly acted as proxies for the hydromorphological gradient (water depth and flow conditions), and our two-year design could not separate a winter legacy effect from unmodeled concurrent growing-season drivers, notably spring flood conditions, leaving the contribution of ice cover conditions to SAV decline only partly resolved. Nevertheless, this study offers an initial exploration of potential physical and physiological effects of ice cover on SAV.

Keywords: Submerged aquatic vegetation; biovolume; Lake Saint-Pierre; lake ice cover; ground-penetrating radar; random forest model

2.1 Introduction

Submerged aquatic vegetation (SAV) communities play a key role in shallow lakes through multiple ecological functions. For instance, they form mono- or multi-species assemblages that stabilize benthic sediments by dampening flow and trapping suspended particles, thereby reducing turbidity (Madsen et al., 2001; Cornacchia et al., 2020). These communities further support biogeochemical cycling by retaining nutrients such as phosphorus and nitrogen through vegetative uptake (Yu et al., 2025) and regulating carbon and oxygen fluxes via photosynthesis (Binzer et al., 2006). Their structural complexity promotes trophic interactions by providing heterogeneous habitat that offers shelter and foraging grounds for invertebrates and waterfowl, substrate for epiphytic organisms, and spawning sites for fish (Lodge, 1991; Thomaz et al., 2025). However, long-term observations indicate that lake SAV communities are increasingly threatened worldwide, raising concerns about the loss of ecosystem functions they support. A recent global meta-analysis by Botrel and Maranger (2023), covering over 300 lakes, reported that SAV has declined in 41% of analyzed time series, largely attributed to anthropogenic stressors that reduce light availability, such as eutrophication, turbidity, invasive species, and altered hydrological regimes. While these pressures have been well-documented during the growing season, the potential role of winter conditions in driving SAV decline remains poorly understood.

In temperate lacustrine ecosystems, the seasonal growth cycle of SAV coincides with the formation and break-up of an ice cover. During the transition to winter, falling temperatures lead to progressive surface heat loss and vertical water mixing, initiating ice cover formation at the water surface (Kirillin et al., 2012), which can isolate SAV below thickening layers of ice and snow. Once established, the ice cover can attenuate light transmission to SAV (Weyhenmeyer et al., 2022), and under low-light conditions, photosynthetic activity decreases (Spencer & Wetzel, 1993). SAV species thus overwinter through dormancy, i.e., a physiological response to cooling water temperature and shortening photoperiod, whereby individuals rely on vegetative propagules such as turions and rhizomes or on persistence of overwintering shoots for survival (Jarvis & Moore, 2008; Adamec, 2018). Once ice retreats, warming water temperature and lengthening photoperiod initiate rapid vegetative growth from these overwintering structures, supported by carbohydrate reserves stored before winter (Spencer & Wetzel, 1993; Adamec et al., 2020). This phenological cycle is therefore fundamental to SAV ecology in ice-covered lakes, with the timing

and success of spring regrowth influencing SAV biomass and distribution during the following growing season.

Lake Saint-Pierre (LSP), a shallow fluvial expansion of the St. Lawrence River in Québec, Canada, exemplifies these anthropogenic pressures on SAV. Situated between the cities of Sorel-Tracy and Trois-Rivières, LSP forms the largest fluvial expansion of the St. Lawrence River along its freshwater course, approximately 120 km upstream from the estuarine transition near Québec City. This shallow floodplain lake harbors over 197 km^2 of contiguous wetlands, including channels, floodplain depressions, and marshes, which represents one of the largest freshwater marsh complexes in North America (Hudon et al., 2018). Owing to its biodiversity and functional connectivity, LSP was designated a Ramsar wetland of international importance in 1998 and a UNESCO World Biosphere Reserve in 2000. Together, the lake and its wetlands support 288 bird species and 79 fish species (MDDEFP, 2013). Among these, the yellow perch (*Perca flavescens*) stands out as a historically abundant species (Magnan et al., 2022), once emblematic of local commercial and recreational fisheries collectively worth up to CAD$10 million annually during the 1980s (Mailhot et al., 2015). Its population collapsed in the 1990s, largely attributed to habitat degradation (e.g., de la Chenelière et al., 2014; Giacomazzo et al., 2020). Despite regulatory measures, such as quotas and legal-size limits, continued population declines led to a moratorium on yellow perch fisheries in effect since 2012 (Magnan et al., 2022).

Echoing patterns observed worldwide, SAV communities in LSP have shown substantial declines in spatial occurrence over the last decades, coinciding with widespread degradation of littoral habitats and the collapse of key fish populations. Spanning over 900,000 km^2 across the United States, Ontario, and Québec, the LSP watershed is home to nearly six million people in its Québec portion alone (MDDEFP, 2013). At the regional scale, conflicting land-use priorities have been identified as a persistent obstacle to the conservation of littoral ecosystems (e.g., Lévesque et al., 2024; Watson et al., 2024). Notably, intensive row-crop agriculture, primarily corn and soybean, occupies over 4300 hectares, or approximately 90% of the cultivated floodplain as of 2016 (Jobin & Brodeur, 2023). The impacts of agriculture on the optical properties of the water column have been extensively examined. For instance, Giacomazzo et al. (2020) linked a threefold rise in lake-wide turbidity to long-term declines in both SAV and yellow perch via reduced light availability. Additionally, Clermont et al. (2023) showed that turbidity during the spring flood was 35% to 93% higher above flooded corn and soybean fields than over wet meadows, identifying

bare or sparsely vegetated croplands as active sources of suspended sediments. While these effects on water optical properties appear localized, they stem from broader watershed-scale pressures, as tributaries convey excess suspended particulate matter and nutrients from upstream runoff over agricultural and urban landscapes, as well as from point-source discharges (Hudon & Carignan, 2008). Dissolved organic matter from forested watersheds is also known to contribute to light attenuation (Frenette et al., 2003). Furthermore, nutrient-enriched conditions in nearshore areas have long been associated with the proliferation of benthic cyanobacteria (*Lyngbya wollei)*, whose dense mats can outcompete SAV for light (Vis et al., 2008). These watershed-scale pressures have jointly diminished water clarity, thereby narrowing the photic depth of colonization for native rosette-forming species such as *Vallisneria americana*, which lack the vertical growth capacity of caulescent taxa. According to Laporte et al. (2023), this long-term decline was marked by a drop in SAV occurrence from 75% to 20% at underwater camera stations monitored between 2002 and 2021, while the maximum colonization depth of low-canopy species, once reaching up to 8.3 m, has contracted to 3.25 m over the same period.

In addition to these watershed-derived pressures on water clarity, SAV coverage in LSP can be explained by hydrodynamic heterogeneity and lakebed morphology alterations, both associated with commercial navigation. Since the mid-19th century, repeated dredging operations of the central navigation channel (Morin & Côté, 2003) have confined most of the Great Lakes-sourced flow to an approximately 500-m-wide, fast-flowing corridor (i.e., 0.5 to > 1 m s^{-1}) bordered by slower-flowing lateral waters (i.e., < 0.4 m s^{-1}) fed by tributaries from both shores (Morin & Champoux, 2006; Hudon & Carignan, 2008). Fast-flowing water and ongoing maintenance dredging thus likely preclude permanent SAV establishment within the LSP navigation channel. For instance, Chambers et al. (1991) observed that SAV biomass decreased with increasing flow velocity up to 1 m s^{-1} in two rivers in Alberta, with negligible SAV occurrence above this threshold possibly arising from shoot breakage, uprooting, or nutrient limitation. While dredging operations have altered flow regimes, resuspension of sediment from disposal sites along the periphery of the navigation channel is also thought to have contributed to the near-complete loss of SAV in the northeastern portion of the lake (Hudon et al., 2018). Conversely, the same authors noted that some of these disposal sites, located downstream of the Sorel Islands delta and northwest of the navigation channel, have formed shallow shoals that SAV has partially recolonized. At present, SAV coverage remains largely restricted to the southwestern part of the lake, and clearer waters

originating from the Great Lakes have been identified as a potential photic refuge critical to SAV persistence in LSP (Laporte et al., 2023).

Despite the widespread presence of SAV in the shallow southwestern reaches, hydroacoustic surveys conducted in the early 2000s uncovered persistent SAV-devoid channels in this area (Morin & Champoux, 2006), a pattern that they suggested may not be fully explained by summer environmental drivers. This spatial discrepancy thus prompted consideration that ice-induced disturbance (i.e., physical and physiological) could explain the absence of SAV. Whether the spatial overlap between SAV coverage and ice cover conditions (e.g., type, thickness, stratigraphy, duration) reflects causal interactions or merely shared environmental drivers remains an open question, given the scarcity of empirical insights into ice cover properties and sub-ice physical conditions. Similarly, Laporte et al. (2023) emphasized the uncertain role of ice dynamics in shaping SAV distribution. Addressing this question has, to date, posed multiple challenges, considering that research on SAV during winter faces both conceptual and operational barriers. SAV beneath the ice cover, for instance, has received limited attention. This is possibly because reduced biological activity during dormancy (e.g., Spencer & Wetzel, 1993) is assumed to offer little research interest, and the overwintering strategies of most SAV species (e.g., Adamec, 2018) leave minimal visible biomass. Research has instead focused mostly on riparian species, which remain visible above the ice cover surface (e.g., Lind et al., 2014). Moreover, fieldwork in ice-covered lakes requires specialized equipment and strict safety protocols, which often constrain sampling efforts (Block et al., 2019).

Nevertheless, knowledge of ice-induced disturbance on SAV has been inferred from studies on riparian functional groups and river ice dynamics (i.e., freeze-up, thickening, break-up, and ice-jam events), where physical processes such as scouring, detachment, fracturing, or uprooting are more evident along the shore (Lind et al., 2014). While biomass loss is among the potential outcomes of physical disturbance by ice, such disturbance may also influence post-winter recolonization and therefore play a role in spatial community composition (Scrimgeour et al., 1994). Additionally, SAV may be subject to heterogeneous ice conditions, which are directly related to local hydromorphology (e.g., water depth, flow velocity, benthic substrate), groundwater upwelling, and meteorological drivers (e.g., air temperature, precipitation) that determine the timing and extent of freeze-up and break-up (Kirillin et al., 2012). In shallow, flow-sheltered nearshore waters, the typically earlier onset of freeze-up prolongs conductive heat loss and snow

metamorphism, resulting in thicker formation of congelation (black ice) and snow ice (white ice) layers (Adams & Roulet, 1980; Leppäranta, 2015). Each additional centimeter of snow and white ice has been linked to an approximately 9% decrease in under-ice irradiance, a factor known to limit the growth of photoautotrophs (Weyhenmeyer et al., 2022). Although not focused on SAV, a few studies have emphasized how spatial variability in ice thickness can lead to shallow benthic areas freezing to the lakebed. Arp et al. (2022), for instance, showed that bedfast ice in Alaskan lakes can reach up to 2 m thick, eliminating under-ice clearance and the overwintering habitat provided for fish and aquatic mammals such as beavers and muskrats. As discussed by Callaghan et al. (2016), bedfast ice may compromise embryo incubation of salmonids in northern Canadian lakes, which suggests that similar ice-related disturbances could also threaten overwintering vegetative organs of SAV. On the dynamic end of the flow regime, frazil ice composed of needle-like crystals can form and remain suspended in supercooled, turbulent waters (Hicks, 2009; Leppäranta, 2015). The adhesion of frazil crystals to interstitial benthic substrates or submerged structures under these conditions is known as anchor ice (Stickler & Alfredsen, 2009). This phenomenon, sometimes observed on riverbeds and municipal water intakes (e.g., Richard & Morse, 2008), may also accrete on overwintering vegetative structures of SAV. In such cases, extracellular ice formation can induce cellular dehydration in vascular plants (Pearce, 2001). Moreover, once supercooled water conditions cease (i.e., water warming above 0 °C), anchor ice loses its adhesive properties and, owing to the lower density of ice, rises to the surface, which could detach or uproot overwintering structures of SAV (Stickler & Alfredsen, 2009).

At the local scale, LSP has undergone progressive ice management since the 1960s to prevent downstream ice jams and maintain the transit of ice floes through the navigation channel. These measures include ice booms, stabilizing islets, mid-winter icebreaking, and late-season nearshore hovercraft operations conducted by the Canadian Coast Guard (CCG; Morse, 2001; Côté & Morin, 2007). Among the areas of concern, Bastien (1976) identified the first bend of the navigation channel downstream of the Sorel archipelago as particularly prone to ice accumulation and jamming. Scalabrini and Morse (2021) expanded on this observation through ice-jam risk diagnostics, indicating that the directional shift at this bend slows drifting ice floes as friction builds between converging fragments. As ice concentration increases (e.g., > 70%), part of the water flow may be diverted laterally beneath the ice cover on either side of the navigation channel (Morin & Côté, 2003), potentially carrying frazil and ice floes that could scour local SAV patches

and maintain the SAV-devoid channels reported by Morin and Champoux (2006). The extent to which such under-ice disturbances, shaped by ice management measures, influence SAV distribution remains unclear without winter-specific hydrodynamic measurements and observations of sub-ice transport processes.

The seasonal asynchrony between ice-induced disturbance during winter and the summer peak of SAV growth introduces a time-lag challenge, whereby ecological responses may only emerge months after the initial stress. This time-lag thus underscores the need for an interseasonal framework that integrates both ice cover conditions and SAV spatial metrics. Acquiring the spatially extensive environmental data for such a framework typically relies on remote sensing technologies, which are widely used to monitor large aquatic systems (e.g., Duguay et al., 2015; Stocks et al., 2019). However, in the optically complex waters of LSP, where turbidity-driven light attenuation hinders the effectiveness of satellite- and airborne-based sensors, hydroacoustic surveys have proven more effective for fine-scale SAV mapping (Vis et al., 2003). These surveys yield measurements of canopy height, coverage, and water depth, from which biovolume (BIOV), a compound indicator of the proportion of the water column occupied by SAV, can be calculated (Valley et al., 2005). Biovolume correlates almost linearly with dry biomass and is a proxy for cumulative summer biomass production (Botrel et al., 2023). Once the lake freezes, the tools and variables of interest shift to surface conditions. For ice monitoring, optical satellite remote sensing can track seasonal changes in ice cover by detecting spectral contrasts between open water and snow-covered ice to estimate ice extent and duration (e.g., Yang et al., 2019; Huo et al., 2022), even under partial cloud cover, with data gaps mitigated through temporal gap-filling techniques (Weiss et al., 2014). Although other satellite sensors like radar and laser altimeters have been primarily used to estimate sea ice thickness, uncertainties of 0.12 to 0.41 m due to challenges in accounting for snow conditions (Beckers et al., 2017; Tilling et al., 2018), combined with coarse spatial resolution averaging out fine-scale thickness variability, currently make them unsuitable for practical application in small, hydrologically complex lakes (Murfitt & Duguay, 2021). Instead, fine-scale ice thickness has been derived using ground-penetrating radar (GPR), which detects internal interfaces based on contrasts in dielectric properties (e.g., Galley et al., 2009; Stevens et al., 2009). In rivers, GPR-derived ice thickness estimates obtained at frequencies ranging from 0.1 to 1.5 GHz have been compared with co-located borehole measurements, with reported mean absolute error (MAE) of 0.03 to 0.05 m (Galley et al., 2009; Kämäri et al., 2017; Fu et al., 2018).

This study aims to explore how ice cover may be associated with SAV distribution in LSP by assessing spatial relations between summer cumulative SAV growth, previous-winter ice cover conditions, and shared hydromorphological drivers. The study was conducted in the southwestern portion of LSP, located within the St. Lawrence Valley, Québec (46°10′N, 72°50′W), where the remaining SAV coverage has been the focus of ecological monitoring efforts over the past two decades (e.g., Hudon et al., 2018; Laporte et al., 2023). Cumulative SAV growth was monitored using a boat-mounted echosounder from mid-August to early September of 2021 and 2022, while ice conditions were measured using a GPR in mid-February 2022, complemented by optical satellite imagery throughout the same winter. These periods aimed to capture the seasonal maximum in SAV distribution, the thickest ice conditions, and the ice-covered duration from freeze-up to break-up. We explore how SAV distribution, as captured by the interannual change in maximum biovolume (ΔBIOV), responded to spatial variation in ice thickness, ice cover duration, and other hydromorphological drivers. Given the long-term degradation of littoral habitats in LSP, there is a need to consider year-round SAV dynamics to understand whether and how ice cover conditions impact SAV interannual distribution, with the aim of guiding conservation and restoration efforts. However, this can be complicated by the interactions between the ice cover and other known drivers of SAV distribution such as water depth or hydrodynamic exposure, as well as the active ice management and the delayed nature of the ecological response.

Considering the role of bedfast ice, frazil accumulation, diverted floes, and anchor ice as potential physical constraints on overwintering vegetative structures, this study included under-ice clearance along with observations of ice-induced disturbances to identify areas where SAV may be vulnerable to ice conditions. While direct causal inference is hindered by the delayed nature of ecological responses, we adopted an exploratory framework to examine spatial associations and provide a basis for formulating mechanistic hypotheses regarding interseasonal effects. Rather than formal hypothesis testing, we propose two heuristic hypotheses to guide the interpretation of ΔBIOV's observed spatial patterns. First, greater ice thickness is expected to be negatively associated with ΔBIOV, especially in shallow areas, as thicker ice cover reduces under-ice clearance, which has been shown to create unfavorable conditions for overwintering habitat (e.g., Arp et al., 2022). Second, a longer ice cover duration is expected to be negatively associated with ΔBIOV, as it may reflect a prolonged period of ice thickening that could extend the exposure of overwintering vegetative structures to low light availability (e.g., Weyhenmeyer et al., 2022).

2.2 Methods

2.2.1 Study area

The study area encompasses Lake Saint-Pierre (46°10′N, 72°50′W; ~370 km^2), a widening of the St. Lawrence River in southern Québec, Canada (Figure 2.1a). The study site (~15 km^2) lies within its southwestern portion (Figure 2.1b). Lake morphology and surrounding lowlands were shaped by the retreat of the Laurentide Ice Sheet and the postglacial incursion of the Champlain Sea (Parent & Occhietti, 1988). Although water depths exceed 11 m in the central navigation channel, most of the lake is shallow, with a mean depth of ~3 m (Hudon & Carignan, 2008). Water levels can fluctuate by up to 3 m annually, peaking during the spring freshet (March–May) and reaching minima in late summer (August–September) (Morin & Côté, 2003; Fisheries and Oceans Canada, n.d., station ID 15975). With a temperate climate (Assani, 2023), the mean annual temperature was 5.8 °C, while the mean monthly temperatures in January and July, the coldest and warmest months, were −11.5 °C and 20.4 °C, respectively, for the 1981–2010 climate normals. During this period, total annual precipitation was 985 mm, about 19% of which fell as snow (Environment and Climate Change Canada [ECCC], n.d.-a, station ID 7026043). Prevailing winds are bimodal, blowing from the northeast and southwest, driven by synoptic systems (Razy et al., 2012; ECCC, n.d.-b, station ID 701LP0N). Lake freeze-up typically starts in late November, and ice persists until mid-April (Morin & Champoux, 2006). Summary hydroclimatic and wind conditions for the 2021–2022 ice season are provided in the Supplementary Material (Figures S1 and S2).

The study site (Figure 2.1) is bounded toward the lake center by the navigation channel, which conveys the main throughflow supplied by the Great Lakes (73%), with additional inputs from the Ottawa River (19%) and contributions from north-shore tributaries (< 2%), resulting in a mean annual discharge of approximately 9500 m^3 s^{-1} at the entrance of LSP (Hudon & Carignan, 2008). The study site extends from sheltered marsh wetlands in the southwest to water depths of up to 4 m at its northeastern edge. The lakebed consists of postglacial clay deposits overlain by a mix of sand, silt, and organic mud layers (Saint-Laurent et al., 2010). Several tributaries contribute additional discharge south of the navigation channel, notably the Saint-François (170 m^3 s^{-1}) and Yamaska (85 m^3 s^{-1}) rivers, while the Richelieu River discharges about 435 m^3 s^{-1} upstream of LSP (Hudon & Carignan, 2008). The Tardif channel, a branch of the Saint-François River, flows directly into the study site (Figure 2.1b). This nearshore portion of the southwestern littoral hosts

a mosaic of SAV assemblages dominated by *Vallisneria americana, Potamogeton richardsonii,* and *Heteranthera dubia*, while *Ceratophyllum demersum*, *Elodea canadensis*, *Stuckenia pectinata,* and *Myriophyllum spicatum* are also found across the lake (Laporte et al., 2023).

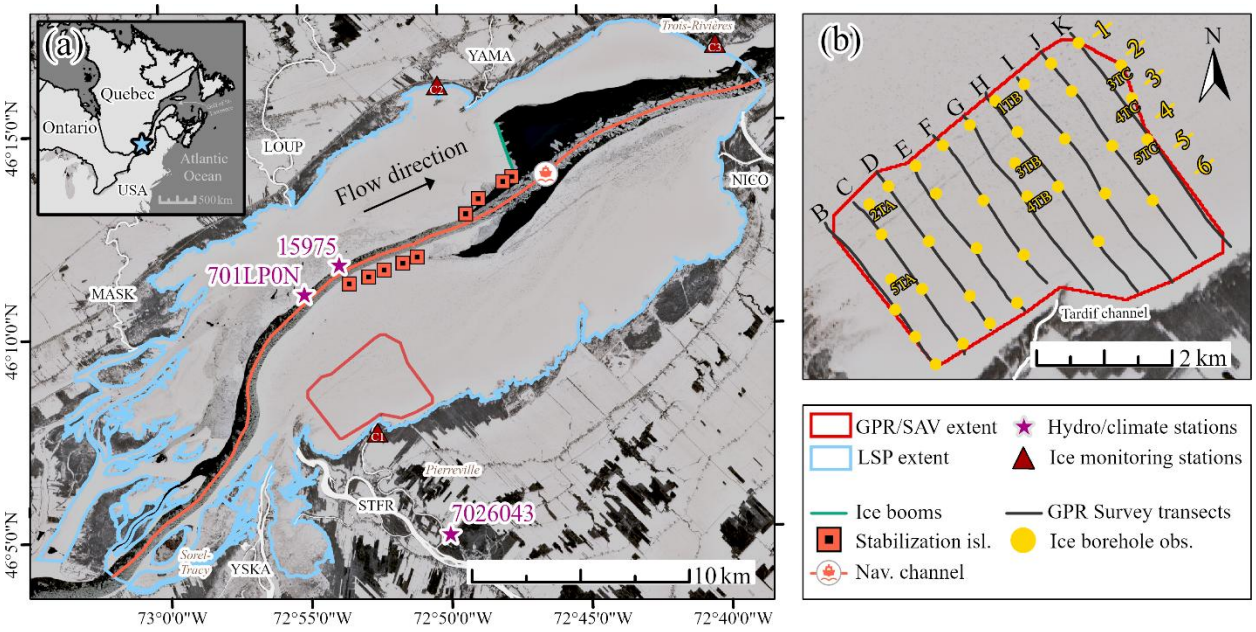


Figure 2.1. *Location of the study site in the southwestern portion of LSP.* ***(a)*** *Location of LSP within the St. Lawrence River in southern Québec, Canada (blue star and rectangle). Main tributaries within the map extent include MASK (Maskinongé River), LOUP (du Loup River), YAMA (Yamachiche River), NICO (Nicolet River), STFR (Saint-François River), and YSKA (Yamaska River). Symbols indicate the hydrometric (ID 15975) and climate stations (IDs 7026043, 701LP0N) as purple stars; ice monitoring stations (C1–C3) as red triangles; and ice management structures (booms, stabilization islets, and the navigation channel) as green lines and orange icons.* ***(b)*** *Site covered by the hydroacoustic and GPR surveys (in red), with GPR transects (black lines) and ice borehole observation sites (yellow dots). Boreholes are labeled by grid position (e.g., 6B); TA, TB, and TC indicate additional boreholes between grid lines. The Tardif channel is also shown. Hydroacoustic transects were omitted for clarity (cf. Section 2.2.2). Basemap: Copernicus Sentinel-2 true-color imagery, January 20, 2022.*

2.2.2 Mapping interannual SAV biovolume change

Summer fieldwork was conducted on August 17–20 and September 7–8, 2021, and on August 10–12, 2022. A boat-mounted Lowrance SIMRAD single-beam echosounder equipped with an 83/200 kHz TotalScan Skimmer transducer (22° conical beam width) was used to collect hydroacoustic data. Survey dates were selected based on optimal weather and water conditions; the boat was driven at low speed along hydroacoustic transects to minimize wave-induced motion. Transects were spaced 250 m apart (Figure S3 in Supplementary Material), consistent with

recommended intervals for biovolume mapping in lakes larger than 4 km^2 (Navico Inc., 2014). Positions from the echosounder's integrated GPS were logged every second (1 Hz), and 5–30 acoustic pings were averaged per position report. The echosounder was set to shallow-water mode, with a 15 Hz ping rate, a 200 kHz frequency, and Wide Area Augmentation System (WAAS) satellite-based corrections enabled for precise geopositioning (Helminen et al., 2019).

Georeferenced acoustic records were processed by the Québec Ministry of Environment (MELCCFP) using BioBase EcoSound, an automated cloud-based software. First, the uploaded data underwent internal quality-control procedures, during which data failing detection criteria were removed; minimum detection distances correspond to 0.73 m from the transducer face to the SAV canopy and 0.37 m to the lakebed. Observations where SAV height averaged below 5% of the water column depth were considered not vegetated, and the 2% deepest points were also excluded to minimize false detections caused by bottom debris (Navico Inc., 2014). For each remaining acoustic record, BIOV (%) was calculated according to the following formula (Valley et al., 2005):

$$BIOV\ (\%) = \frac{h_{SAV}}{dz} \times 100 \quad (1)$$

where h_{SAV} is the SAV height (m) and dz is the water column depth (m), both derived from acoustic returns using automated feature-detection algorithms.

The resulting point data were interpolated using ordinary kriging algorithms (Webster & Oliver, 2007) in EcoSound, which operate with non-user-accessible geostatistical parameters and estimate BIOV values at unsampled locations based on the spatial relationships among input points (Navico Inc., 2014; Valley et al., 2015). BIOV rasters were generated at 20 m spatial resolution for each survey year to maintain a consistent alignment with all subsequent mapped variables. The interannual change in percent biovolume (i.e., ΔBIOV) was mapped by subtracting 2021 BIOV values from those of 2022 at each grid cell within their common spatial extent.

2.2.3 Mapping ice thickness

Winter fieldwork was conducted on February 14–15 and 21, 2022. Boreholes were drilled at 37 locations (Figure 2.1b) to measure ice thickness (THK) and stratigraphy. Two boreholes were drilled 1 m apart at each location using a 10-inch-diameter ice auger, one stopping approximately

5 cm above the ice-water interface and the other extending through it. White ice thickness was measured with an L-shaped rod in the partial borehole, from the ice surface to the transition between the white and black ice layers; total ice thickness was measured with the same instrument in the second borehole. Black ice thickness was calculated as the difference between the two measurements. The overlying snow was excavated to the ice surface, and snow thickness was measured once per location prior to drilling. An underwater camera mounted on a pole was deployed through the boreholes to document under-ice conditions. The water column was inspected for the presence of frazil ice, while the lakebed was examined for anchor ice, bedfast ice, and overwintering SAV. Water depth was measured with a weighted graduated tape from the ice surface to the lakebed.

Ground-penetrating radar (GPR) surveys were conducted during the first two days of winter fieldwork. A sled-mounted IceMap GPR system equipped with a 500 MHz Noggin sensor was used to collect radar traces (Sensors & Software Inc., 2013). This radar frequency has been used in previous studies to measure ice thickness in freshwater environments (e.g., Stevens et al., 2009; Annan et al., 2016). Survey dates were selected to target cold air temperatures and dry snow conditions, minimizing radar wave attenuation associated with liquid water content in the snow cover (Bradford et al., 2009). The sensor and a Topcon GNSS receiver were connected to a SPIDAR network interface, which synchronized radar traces with positioning data. The GNSS receiver operated in autonomous mode with WAAS corrections enabled. The system was operated in reflection mode and towed behind a snowmobile at low speed along GPR transects (Figure 2.1b). Radar traces were acquired at a nominal spatial step size of 0.5 m (Sensors & Software Inc., 2013) and signal-stacked in groups of 32 for each positional report to improve the signal-to-noise ratio. The sensor integrates parallel transmitting and receiving antennas separated by 0.155 m. A time-zero correction of 9.8 ns was applied to account for system delay and the fixed air path between the antennas and the ice surface.

GPR traces were then preprocessed in IceMap version 1 r8 using a de-wow filter to remove low-frequency noise and a gain function to enhance deeper radar reflections. Two-way travel times to the ice-water interface were automatically extracted with the modified energy ratio algorithm (Wong et al., 2009), a tool implemented in IcePicker version 1 r7, which detects the first high-amplitude reflection. Outliers, defined as standardized residuals exceeding ± 1.96 (4.5% of traces), were excluded from the dataset.

Ice thickness was mapped using a two-step geostatistical framework in ArcGIS Pro version 2.8.0. GPR two-way travel times (TWT) were first aggregated within a 100 m radius (i.e., every 200 m along transects) to homogenize sampling density and minimize striping artifacts inherent to the transect-based survey layout (e.g., Oliver & Webster, 2014; Knadel et al., 2015). The aggregated TWT were interpolated across the study site using simple kriging with trend removal. A southeast-northwest gradient in TWT was identified with the trend analysis tool in ArcGIS Desktop version 10.6.1, then modeled in ArcGIS Pro with a first-order polynomial and removed prior to residual interpolation to meet the stationarity assumption of simple kriging (Webster & Oliver, 2007). A spherical semivariogram model (nugget = 0.047, partial sill = 0.076, range = 1864 m) was fitted to the residuals. Residuals (i.e., detrended TWT values) were then estimated at each grid cell as a weighted linear combination of up to five neighboring values, with weights from the semivariogram model. The trend was added back to the kriged residuals, and the resulting intermediate TWT raster was exported at 10 m spatial resolution as an input for the next step.

Borehole total ice thickness measurements were spatially interpolated using empirical Bayesian kriging regression prediction (EBKRP) in ArcGIS Pro version 2.8.0, which incorporated the TWT raster as an explanatory variable for spatial prediction of ice thickness (Krivoruchko, 2012). EBKRP was used given that TWT is related to ice thickness through radar wave propagation in ice (e.g., Galley et al., 2009; Stevens et al., 2009; Fu et al., 2018). Spatially exhaustive coverage of a secondary variable can also reduce prediction error relative to interpolation from sparse point data alone (e.g., Njoku et al., 2023). EBKRP was implemented using an exponential semivariogram model, 300 simulations, a subset size of 100, and an overlap factor of 1. A search neighborhood of up to 10 observations within a 1968 m radius guided local prediction. The correspondence between observed and predicted ice thickness was assessed using leave-one-out cross-validation (LOOCV), whereby each borehole observation was withheld sequentially, predicted from the remaining dataset, and compared to its observed value. Cross-validation prediction error metrics such as the root mean square error (RMSE) and the coefficient of determination R^2 (Berrar, 2019; Chicco et al., 2021) were used for assessment. Spatial uncertainty was quantified from the same EBKRP semivariogram model with the prediction standard error, i.e., the square root of the expected variance for each predicted value (Krivoruchko, 2012; Krivoruchko & Gribov, 2019). Ice thickness (THK) and prediction standard error rasters were exported at 20 m spatial resolution to match that of the hydroacoustic-derived ΔBIOV raster.

2.2.4 Mapping water depth

Water depth (WD) was mapped using ordinary kriging (Webster & Oliver, 2007) performed in ArcGIS Pro. Ordinary kriging yielded low prediction errors for bathymetric interpolation in other aquatic systems (e.g., Curtarelli et al., 2015; Chowdhury et al., 2017). Bathymetric data were obtained from the Canadian Hydrographic Service (CHS) non-navigational (NONNA) product at 10 m spatial resolution and clipped to the study site extent (Fisheries and Oceans Canada, 2018). This dataset, compiled from hydroacoustic surveys, was selected over depth measurements from SAV eco-sounding surveys (cf. Section 2.2.2) for two reasons. First, NONNA provided depth measurements distributed more evenly across the entire study site, whereas SAV surveys were restricted to transects spaced 250 m apart (Figure S3), leaving larger sampling gaps where interpolated values would rely on more distant observations. Second, NONNA was already referenced to the Canadian Geodetic Vertical Datum (CGVD28), allowing for precise vertical corrections to daily water levels. A spherical semivariogram model (nugget = 0, partial sill = 1.039, range = 5750 m) was fitted to the CHS bathymetric data. Water depth was estimated at each grid cell as a weighted linear combination of up to 10 neighboring observations. The correspondence between observed and predicted water depths was assessed using LOOCV, with the same error metrics as for THK (cf. Section 2.2.3). A vertical offset of 0.40 m was then applied to correct for the difference between the chart datum and mean water levels (Fisheries and Oceans Canada, n.d.) recorded at the nearest hydrometric station (Figure 2.1a; station zero at 3.41 m CGVD28) during the 2021 summer fieldwork (i.e., August 17 to September 8). Predicted water depths, corrected to daily water levels for each winter fieldwork date, were also independently validated against water depths measured in boreholes (cf. Section 2.2.3). Daily water level offsets were 1.01 m (February 14), 1.02 m (February 15), and 1.49 m (February 21). Spatial uncertainty was estimated from the kriging prediction standard error derived from the fitted semivariogram. The water depth (WD) and standard error rasters, corrected to summer 2021 water level, were exported at 20 m resolution.

2.2.5 Mapping ice cover duration

Ice cover duration (ICD) was mapped from a time series of 24 Sentinel-2 satellite images acquired between November 1, 2021, and April 30, 2022, using supervised classification. Level-2A imagery at 10 m (i.e., bands B2, B3, B4, B8) and 20 m (i.e., bands B5, B6, B7, B8A, B11, B12) spatial

resolution was obtained from the European Space Agency's Copernicus program (Drusch et al., 2012). These images, already corrected to bottom-of-atmosphere reflectance via the Sen2Cor processor (Main-Knorn et al., 2017) as part of the systematic processing pipeline from the Copernicus program, were accessed through the Google Earth Engine cloud-based platform (Gorelick et al., 2017). Scenes were then manually inspected and selected, rather than filtered using a typical fixed cloud cover threshold (e.g., Huo et al., 2022), to minimize cloud cover confounding pixel classification during rapidly changing ice conditions (i.e., freeze-thaw events), while retaining scenes judged suitable for classification despite some cloud presence during stable mid-winter ice-cover conditions.

Pixels already flagged as clouds, cloud shadows, or radiometrically saturated by the Sen2Cor Scene Classification Layer were masked (Main-Knorn et al., 2017). A wetland mask was conservatively delineated from the pre-freeze scene on November 11, 2021, using the Normalized Difference Water Index (NDWI; McFeeters, 1996). This scene was selected because water levels were below the average for the period up to the first day of winter fieldwork, and snow-covered marshes (i.e., frozen wetlands) could otherwise be misclassified as ice (e.g., Huo et al., 2022). The NDWI was calculated according to the following formula:

$$NDWI = \frac{\rho_{green} - \rho_{NIR}}{\rho_{green} + \rho_{NIR}} \quad (2)$$

where ρ_{green} and ρ_{NIR} represent the reflectance of the green (B3) and near-infrared (B8) Sentinel-2 spectral bands, respectively. Pixels with positive NDWI values were used to extract the unfrozen lake water boundary, whereas the wetland mask (represented in gray in Figure 2.2a) was delineated from the remaining pixels with negative values (i.e., non-water surfaces including marshes). The resulting vector boundary was refined based on photo-interpretation where necessary, for instance in areas with mixed water and marsh pixels, and was spatially aligned to the 20 m resolution of the Sentinel-2 imagery.

Supervised classification was performed in Google Earth Engine. Pixels were classified into three classes: ice, ice floes, and water. Training samples (Figure 2.2a) were generated from a point grid and assigned to classes through photo-interpretation (Figure 2.2b–d) based on tones and spatial patterns at the pixel scale. The number of sample points varied among scenes due to cloud masking and changing ice conditions, with manual additions where necessary. Details on scene

dates, cloud cover, and training samples are provided in the Supplementary Material (Table S1). A Random Forest classifier was trained for each scene using surface reflectance values from the ten spectral bands previously introduced, with the native 10 m spatial resolution bands resampled to 20 m. The Normalized Difference Snow Index (NDSI; Hall et al., 1995) was also included. NDSI was calculated according to the following formula:

$$NDSI = \frac{\rho_{green} - \rho_{SWIR}}{\rho_{green} + \rho_{SWIR}} \quad (3)$$

where ρ_{green} and ρ_{SWIR} represent the reflectance of the green (B3) and short-wave infrared (B11) Sentinel-2 spectral bands, respectively. Training samples were split into 70% for classifier training and 30% for validation. Predicted classes were compared with the photo-interpreted reference labels from each scene's validation samples using confusion matrices (Table S1), yielding standard classification accuracy metrics (Table S2), such as the overall accuracy (i.e., the proportion of correctly classified samples) and the Kappa coefficient (Cohen, 1960; Congalton & Green, 2019).

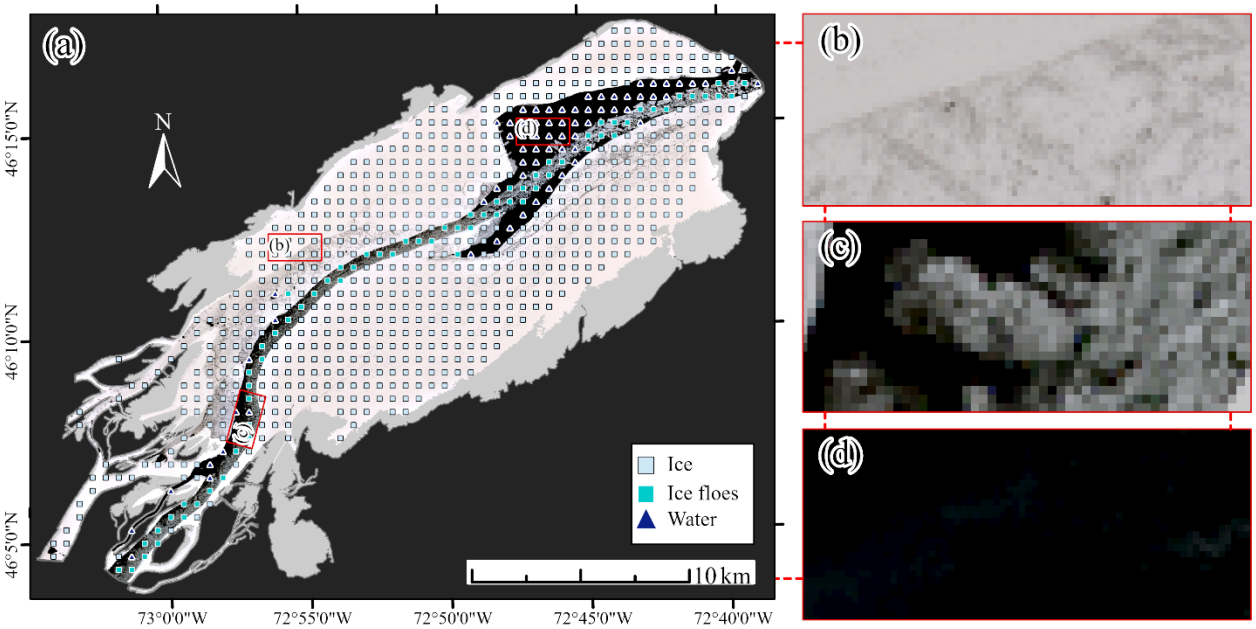


Figure 2.2. *Spatial distribution of photo-interpreted training samples grouped by class.* ***(a)*** *Distribution of training samples for a model scene. Frozen wetlands are shown in gray. Tones and spatial patterns of the surrounding pixels for training samples assigned to the* ***(b)*** *ice,* ***(c)*** *ice floes, and* ***(d)*** *water classes. Basemap: Copernicus Sentinel-2 true-color imagery, January 20, 2022.*

Classified images were post-processed using temporal gap-filling of cloud-masked pixels (e.g., Weiss et al., 2014). Additionally, ice pixels were reclassified as ice floes where appropriate,

given that throughflow and ship traffic prevent ice consolidation in the navigation channel; revised pixel proportions are reported in Table S1. Ice cover duration was calculated by merging the ice and ice floes classes into a binary ice/no-ice mask, stacking these masks chronologically, and counting, for each pixel, the number of days classified as ice. The ice cover duration (ICD) raster was exported at 20 m resolution for the study site.

Classification accuracy metrics were examined across ice-season phenological phases, which were derived from the lake ice fraction (Yang et al., 2019). The lake ice fraction was calculated as the proportion of ice-covered area (i.e., ice-class pixels only) relative to the LSP water extent, with frozen wetlands excluded (Figure 2.2a). Following Yang et al. (2019), ice fraction thresholds were set at 20% and 80% to determine phenological transition dates (i.e., freeze-up start and end, break-up start and end), and the durations between these dates were calculated (Supplementary Material, Table S3). Canadian Coast Guard ice-management activities were compiled from operational logs and overlaid on the ice phenology time series to provide qualitative context on whether phenological transition dates coincided with, or followed, periods of human intervention (i.e., icebreaking). Finally, daily images from cameras at shoreline monitoring stations (C1–C3; Figure 2.1a) were reviewed as an additional check to corroborate ice onset and complete ice clearance dates with their satellite-derived estimates.

2.2.6 Mapping under-ice clearance

Under-ice clearance (UIC) was calculated as the difference between the water depth and ice thickness rasters (cf. Sections 2.2.3 and 2.2.4). WD values were corrected using the aforementioned water level offset (1.02 m) (cf. Section 2.2.4) for the GPR survey period prior to UIC calculation. UIC values are interpreted such that positive values correspond to the vertical space between the ice-water interface and the lakebed, whereas UIC ≤ 0 corresponds to areas with bedfast ice (i.e., frozen to the lakebed). The UIC raster was exported at 20 m spatial resolution.

2.2.7 Statistical analyses

Pairwise relationships between ΔBIOV and each candidate predictor (i.e., THK, WD, ICD, UIC), as well as potential collinearity among predictors, were explored with scatterplots and correlation analysis using values extracted from the collocated 20 m resolution rasters at each grid cell.

Analyses were restricted to the spatial extent of the ΔBIOV raster, which covered only part of the study area due to logistical constraints. Spearman's rank correlation was used given that some variables deviated from normality and pairwise relationships were non-linear. Random Forest regression (RF) was then implemented to model interannual change in biovolume (i.e., ΔBIOV) as a function of the candidate predictors. RF is an ensemble machine learning algorithm in which predictions of a target variable are obtained by averaging the output of multiple decision trees (Breiman, 2001). It has proven useful for handling complex ecological datasets due to its flexibility in modeling non-linear relationships and is commonly used to perform regression tasks, yielding robust predictive performance compared to other algorithms (e.g., Akselrud, 2024). RF relies on bootstrap aggregation whereby individual decision trees are built from a random sample drawn from a training set with replacement, called the bootstrap sample, which represents about two thirds of the total samples. Training data left aside at each split, known as the out-of-bag (OOB) sample, were used to cross-validate the regression models. The performance of each model was assessed with prediction error metrics such as the goodness of fit with the coefficient of determination R^2 and the RMSE (Chicco et al., 2021; Hodson, 2022). RF regression models were implemented in R with the "Ranger" package (Wright & Ziegler, 2017). Multivariate models were built to predict ΔBIOV using ice-related variables and water depth as predictors. Spatial block cross-validation (Block CV; Roberts et al., 2017), implemented with the "BlockCV" package in R (Valavi et al., 2019), was used to further evaluate model predictive performance by dividing the study site into spatially independent blocks, thereby accounting for spatial autocorrelation among grid cells. Block CV model performance was assessed with both the coefficient of determination R^2 and the squared correlation coefficient r^2 (Viana et al., 2022).

RF models enable the ranking of each explanatory variable's contribution in a regression problem through the measurement of variable importance (Breiman, 2001). Permutation importance was used to calculate the variable importance in R by randomly reshuffling the values of each explanatory variable. Partial dependence plots (PDPs) were generated for multiple multivariate models to assess the marginal effect of each predictor on ΔBIOV, while considering the influence of other predictors. The partial functions were computed in R using the "pdp" package (Greenwell, 2017). Univariate random forest models were fitted to evaluate the predictive ability of each predictor in isolation, and provide a baseline for comparison with potential conditional effects in multivariate models. Finally, variation partitioning was calculated from the Block CV squared

correlation coefficient (r^2) values of the full multivariate model (including all potential predictors) and the univariate models (including predictor subsets) to quantify the exclusive and pairwise shared fractions of variance explained by each ΔBIOV predictor (Peres-Neto et al., 2006; Legendre & Legendre, 2012; Viana et al., 2022).

2.3 Results

2.3.1 Borehole observations

Ice thickness values at the borehole locations were rather homogeneous, with a mean (± SD) of 0.48 ± 0.05 m. The ice stratigraphy was dominated by black ice, averaging 81.8 ± 9.0% of the total thickness, whereas white ice made up the remaining 18.2 ± 9.1%. No frazil ice was observed at any of the locations. The overlying snow was thin, with a mean thickness of 0.07 ± 0.05 m (Figure 2.3). However, a few observations could not be completed. The identification of ice-type transitions at sites 1J and 1K was hindered by the presence of slush. At borehole TB1, an additional ice layer was encountered beneath the surface ice, separated by an intervening water layer of about 1 m; only the surface ice layer is shown in Figure 2.3. Finally, under-ice footage was recorded at 33 of the 37 borehole locations (recordings were lost at the remaining four sites due to camera malfunction), and the lakebed was only visible at 21 sites due to low light conditions (Figure 2.3). Under-ice SAV was visually observed from this footage at four sites (i.e., 2E, 3I, 4E, 6B), where coarse morphological features (i.e., stems and shoots) could be distinguished.

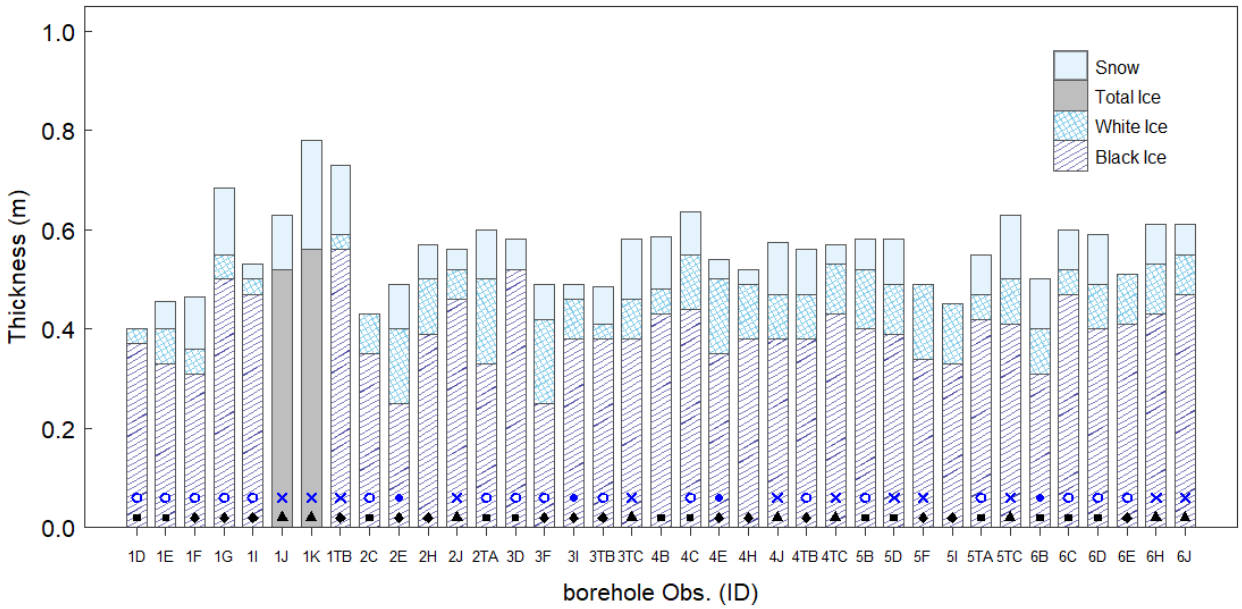


Figure 2.3. *Borehole ice stratigraphy and snow thickness. Site IDs on the x axis are ordered by their group position from the shoreline, from farthest (1) to closest (6) along or off transects (letters) (see Figure 2.1b for site locations). Drilling dates are shown at the base of each bar (black symbols): February 14 (square); February 15 (diamond); February 21 (triangle). Under-ice SAV presence is marked above the latter (blue symbols): observed (filled circle); not observed (open circle); lakebed not visible (cross).*

2.3.2 Kriging cross-validation and prediction uncertainty for ice thickness and water depth

The kriged maps of the potential explanatory variables THK (via empirical Bayesian kriging regression prediction) and WD (via ordinary kriging) (cf. Section 2.3.4) were assessed with a leave-one-out cross-validation (LOOCV) against the borehole observations (cf. Section 2.3.1) and the Canadian Hydrographic Service (CHS) chart datum bathymetric data, respectively. For the WD map, an independent validation was also performed by comparing kriged WD values, adjusted to daily winter water levels (cf. Section 2.2.4), against water depths measured at the borehole locations. The spatial variability of kriging prediction error for both variables was further assessed across the study site with the standard error.

Cross-validation metrics for THK and WD, along with the independent validation metrics for WD, are shown in Table 2.1; scatterplots of predicted versus observed values are available in the Supplementary Material for the WD independent validation (Figure S4) and the THK cross-validation (Figure S5). The RMSE for THK (0.044 m) amounted to 9% of the mean observed ice thickness, though THK variability among boreholes was limited (cf. Section 2.3.1). For WD, the independent validation yielded a higher RMSE (0.380 m) and lower R^2 (0.85) than the LOOCV.

Table 2.1. *Validation metrics for THK and WD. LOOCV: leave-one-out cross-validation; BH: boreholes (n = 36); CHS: Canadian Hydrographic Service bathymetry (n = 6716).*

	THK *(LOOCV, BH)*	**WD** *(LOOCV, CHS)*	**WD** *(Indep. validation, BH)*
RMSE (m)	0.044	0.070	0.380
R^2	0.27	0.99	0.85

The 20 m resolution prediction standard error (SE) maps (Figure 2.4) showed the spatial variability of prediction uncertainty for the interpolated variables. The spatial patterns of SE for THK (Figure 2.4a) and WD (Figure 2.4b) appear, as expected, consistent with the underlying geostatistical relationships, i.e., the spatial dependence inherent to their respective datasets: SE values increase with distance from observation locations, following the discrete borehole locations for THK and the CHS survey lines for WD, with the highest values in the southwest of the site.

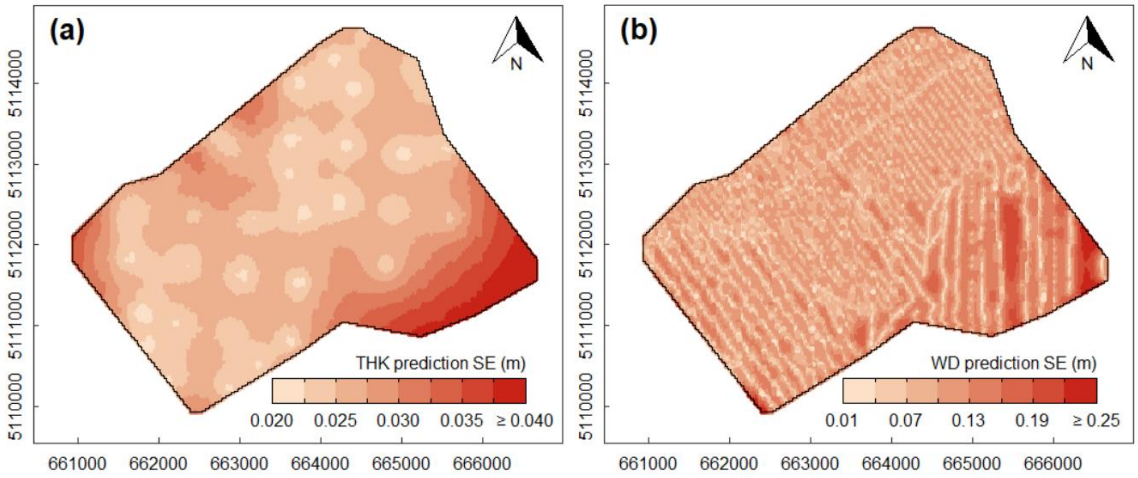


Figure 2.4. *Prediction standard error rasters for the interpolated explanatory variables.* ***(a)*** *ice thickness (THK);* ***(b)*** *water depth (WD).*

2.3.3 Ice cover phenology and classification accuracy

The lake ice phenology (i.e., ice fraction) and per-scene classification accuracy are shown in Figure 2.5. Freeze-up began on January 10 (Figure 2.5a), when drifting ice floes accumulated from east to west across the lake, upstream of ice booms and near the stabilization islets. This process was completed within ten days, leading to a continuous frozen period of 52 days, except along the navigation channel. Break-up started on March 13, following CCG icebreaking, and extended until March 28. The lake was ice-covered for 77 days (i.e., > 20% ice fraction, between FUS and BUE).

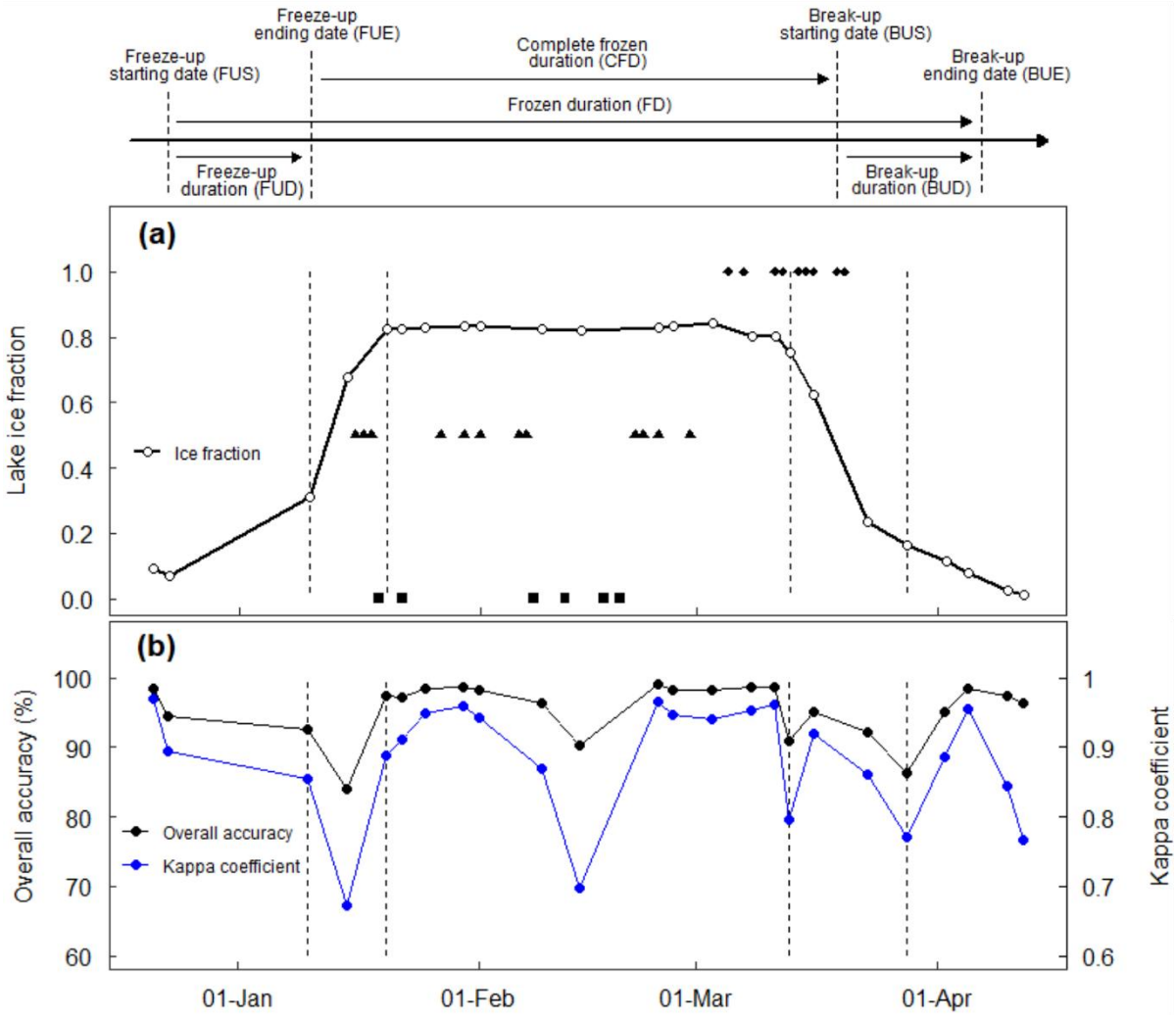


Figure 2.5. *Ice cover phenology and classification accuracy.* ***(a)*** *Lake ice fraction from classified images (n = 24; white dots). CCG ice management activities are indicated by symbols (lake-wide icebreaking: diamond; navigation channel clearing: triangle; ice reconnaissance patrol: square).* ***(b)*** *Overall accuracy (black dots) and kappa coefficient (blue dots) calculated against each scene's validation samples. Phenological cycle phases (annotations) are displayed above both panels. Dashed lines indicate freeze-up (FUS, FUE) and break-up (BUS, BUE); arrows denote transition (FUD, BUD) and frozen durations (FD, CFD).*

Overall accuracy of classified scenes was high, averaging 95.5 ± 4.1% and never falling below 83.9%, while Cohen's kappa confirmed substantial to strong agreement with validation samples, averaging 0.88 ± 0.09 and a minimum of 0.67 (Figure 2.5b). Moreover, the out-of-bag error rate of the RF classifier was 4.3 ± 3.5%, with a maximum of 15.1%. Outside the defined FUS and BUE thresholds, ice was detected as early as December 21, 2021, with onset consistent within 2–3 days and complete clearance confirmed by ice monitoring stations (C1–C3) on April 12, 2022.

2.3.4 Spatial variability of ΔBIOV and explanatory variables

The 20 m resolution map of ΔBIOV and the potential explanatory variables (Figure 2.6) highlight spatial contrast across the study site. Shallow nearshore and central areas show decreased biovolume, i.e., notably more negative ΔBIOV values (Figure 2.6a), while deeper areas farther from the shoreline, where flow was typically faster, show positive values (e.g., along the potential interface of inflowing water masses and near the Tardif tributary). Although ΔBIOV was mostly negative across the site, typically in the order of −10 to −30%, about a third of the grid cells had positive values (increasing biovolume). Nearly one-fifth of all grid cells had minimal ΔBIOV (i.e., < ±5%), suggesting minor interannual changes. Nevertheless, some grid cells (5.4%), especially near potential hydrologically dynamic areas at the northern edge, had biovolume values exceeding 30% compared to the preceding year.

Ice was generally thicker (THK; Figure 2.6b) over shallow nearshore areas (WD; Figure 2.6c), which, being sheltered from strong flow and less exposed to potential breakage, froze earlier (ICD; Figure 2.6d) and accumulated snow first. Under-ice clearance (UIC; Figure 2.6e) was also lower in shallow areas with thicker ice. Conversely, ice was thinner in the most exposed areas, notably at the Tardif tributary confluence and farther from the shoreline (Figure 2.6b), where ice cover duration was also shorter (Figure 2.6d). These areas coincided with greater water depth (Figure 2.6c). However, ice thickness was locally higher in the eastern and northeastern parts of the site, even under deeper water conditions near borehole TB1 (Figure 2.6b). In addition, a crack, ~75 cm wide and stretching several kilometers (Figure 2.6b), was observed across the site (Figure 2.6f), oriented from southwest to northeast. The role of the hydromorphology was apparent, particularly on the ice thickness and ice cover duration maps, which show localized thickening and longer-lasting ice patterns structured by water depth and potential hydrological exposure. The same hydromorphological dynamics were also seen in the ΔBIOV patterns in Figure 2.6a.

Bedfast ice conditions were not reached within the study site (Figure 2.6e). The under-ice clearance, corrected to February 14, 2022, water levels, was positive throughout (min = 0.09 m; median = 1.87 m), with 99% of grid cells showing at least 0.42 m of UIC. These values did not account for ice buoyancy (freshwater ice density ~917 kg m^{-3}; Leppäranta, 2015), which would increase UIC by ~0.04 m on average.

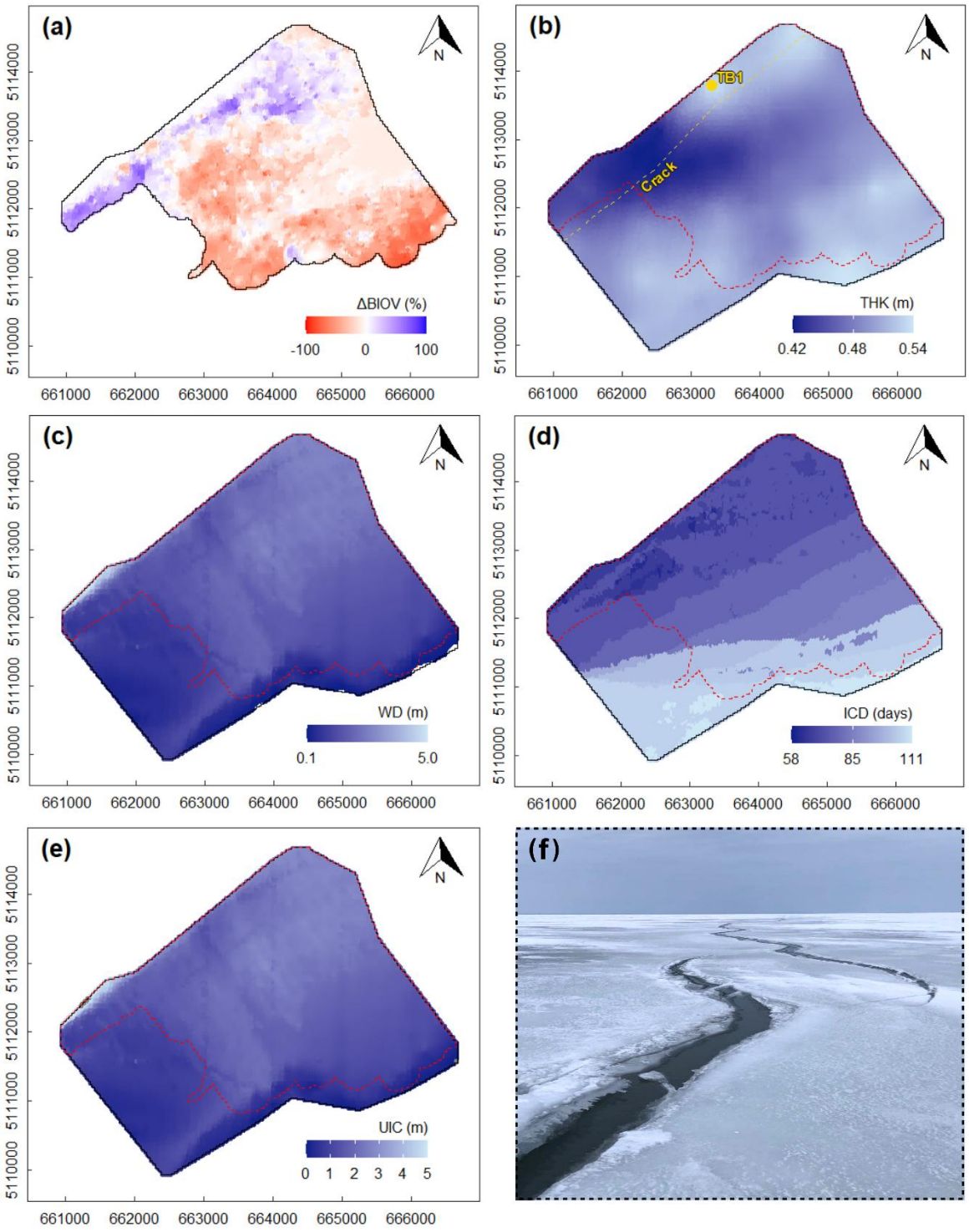


Figure 2.6. *Rasters of ΔBIOV and the potential explanatory variables investigated.* ***(a)*** *ΔBIOV, i.e., the difference between interpolated values from 2022 and 2021;* ***(b)*** *ice thickness (THK);* ***(c)*** *water depth (WD);* ***(d)*** *ice cover duration (ICD);* ***(e)*** *under-ice clearance (UIC);* ***(f)*** *field photo of the longitudinal crack, also displayed in panel* ***(b).*** *The red outline delineates the ΔBIOV analysis extent (n = 56,171 grid cells); cells outside were excluded.*

2.3.5 Pairwise predictor relationships and collinearity

The pairwise correlation matrix (Figure 2.7) shows variations in strength and direction of relationships between ΔBIOV and ice-related predictors. Partial interannual consistency in biovolume spatial patterns was indicated by the positive correlation (r = 0.64) between the 2021 and 2022 biovolume maps. Hence, ΔBIOV was mostly related to its initial state (BIOV21: r = −0.59), with more pronounced biovolume loss (ΔBIOV) in areas with larger initial biovolume. The strongest correlation between ΔBIOV and the potential predictors was with ICD (r = −0.62), followed by UIC (r = 0.37) and WD (r = 0.36), while THK (r = −0.16) was more weakly correlated. Histograms of the predictor distributions showed departures from normality, with ICD being positively skewed, whereas UIC and WD exhibited high kurtosis. Non-monotonic responses of ΔBIOV to some predictors (e.g., UIC and WD) were apparent in scatterplots, as inverted U-shaped trends. Since UIC was derived from WD, both predictors were deterministically related and almost perfectly correlated (r = 0.99), showing that ice thickness had a marginal effect on UIC in most areas of the study site. Accordingly, the relationship between THK and UIC was negative but low (r = −0.20). Likewise, Spearman's coefficients indicated that ICD was moderately collinear with the other predictors (|r| > 0.51), as shallow areas tend to freeze first, leading to thicker ice and longer-lasting ice cover.

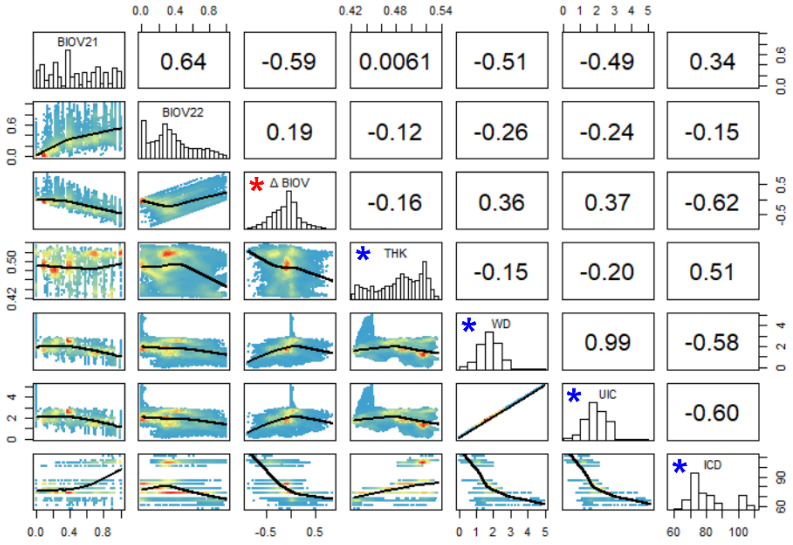


Figure 2.7. *Pairwise correlation matrix and variable distributions. Histograms are displayed on the diagonal panels, density scatterplots with trends on the lower panels (blue to red: low to high dot density), and Spearman's rank correlation coefficients on the upper panels. Red asterisk: response variable; blue asterisk: potential predictors.*

The random forest regression models (cf. Section 2.3.6) do not assume normality and can capture non-linear effects on the response variable through recursive partitioning. These models also tolerate collinearity without compromising predictive performance but may distort individual variable importance when explanatory contribution is shared among collinear predictors (Nicodemus et al., 2010; Gregorutti et al., 2017). UIC and WD were therefore not combined in models, and UIC, not an independent predictor, was excluded from the variation partitioning.

2.3.6 Random Forest regression models

The first multivariate random forest model tested (M1) included all ΔBIOV potential predictors except UIC and yielded the highest OOB R^2 (0.95) and the lowest RMSE (0.054) among all models tested (Table 2.2). The two-predictor models (M2–M5) also captured a large proportion of the variance ($R^2 \approx 0.86–0.93$) in the spatial patterns of ΔBIOV. The performance of models that combined ICD with either WD (M3) or UIC (M4) was nearly identical. WD and UIC had almost the same predictive ability in the univariate models, where each accounted for a substantial proportion of ΔBIOV variance ($R^2 \approx 0.73$), while THK and ICD alone explained comparatively less. OOB performance, however, does not account for the strong spatial correlation among grid cells and is therefore inflated. When model performance was assessed using spatial block cross-validation, which addresses spatial autocorrelation (Roberts et al., 2017), Block CV R^2 values were much lower than their OOB counterparts (Table 2.2).

Table 2.2. *Prediction performance metrics from out-of-bag (OOB) validation (R^2 and RMSE) and spatial block cross-validation (Block CV; R^2 and r^2) for random forest regression models of ΔBIOV. R^2 is the coefficient of determination and r^2 is the squared correlation coefficient.*

Model ID	ΔBIOV Predictors	R^2 (OOB)	RMSE (OOB)	R^2 (Block CV)	r^2 (Block CV)
Multivariate (M1)	THK + WD + ICD	0.95	0.054	0.50	0.50
Multivariate (M2)	THK + WD	0.93	0.067	0.21	0.29
Multivariate (M3)	WD + ICD	0.88	0.088	0.43	0.43
Multivariate (M4)	ICD + UIC	0.87	0.091	0.42	0.42
Multivariate (M5)	THK + ICD	0.86	0.096	0.39	0.39
Univariate (U1)	THK	0.62	0.155	−0.72	0.00
Univariate (U2)	WD	0.74	0.128	−0.58	0.01
Univariate (U3)	ICD	0.41	0.194	0.36	0.37
Univariate (U4)	UIC	0.73	0.130	−0.59	0.01

The prediction performance ranking also changed for the two-predictor models, with models including ICD (M3–M5) outperforming M2 in terms of Block CV R^2 (0.39–0.43 vs. 0.21). A similar contrast was found in the univariate models, where THK, WD, and UIC had negative Block CV R^2, meaning that these predictors did not generalize to spatially independent blocks, while ICD maintained a comparable Block CV R^2 (≈ 0.36) to its OOB R^2 (0.41).

2.3.7 Predictor variable importance and variation partitioning

The variable importance (VI) differed across the multivariate models (Figure 2.8). In the three-predictor model (M1), ICD had the highest relative importance (VI = 1.00), while those of THK (VI = 0.65) and WD (VI = 0.61) were lower. ICD remained the most influential predictor in the two-predictor models (M3–M5), whether combined with WD, UIC, or THK, which contributed similarly to each model's predictions (VI = 0.55, 0.53, and 0.54, respectively). Conversely, in the model composed of THK and WD (M2), both predictors were nearly equivalent in terms of relative importance (VI = 0.92 and 1.00, respectively). Overall, ICD was ranked as the most influential predictor whenever included in a given model, whereas WD and THK took precedence when ICD was omitted.

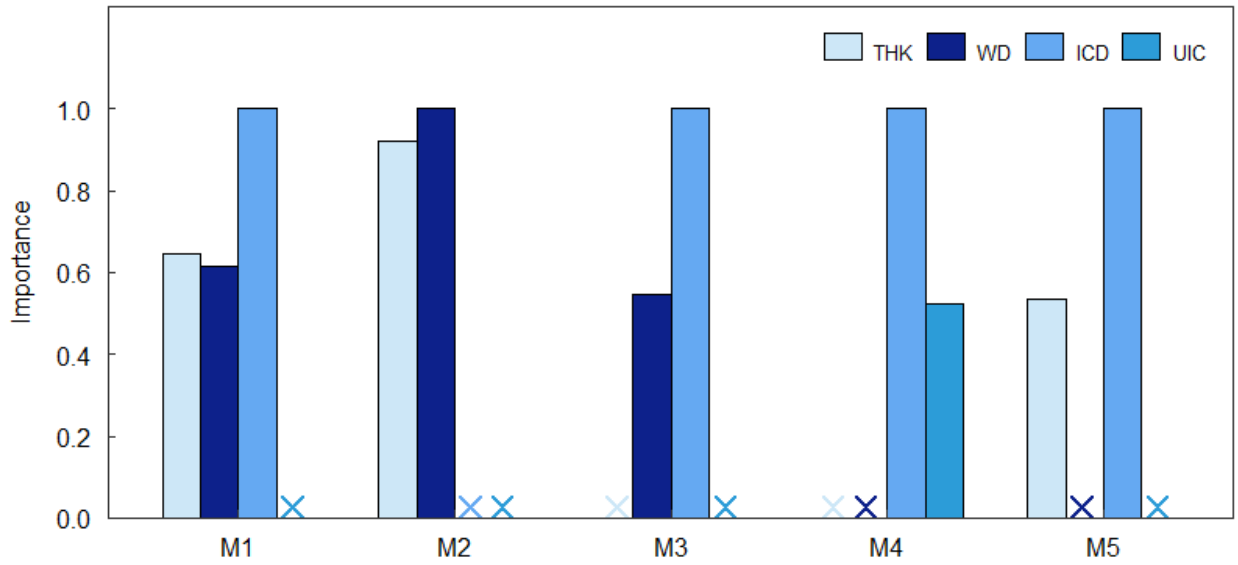


Figure 2.8. *Permutation-based variable importance for the multivariate random forest regression models. Relative importance values were rescaled on a 0–1 range, where higher values implied more influence of a predictor within a given model. Predictors (colors) not included in a model are shown as crosses. These values should be interpreted cautiously, as partial collinearity among predictors may distort relative importance.*

The Block CV squared correlation coefficients (r^2; Table 2.2) were used to calculate the variation partitioning fractions, following Viana et al. (2022) (cf. Section 2.2.7). The results of the variation partitioning for the full model (M1) are presented in Figure 2.9. ICD, as in the VI ranking, appeared to contribute the most to explaining ΔBIOV, as its exclusive fraction of the explained variation ([c] = 0.21) surpassed those of WD ([b] = 0.11) and THK ([a] = 0.07). The pairwise shared fractions involving THK and ICD ([f] = 0.21), as well as WD and ICD ([e] = 0.18), were almost equal to or greater than their respective exclusive fractions. Accordingly, the magnitude of these shared fractions relative to the total explained variance of M1 (i.e., r^2 = 0.50; Table 2.2) points to the effect of collinearity between ICD and the other predictors (Legendre & Legendre, 2012). On the other hand, the fractions of the explained variation shared by THK and WD ([d] = −0.04) and among all three predictors ([g] = −0.24) were negative, and therefore have no direct interpretation as proportions of variance. This can be attributed to suppression effects in variation partitioning (Peres-Neto et al., 2006), whereby predictors weakly correlated with the response variable (e.g., THK; Figure 2.7), when combined with other predictors, explain more variation than the sum of their univariate model performances (i.e., r^2; Table 2.2). The remaining half of the total variation was unexplained ([h] = 0.50), suggesting other important environmental controls unrelated to the predictors considered.

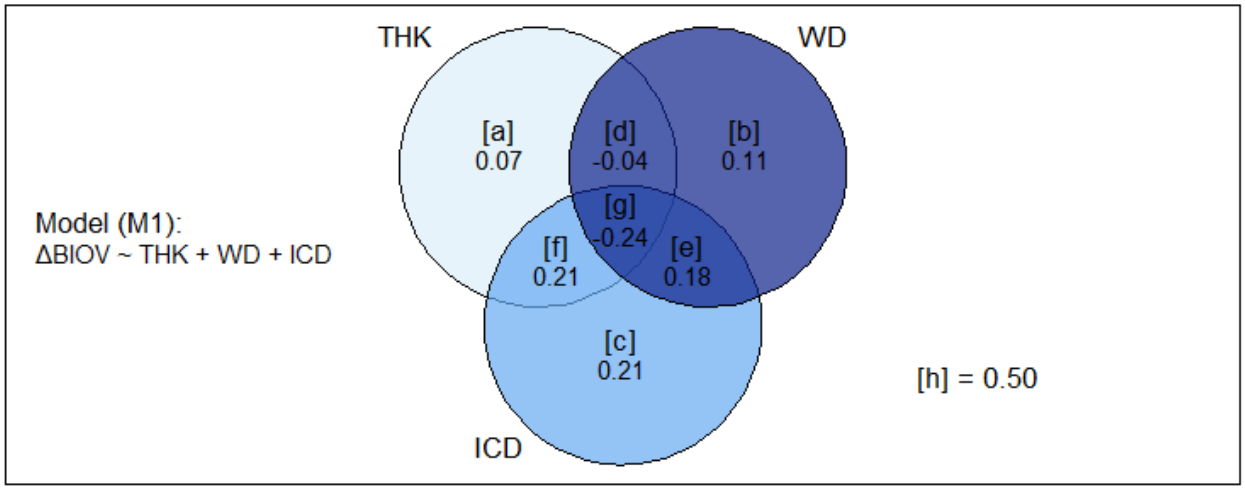


Figure 2.9. *Proportions of variation of ΔBIOV. Fractions [a], [b], and [c] are the variation explained exclusively by THK, WD, and ICD, respectively. Fractions [d]–[f] are the shared variation between each predictor pair, and fraction [g] is the shared variation among all three predictors. Fraction [h] is the variation unexplained by the predictors.*

2.3.8 Modeled responses of ΔBIOV and interactions among predictors

The partial dependence plots (PDPs) illustrated how ΔBIOV responded to each predictor in the multivariate models (M1–M3; Figure 2.10). The partial responses of ΔBIOV to the M4 and M5 predictors were structurally similar to those of M3 and M1, respectively, and were omitted.

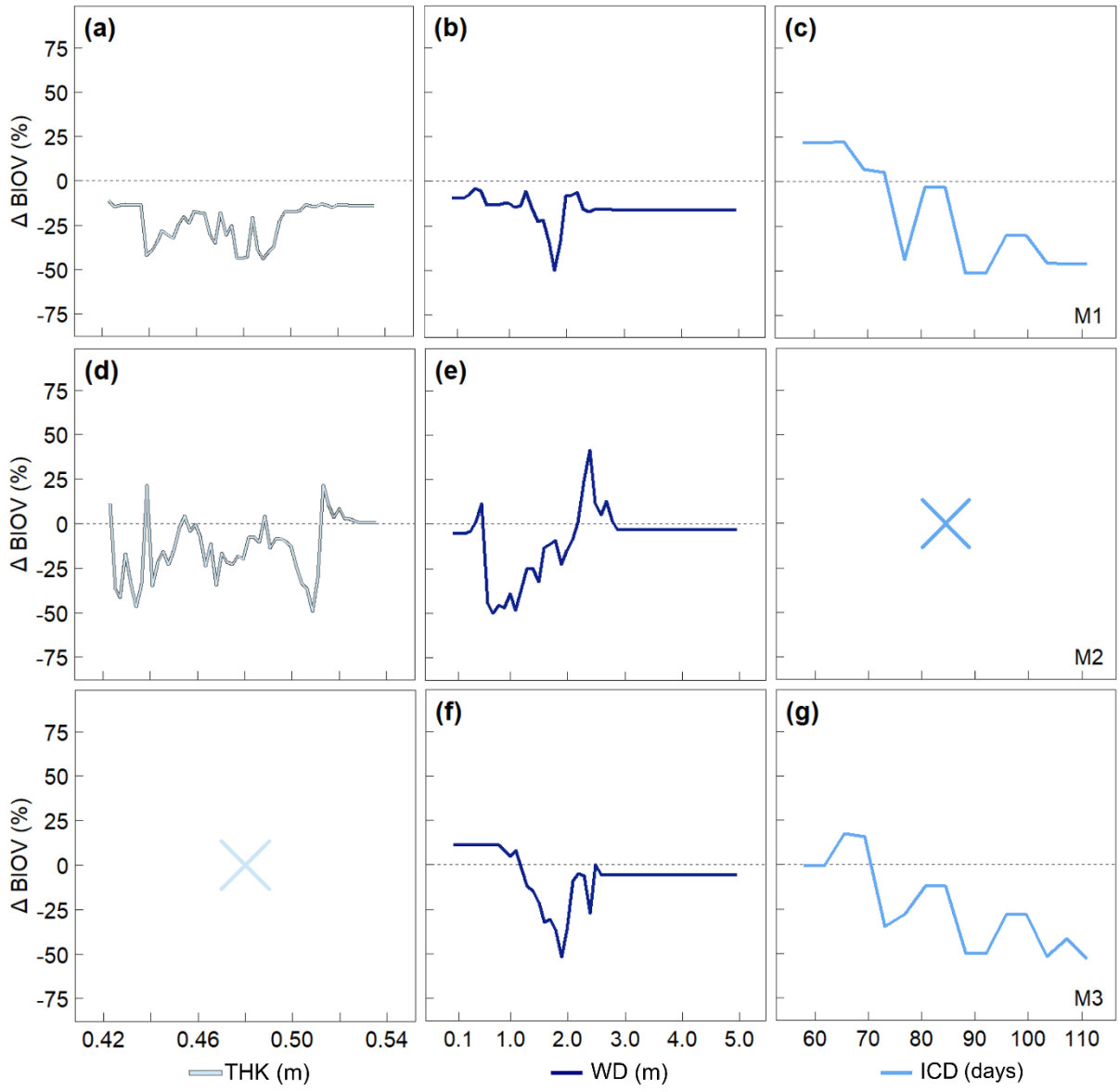


Figure 2.10. *Partial dependence plots for ΔBIOV by predictor (columns, colors) from the multivariate models M1, M2, and M3 (rows).* ***(a, d)****: THK;* ***(b, e, f)****: WD;* ***(c, g)****: ICD; The horizontal dashed line serves as a visual reference where ΔBIOV = 0. Predictors not included in a model are shown as crosses. PDPs were computed with the full range of each predictor's values shown in Figure 2.6; however, in the present figure, the y-axis limits were fixed to match the common range of marginal effects, while the ICD x-axis tick labels were rounded for visual clarity.*

The modeled response of ΔBIOV was mostly negative across the range of THK, and no clear trend was observed for this relationship in either M1 or M2 (Figure 2.10a, d). A clearer common pattern was found in response to WD (Figure 2.10b, e, f), as ΔBIOV began to plateau at depths between 2.6 and 2.9 m, beyond which no SAV was detected (Figure 2.6a, c). The WD partial responses for M1 (Figure 2.10b) and M3 (Figure 2.10f), which both include ICD as a predictor, were closely aligned, consistent with the relative importance of WD in these models (Figure 2.8). In both models, a downward shift from ~0 in the marginal effect of ΔBIOV was discernible in their respective WD plateau (−16% in M1; −5% in M3), whereas the ΔBIOV map showed near-zero values in areas deeper than ~3 m (Figure 2.6a, c), where ICD was generally shorter (Figure 2.6d). This downward shift was least pronounced in the PDP of M2 (−3%; Figure 2.10e), which suggests that the shift observed in the other multivariate models was partly an artifact of collinearity. Finally, the ΔBIOV partial relationship with increasing ICD appeared broadly negative in M1 and M3 (Figure 2.10c, g), and was overall the only relatively stable and monotonic one among the predictors, with higher predicted interannual biovolume loss at longer ice cover duration. The marginal responses were positive only when the ICD ranged from 58 to ~75 days, then alternated between dips and rebounds, a pattern that seemed to follow the sequential freeze-up progression illustrated in the ICD map (Figure 2.6d).

Considering the moderate collinearity of ICD with the other predictors (Figure 2.7), the possible effects of shared explanatory contribution on the shape of the PDPs from the multivariate models (Figure 2.10) were investigated using the ΔBIOV response curves predicted by univariate models (U1–U3; Figure 2.11). The response curve to THK in model U1 (Figure 2.11a) was somewhat similar to its PDP counterpart in M2 (Figure 2.10d). Meanwhile, the univariate response curve to WD (U2; Figure 2.11b) plateaued over the same depth range as in the multivariate plots (Figure 2.10b, e, f). There was still no clear overall pattern in the univariate response of ΔBIOV to THK, whereas for WD, the relationship shows a broad, albeit noisy, decrease in ΔBIOV with decreasing depth. Moreover, in both U1 and U2 models, the response curves appeared more irregular in shape than their corresponding PDPs, particularly beyond 0.50 m for THK and at WD less than 3 m. The ΔBIOV response to ICD (U3; Figure 2.11c) was negative with increasing duration, similar to the biovolume decline seen at shallow WD. This convergence in response was consistent with the Spearman's rank correlation between both predictors (Figure 2.7). The negative response of ΔBIOV to ICD in the univariate model was also more continuous over the range of

ICD values (Figure 2.11c) than in the multivariate models (Figure 2.10c, g). Lastly, no downward shift from ~0 was discernible in the univariate responses. Collinearity among the predictors in the multivariate models M1 and M3, both of which included ICD, thus appeared to have a notable influence on the shape of their predicted marginal effects. Nevertheless, several patterns recurred in the multivariate models regardless of which predictors were combined. For instance, dips were observed in the PDPs over the WD range of 0.6 to 2.1 m, although they were nonexistent in the corresponding univariate relationships.

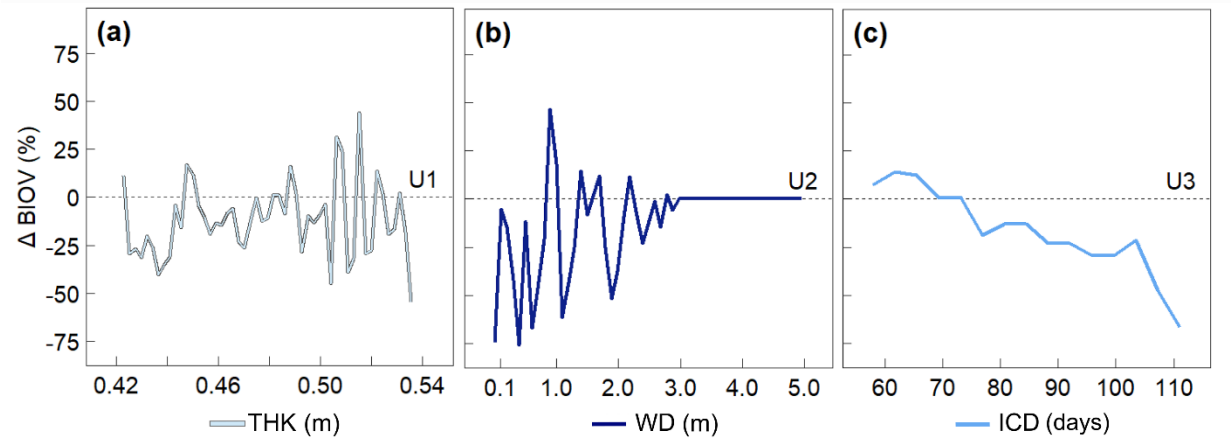


Figure 2.11. *Response curves for ΔBIOV by predictor (columns, colors) from the univariate models U1, U2, and U3.* ***(a)*** *THK;* ***(b)*** *WD;* ***(c)*** *ICD. Axis scales and tick values are identical to those in Figure 2.10 for comparison between multivariate and univariate model responses.*

The possible interacting effects of ice thickness (THK), ice cover duration (ICD), and water depth (WD) on ΔBIOV were explored using two-dimensional partial dependence plots (Figures 2.12 and S6) derived from the multivariate model M1, which explained most of the variation under spatial block cross-validation among the models tested (Table 2.2). Overall, predicted ΔBIOV values were negative across most of the response surface for the THK and WD pair (Figure 2.12a). The more negative ΔBIOV values appeared at intermediate depths (i.e., WD between ~1.2 and 2.3 m), especially at THK below ~0.50 m. Conversely, ΔBIOV values were less negative in shallow areas (WD below ~1.2 m), and became slightly positive for mid-range THK values. THK thus appeared to have a limited influence on ΔBIOV, restricted to shallow areas and without a consistent direction. A clearer pattern emerged in the response surface for the ICD and WD pair (Figure 2.12b), where predicted ΔBIOV values were generally positive up to ~75 days of ice cover, and negative above that duration. This marked transition in the response surface held over nearly the whole WD range, so the ΔBIOV response appeared driven mainly by ICD, with some influence

of WD on the magnitude rather than on the sign of the predicted change. At depths exceeding 2.8 m, both two-dimensional response surfaces (Figure 2.12a, b) showed horizontally oriented patterns across the THK and ICD ranges, respectively; thus, predicted ΔBIOV no longer varied with WD. Depths over 2.8 m, however, corresponded to 1.3% of grid cells in the WD map (Figure 2.6c). The remaining possible pair, ICD and THK, also the most collinear in M1 (Figure 2.7), is provided in the Supplementary Material (Figure S6), where nearly the same transition as in Figure 2.12b was visible along the ICD range, with little apparent change in ΔBIOV across the whole THK range.

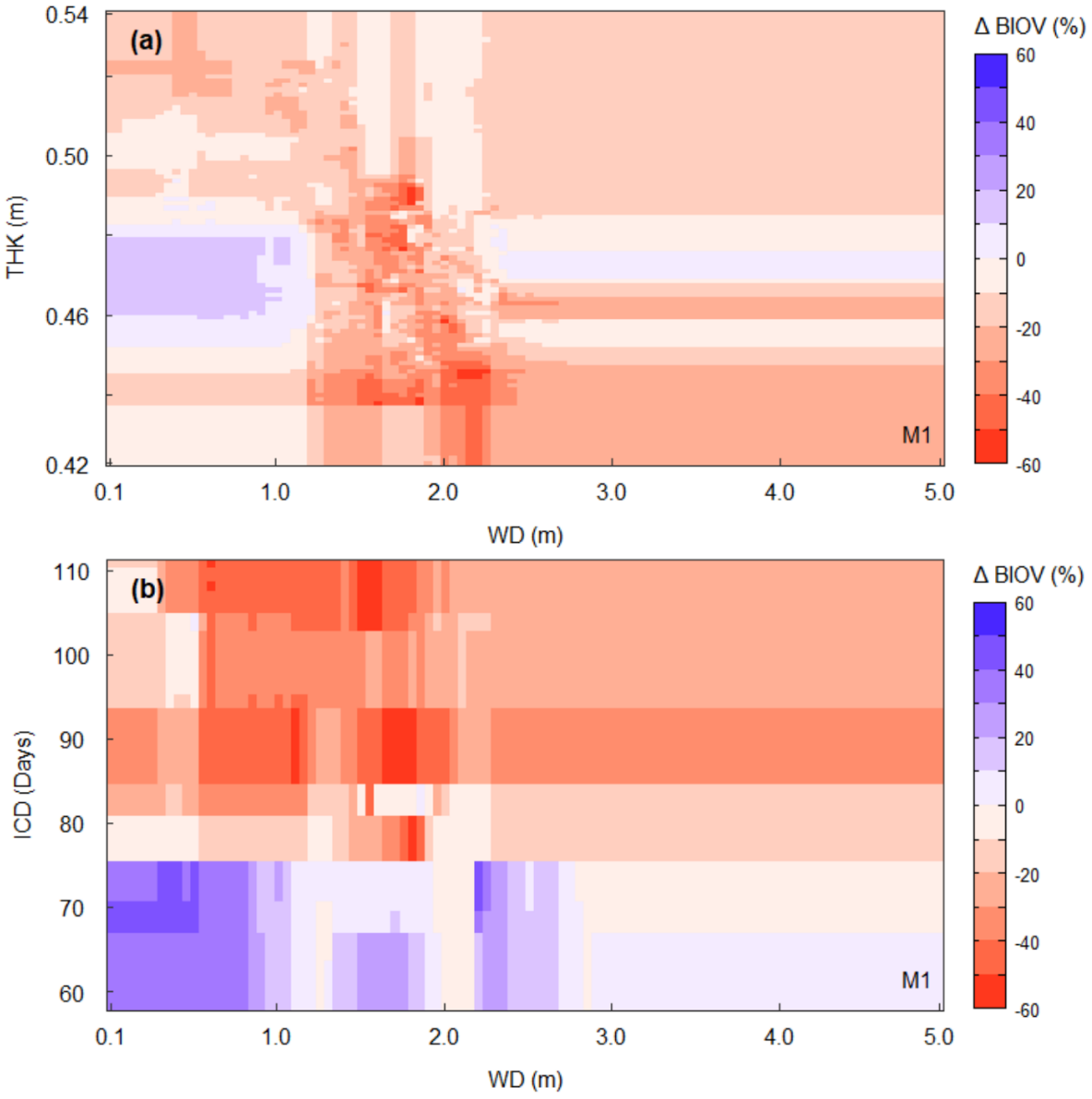


Figure 2.12. *Two-dimensional partial dependence plots of the modeled interactions between predictors and their effect on ΔBIOV (colors) from the multivariate model M1.* ***(a)*** *THK and WD;* ***(b)*** *ICD and WD. Partial dependence was computed over a 100 × 100 predictor grid.*

2.4 Discussion

Our study examined whether spatial variability in ice cover conditions (i.e., THK, ICD, and UIC as a derived descriptor) could contribute to the decline of SAV distribution and biovolume in Lake Saint-Pierre, acknowledging the inherent time-lag between ice-induced winter disturbance and the summer peak of SAV growth. The interseasonal framework also provided key insights into specific sub-ice conditions including bedfast ice, frazil ice, and the presence of SAV during winter (Figure 2.3) in a hydrologically complex floodplain lake where ice conditions are shaped by ice management activities (Figure 2.5). Our results provided little support for the hypothesis that greater ice thickness, especially in shallow areas, could lead to decreased SAV biovolume, whereas the hypothesis that a longer ice cover duration could have the same effect was partially supported. The best-performing RF model (M1), which associated ΔBIOV with ice-related predictors (i.e., THK, ICD) and WD as a hydromorphological driver, had a relatively moderate explanatory power (50% of the total variation explained) under spatial block cross-validation (Table 2.2). Between 2021 and 2022, ice thickness was associated with limited SAV biovolume change only when combined with shallow water depth (WD < ~1.2 m; Figure 2.12a), which may explain the absence of a clear ΔBIOV response to THK in the univariate and multivariate PDPs (Figures 2.10a and 2.11a). Meanwhile, longer ice cover duration was associated with more pronounced negative ΔBIOV over the same depth range, but this pattern also extended towards greater depth (Figure 2.12b). The PDPs of ICD also showed the most coherent overall relationship with ΔBIOV (Figures 2.10c and 2.11c). When included in a multivariate model, ICD ranked as the most influential predictor in terms of variable importance among the predictors tested (Figure 2.8), while its exclusive fraction of explained variation (0.21) exceeded those of WD (0.11) and THK (0.07) in the variation partitioning analysis (Figure 2.9). Despite ICD's apparent dominance, disentangling the exclusive fractions of explained variation proved difficult due to the influence of collinearity and the suppression effects observed among predictors.

2.4.1 Spatial datasets: reliability of hydroacoustic, GPR, and satellite sources

Although the role of lake ice cover conditions on the spatial distribution of SAV has been hypothesized (Morin & Champoux, 2006; Laporte et al., 2023), the spatial association between winter ice cover conditions and growing-season SAV responses had not been tested yet.

Considering the widespread decline of SAV in lakes worldwide (Botrel & Maranger, 2023), and the long-term degradation of littoral habitats at LSP (Hudon et al., 2018; Giacomazzo et al., 2020), our interseasonal framework, which combined summer hydroacoustic surveys with winter GPR and satellite-based ice measurements, could help investigate year-round drivers relevant to SAV conservation efforts. The hydroacoustic-derived ΔBIOV map showed a small but widespread decline, with pronounced spatial variability (Figure 2.6a). Biovolume gains were mainly seen at the confluence with the Tardif channel (Figure 2.1b) and in areas where the Saint-François and Yamaska water masses are known to converge (e.g., Hudon & Carignan, 2008). Moreover, the magnitude of ΔBIOV decline was notable across most of the study site, typically ranging from −10 to −30%. As shown by Botrel et al. (2022), who measured interannual variability in SAV biomass at the same study site between 2012 and 2017, consecutive years do not always follow similar trends. They reported that growing-season conditions such as water level, temperature, and nutrient inputs drove up to sixfold year-to-year differences in maximum biomass. The two hydroacoustic survey years in our study differed markedly in spring hydrological conditions. For instance, water levels exceeded 1.5 m (i.e., near the upper limit of yearly winter water levels) for 105 days during the spring flood in 2022, compared to only 13 days in 2021 (Figure S1). The longer spring flood duration in 2022 may therefore partly account for the widespread decline in ΔBIOV, given that sustained higher water levels might have reduced light availability, a primary driver of SAV growth (Giacomazzo et al., 2020). The 2022 survey was also conducted a week earlier than in 2021, perhaps further limiting the time available for SAV growth. Nevertheless, the depth range (~2.9 m) over which SAV biovolume was detected at our study site (Figure 2.11b) nearly corroborated the colonization depths (~3.2 m) recently reported from camera-based surveys at LSP (Laporte et al., 2023). The discrepancies between our cross-validated interpolated water depth map (Figure 2.6c) and observed values at borehole locations (Figure S4) can be attributed to measurement differences between methods. The echosounder underestimated depth by 0.09–0.15 m, whereas the weighted tape used at borehole locations was subject to tilting under flow and penetration in soft sediments, introducing ~0.20 m of uncertainty. The prediction errors reported in Table 2.1 also propagate to the derived under-ice clearance, since UIC was calculated from the interpolated WD and THK rasters. Hydroacoustic surveys, while well suited to detect SAV occurrence, were shown to overestimate biovolume by 9% relative to manual field observations using the same system as in our study (Helminen et al., 2019). However, the authors noted that

this bias did not vary significantly with vegetation abundance. The proportion of grid cells with minimal ΔBIOV change (i.e., < ±5%; Figure 2.6a) may thus arise in part from hydroacoustic measurement uncertainty rather than from a true ecological signal. The interpolation uncertainty of our yearly BIOV maps was not assessed, given that the automated kriging in BioBase EcoSound operates with non-user-accessible geostatistical parameters and does not generate prediction error estimates (Navico Inc., 2014). Nonetheless, kriging of biovolume has shown accurate prediction in freshwater lakes (Valley et al., 2005). Future studies would benefit from performing user-controlled kriging with exported point data to quantify prediction uncertainty.

On the winter aspect of our framework, both the GPR-informed ice thickness map (Figure 2.6b) and observed values (0.48 ± 0.05 m) at borehole locations (Figure 2.3) were within the range of 0.30–0.65 m (mean: 0.49 m) previously reported for LSP by Armellin (2006). Although GPR surveys have shown accurate freshwater ice thickness measurements (MAE: 0.03–0.05 m) relative to co-located borehole observations in other studies (e.g., Galley et al., 2009; Kämäri et al., 2017; Fu et al., 2018), our boreholes and GPR transects were not systematically co-located and both were limited to areas accessible under safe working conditions. Our cross-validated interpolated ice thickness compared with observed borehole values also yielded a low MAE of 0.036 m (Figure S5), although the corresponding R^2 was low (0.27; Table 2.1), a result that stems from the limited variance among borehole observations and from the smoothing inherent to kriging, rather than from poor predictive accuracy. The thin snow cover (0.07 ± 0.05 m), though unresolvable at the 500 MHz GPR frequency (Galley et al., 2009), inevitably contributed to the interpolation uncertainty. Higher-frequency GPR antennas (i.e., 1000 MHz) could improve the vertical resolution needed to resolve the snow-ice interface (e.g., Pouw et al., 2023). The EBKRP approach, which bypasses the need for radar velocity calibration, may offer a promising avenue for ice thickness mapping in hydrologically complex environments with variable ice cover properties if several boreholes or ice cores are obtainable. Given the need to correct interpolation striping artifacts inherent to the transect sampling layout (e.g., Knadel et al., 2015), future GPR surveys could instead benefit from a grid-based coverage with reduced spacing between survey transects. Finally, regarding the satellite-derived ice cover duration map (Figure 2.6d), per-scene classification accuracy was high during midwinter, but lower in the freeze-up and break-up phases (Figure 2.5), when clouds were present or confusion between ice and water classes increased. Cloud-masked or revised pixels represented about 5% of the lake-wide area. This per-scene

classification workflow was tedious, however, and would need to be automated for any future multi-year ICD mapping effort.

2.4.2 Conditional effects of ice thickness on SAV biovolume change

At our study site, ice thickness alone did not appear to exert a detectable direct effect on ΔBIOV, as seen in the univariate response curves (Figure 2.11a). Interpretations of THK should nonetheless be considered in light of the low cross-validation R^2 (0.27) of the interpolated ice thickness map (cf. Section 2.4.1). The pairwise correlation matrix showed only a weak relationship between THK and ΔBIOV (Figure 2.7); similarly, this predictor's exclusive fraction of explained variation was the smallest among all predictors in model M1 (Figure 2.9). The univariate RF model including only THK (U1) also failed to generalize to spatially independent blocks in predicting ΔBIOV (Table 2.2). This weak overall relationship persisted in the two-dimensional response surface (Figure 2.12a), where ΔBIOV values changed with THK only in shallow areas (WD < ~1.2 m), but without a consistent direction across the THK range. Our results therefore provided little support for the hypothesis that areas with greater ice thickness would coincide with a more negative interannual change in SAV biovolume, even when water depth was shallower (Figure 2.12a). This result was perhaps unsurprising given that our hypothesis was mostly formulated from indirect evidence of ice-driven disturbance on aquatic and riparian organisms (e.g., Stickler & Alfredsen, 2009; Lind et al., 2014), as well as theoretical considerations of lake ice dynamics (e.g., Kirillin et al., 2012; Leppäranta, 2015).

The limited individual effect of THK may thus reflect a more fundamental ecological aspect, namely the biological exposure of SAV to ice-related disturbance and species-dependent overwintering strategies. Although we did not assess SAV species composition from our hydroacoustic surveys, *Vallisneria americana* has been reported in recent years as the dominant species within LSP (Laporte et al., 2023). Previous ecophysiological work by Jarvis and Moore (2008) documented the reproductive strategies of *Vallisneria americana* in a system at lower latitude than LSP (i.e., the Chesapeake Bay, eastern USA), where populations were maintained interannually primarily through clonal reproduction via overwintering buds. Therefore, at LSP's northern latitude with a colder climate, most other SAV species were also expected to overwinter as dormant propagules at or near the sediment surface. Adamec (2018) describes this as an ecological strategy used by aquatic plants to escape being frozen and embedded in ice.

Ecological consequences of thick ice for aquatic organisms have been reported in other lakes, where ice was markedly thicker than at LSP. Arp et al. (2022) observed that, in lakes of the Arctic Coastal Plain, ice thickness can exceed 1.9 m by the end of winter, and in shallow areas, bedfast ice eliminates under-ice habitat. In contrast, mapped ice thickness at our study site (Figure 2.6b) was at most 0.54 m and relatively homogeneous with a range of 0.12 m, which was not sufficient for ice to reach the lakebed, thereby preventing bedfast conditions at the time of our survey. Thus, SAV overwintered under similar ice thickness regardless of location. This apparent homogeneity of ice thickness might itself be explained by the ice dynamics (Hicks, 2009; Kirillin et al., 2012) inherent to LSP as a hydrologically complex fluvial lake (Hudon & Carignan, 2008). Ice was generally thicker in shallow nearshore areas (Figure 2.6b, c), typically less exposed to strong flow, but locally as thick in deeper areas farther from the shore near the observed longitudinal crack (Figure 2.6b, f). This similar outcome in thickness is probably due to thermodynamic ice thickening characteristic of sheltered nearshore conditions (Kirillin et al., 2012), whereas hummocky ice accumulation from upstream drifting ice floes, followed by thermal thickening (Hicks, 2009), rather characterizes flow- and wind-exposed areas farther from the shore. The additional ice layer encountered beneath the ice cover at TB1, separated by an intervening water layer (Figure 2.6b), may accordingly point toward such past ice accumulation processes (e.g., hummocky ice, hydraulic thickening) from hydrodynamic forces.

Despite relatively homogeneous ice thickness across the study site and no observed bedfast ice conditions, under-ice clearance was minimal in some areas (Figure 2.6e), though it was higher than 0.42 m over most of the site during the GPR winter survey. Under-ice clearance was globally almost entirely determined by water depth ($r = 0.99$; Figure 2.7), because water depth varied much more than ice thickness across the studied area. However, in shallow areas (< 1m) spatial variation in ice thickness becomes more important in driving under ice clearance and could expose SAV, to some extent, to freezing or physical damage, such as scouring during ice cover freeze-up or break-up (Lind et al., 2014). There is also a risk that a decline in water levels during winter, driven by hydroclimatic variability, might exacerbate this exposure by further reducing under-ice clearance. Carmignani and Roy (2017), in a synthesis of winter drawdown effects on lake littoral zones, also noted that drawdowns can expose perennial SAV species (e.g., *Potamogeton* spp.*)* to dewatering, desiccation, and freezing. The daily water level measured at LSP (Figure S1) relative to the hydrometric station (cf. Section 2.2.4) was 1.01 m at the time of the GPR survey (February 14–15,

2022), whereas it had previously dropped to 0.77 m on January 28, 2022, which was the minimum during the ice-covered period starting in late December (Figure 2.5). Our UIC map (Figure 2.6e) therefore might overestimate clearance conditions on January 28 by approximately 0.24 m, assuming similar ice thickness. Sustained winter drawdown was not observed, but the small amplitude of water-level variations during freeze-up and midwinter was expected given the regulation of inflows by hydraulic infrastructure along the St. Lawrence River (Hudon & Carignan, 2008; Clamen & Macfarlane, 2018). At the lowest winter water level, under-ice clearance in the shallowest areas (1% of grid cells) was reduced to approximately 0.18 m, though bedfast ice remained negligible (< 0.2% of grid cells). Hence, we did not directly detect ecological effects of bedfast ice on ΔBIOV at our study site. Overwintering SAV was nonetheless visually observed at 4 of the 21 borehole locations where the lakebed was visible (out of 33 boreholes inspected with cameras), confirming that SAV persisted beneath the ice cover. Visible stems and verticillate shoots at some locations (Figure 2.3) may correspond to *Ceratophyllum demersum,* a species previously reported at LSP during summer (Laporte et al., 2023). This observation was in accordance with Adamec (2018), who reported that this species can overwinter through dense shoot tips with little-modified leaves. Stem fragments were sometimes found frozen into the ice cover, though no notable visible damage to this species was observed.

Overall, the conditional association between THK and ΔBIOV in shallow areas was weak (Figures 2.9 and 2.12a), and neither THK nor WD generalized spatially in their respective univariate models of ΔBIOV (Table 2.2). The non-generalization of THK might be explained by the difference in ice thickening processes, rather than by a direct ecological effect on ΔBIOV, and thus may explain the weak conditional pattern seen in Figure 2.12a. As for WD, it did not generalize spatially because the amplitude of interannual change in biovolume can be opposite at similar depths under different water mass properties and flow conditions (e.g., Vis et al., 2003), which are known drivers of SAV distribution (Hudon et al., 2018; Laporte et al., 2023). Considering the non-generalization of THK in U1 and the suppression effects between WD and THK in the variation partitioning (Figure 2.9), ice thickness may have acted as a weak proxy for shared morphological gradients (i.e., WD) and related hydrodynamic exposure inherent to ice formation processes (Kirillin et al., 2012). The comparison between modeled responses of ΔBIOV in PDPs (Figure 2.10) versus univariate response curves (Figure 2.11) supported the argument that THK had a possible weak proxy effect, especially visible for WD in model M2, which was in

closer agreement with the ΔBIOV map (Figure 2.6a). However, the WD pattern was more ambiguous in multivariate models M1 and M3, considering the observed distortion (i.e., downward shift) in their marginal effects. This can be attributed to a recognized interpretability bias in RF models, also visible in the permutation-based variable importance (Figure 2.8; VI) when correlated predictors share explanatory power (Nicodemus et al., 2010). In our case, the relative importance of WD, the predictor most strongly correlated with ICD, dropped from 1.00 in M2 to 0.61 in M1, a larger decrease than for THK (0.92 to 0.65), although there is no consensus on how correlated predictors affect VI (Gregorutti et al., 2017). The effect of shared explanatory power was also apparent in the two-dimensional ΔBIOV response surfaces. For instance, the surface for THK and WD computed from model M2, provided in the Supplementary Material (Figure S7), showed a more pronounced contrast across the THK range than in M1 (Figure 2.12a), especially in shallow areas. This difference supports our interpretation of THK as a weak proxy, since THK carried part of the information that ICD accounted for in M1.

2.4.3 Ice cover duration and concurrent growing-season drivers of SAV

Our results partially supported the hypothesis that a longer ice cover duration would be negatively associated with ΔBIOV. In contrast with THK, the pairwise correlation matrix showed the strongest relationship between ICD and ΔBIOV (Figure 2.7), and ICD's exclusive fraction of explained variation was the highest among all predictors in M1 (Figure 2.9). Moreover, ICD in its univariate model (U3) partly generalized to spatially independent blocks in predicting ΔBIOV (Table 2.2), while sharing the highest proportions of explained variation with the other predictors (Figure 2.9). We found a decreasing pattern between ICD and ΔBIOV, visible in both the marginal effects of the multivariate models (Figure 2.10) and the univariate response curve (Figure 2.11). Therefore, ICD coincided with the spatial gradient of ΔBIOV across the study site, but attributing this association to a direct effect of ice cover duration on ΔBIOV could not be clearly established. This was again somewhat expected because of the inherent SAV overwintering strategies and the factors controlling dormancy break (e.g., Rybicki & Carter, 2002; Adamec, 2018). Considering the shared explained variation with the other predictors, and the known influence of water depth and hydrodynamic conditions on freeze-up and break-up timing (Kirillin et al., 2012), ICD may also have acted as a proxy of hydromorphological conditions. In contrast with THK, whose homogeneous thickness across the study site arises from contrasting thickening processes in flow-

sheltered and flow-exposed areas (cf. Section 2.4.2), ice cover duration decreased with potential hydrological exposure and may therefore have captured more of the spatial variability in flow conditions.

Our hypothesis mainly invoked prolonged low light limitation beneath the ice as the underlying mechanism linking ICD to ΔBIOV. This premise was motivated by studies on seasonally frozen lakes showing that white ice thickening and snow accumulation reduce under-ice light availability (e.g., Weyhenmeyer et al., 2022), with documented effects on aquatic photoautotrophs. Bramburger et al. (2023), for instance, found that phytoplankton primary productivity decreased under snow-covered ice. Snow cover at LSP, however, was minimal and the underlying ice stratigraphy was dominated by black ice (81.8 ± 9.0%), conditions conducive to light transmission (Figure 2.3). Although *Ceratophyllum demersum*, a SAV species capable of maintaining minimal physiological activity (Spencer & Wetzel, 1993), was present at LSP, previous studies have shown that light availability in the water column plays a secondary role compared to water temperature in triggering dormancy break. SAV species mostly overwinter through dormant buds (Jarvis & Moore, 2008; Adamec, 2018), and thus do not necessarily require light to initiate regrowth. Rybicki and Carter (2002), in an experimental study, found that *Vallisneria americana* winter buds (e.g., tubers) germinated at a water temperature of 13 °C regardless of light conditions. Moreover, they found that tubers could elongate for 6 weeks without light, and the species' tuber size (i.e., summer carbohydrate reserves) explained almost half of plant height the following spring. Ice cover duration could in principle influence dormancy break through spring water temperature. At LSP, however, sustained inflow during and after break-up would limit the persistence of local temperature differences, and we consider this pathway unlikely to explain the spatial association between ICD and ΔBIOV.

The effects of the preceding winter's ice thickness and ice cover duration on interannual changes in SAV biovolume remain difficult to isolate, given that several other growing-season environmental drivers are known to influence SAV distribution and biomass at LSP (Botrel et al., 2022). The spatial variability in ΔBIOV is most probably explained by the contrasting spring flood duration between survey years, and thus the longer period of higher water levels (Figure S1). Laporte et al. (2023) identified the clearer waters originating from the Great Lakes as a photic refuge. This refuge likely extended during the flood over the northeastern areas of our study site and could explain the biovolume gains observed in 2022 (Figure 2.6). Moreover, the convergence

of these clearer waters with nutrient-rich inputs from the Saint-François and Yamaska rivers may have provided a favorable balance of light, nutrient, and flow conditions for SAV growth. Conversely, biovolume decline in nearshore areas may reflect the lateral confinement of these more turbid southern tributary waters against the shoreline during the prolonged flood, which likely delayed SAV growth compared to 2021. Our study design, based on a single pair of SAV survey years and one ice season, thus cannot separate growing-season conditions from ice-related effects; multi-year monitoring would be needed to disentangle their respective contributions.

2.5 Conclusion

Investigating the physical and physiological effects of ice cover conditions on submerged aquatic vegetation is widely recognized as challenging (e.g., Lind et al., 2014), because little is known about SAV activity beneath the ice cover or the potential effects of ice on their interannual responses. Here, we provide an initial empirical assessment of ice cover conditions and SAV presence during winter. In doing so, we also begin to address long-standing hypotheses on the role of ice in shaping the SAV-devoid channels at LSP (e.g., Morin & Champoux, 2006). We further explored how potential ice-related disturbance is associated with interannual changes in SAV distribution the following summer, through an interseasonal framework of hydroacoustic and ground-penetrating radar surveys as well as satellite-based observations. We showed, by analyzing Random Forest regression models, how interannual changes in SAV biovolume were most strongly associated with ice cover duration among the predictors considered, and how the ice-related predictors were intertwined with one another and with the underlying hydromorphological conditions.

Our study provided little support for the hypothesis of a negative association between greater ice thickness and SAV biovolume change, whereas the hypothesis that a longer ice cover duration could have the same effect was partially supported. Ice thickness was related to biovolume change mostly in shallow areas and without a consistent direction, whereas ice cover duration showed a negative association across a broader depth range. Our borehole observations documented visible SAV beneath the ice cover at some locations, under-ice clearance that, though sometimes limited, remained above bedfast conditions, and an absence of frazil or anchor ice accumulation. Direct physical disturbance by ice was therefore an unlikely mechanism shaping SAV distribution at our study site. Similarly, we measured prevailing black ice conditions and minimal snow cover,

conditions conducive to light transmission. Considering the overwintering strategies of dominant SAV species (e.g., Rybicki & Carter, 2002; Adamec, 2018), prolonged low-light limitation was therefore an unlikely physiological mechanism linking ice cover duration to biovolume change at LSP. Concurrent growing-season drivers, shaped in particular by the markedly longer spring flood in 2022, may have influenced the spatial variability of biovolume, with increases farther from the shoreline and losses in nearshore areas.

However, the full model associating biovolume change with ice-related predictors was confounded by collinearity, as the predictors shared a considerable part of the explained variance, and thus partly acted as proxies for the hydromorphological gradient that drives ice formation processes (e.g., Kirillin et al., 2012). The interpolated ice thickness map also had a low cross-validation R^2, despite low absolute prediction errors. Moreover, ice thickness, water depth, and the derived under-ice clearance did not generalize to spatially independent blocks when considered alone. Whether spatial variability in ice cover conditions contributes to interannual change in SAV distribution independently of the hydromorphological gradient therefore remains only partly resolved, even though ice cover duration retained predictive performance across blocks. Our interseasonal framework provides a basis for broader investigations of ice-vegetation interactions in shallow fluvial lakes. Further characterization of lake ice thickness using a GPR-mounted drone or collaboration with the Canadian Coast Guard could provide new opportunities to expand spatial coverage and access areas precluded by variable and hazardous ice conditions. Monitoring hydrodynamic conditions beneath the ice cover, including frazil ice production, its transport pathways, and the lateral flow diversion associated with ice floe congestion at the first bend of the navigation channel, could help test the hypothesis that sub-ice flow processes shape the SAV-devoid channels. The addition of environmental predictors during spring and summer, e.g., water mass hydrological and physicochemical properties, could possibly help disentangle the effects of ice cover from SAV growing-season conditions. Emergent low marshes, which are more directly exposed to physical ice-related disturbance and also support critical habitat structure and nursery grounds for aquatic fauna at LSP during the spring flood (e.g., de la Chenelière et al., 2014), also warrant consideration for future investigations of ice-vegetation interactions. These investigations could benefit the long-term integrity of LSP littoral ecosystems.

2.6 Supplementary Material

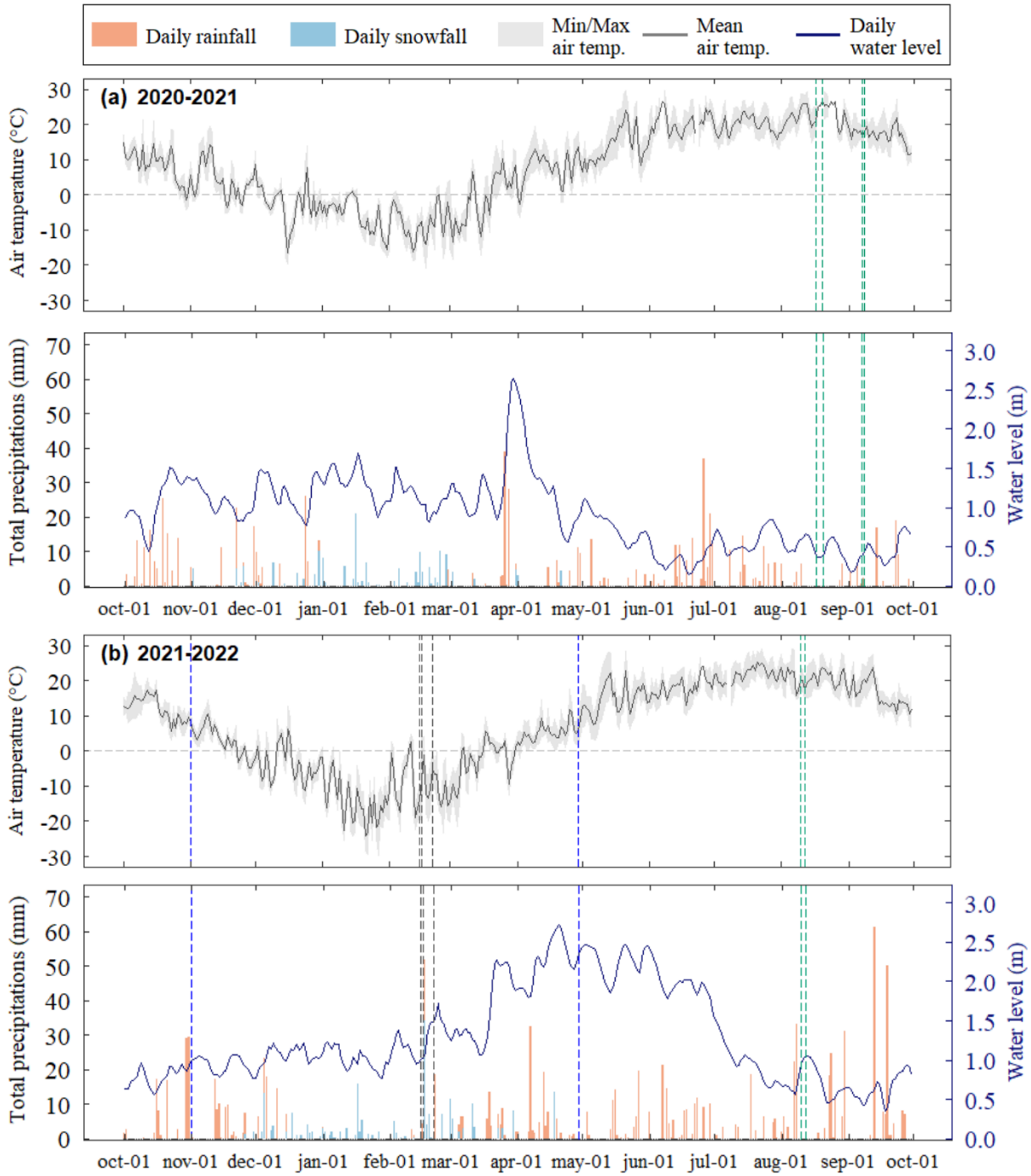


Figure S1. *Hydroclimatic conditions over each survey year.* ***(a)*** *2020-2021;* ***(b)*** *2021-2022. Mean air temperature (gray line), total rainfall (orange bars), total snowfall (light blue bars), and water level (dark blue line), all daily. Vertical green dashed lines indicate summer fieldwork dates. Vertical gray dashed lines in (b) indicate winter fieldwork dates, and vertical blue dashed lines delimit the ice season. Air temperature data: LSP station (ID 701LP0N); precipitation data: Pierreville station (ID 7026043); water level data: LSP hydrometric station (ID 15975).*

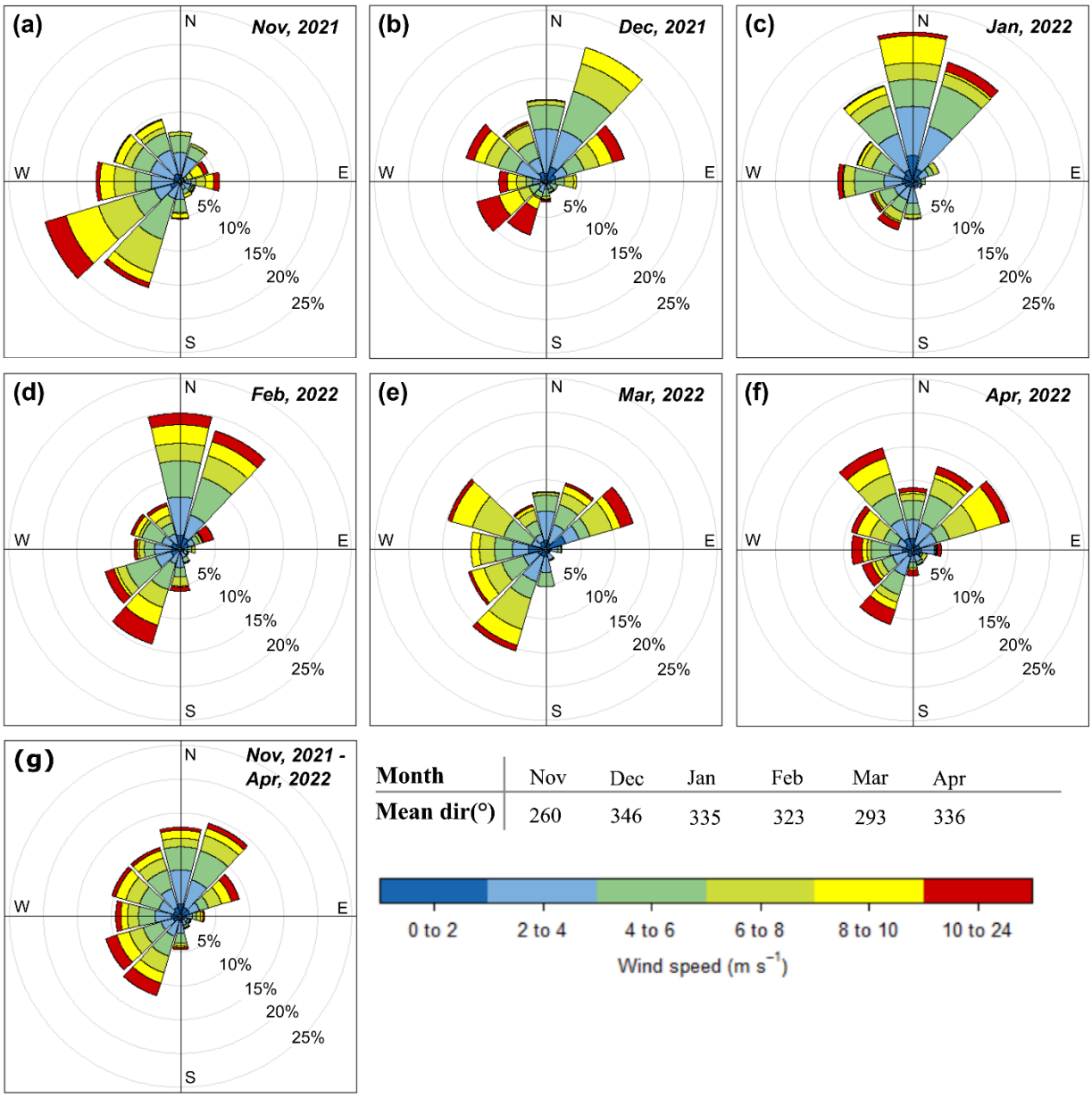


Figure S2. *Wind roses with wind direction frequency (% per 30° sector) and wind speed classes (m s⁻¹; upper bound included, note the wider upper class) from November 2021 to April 2022 (ice season). Panels (a)–(f) correspond to individual months, while panel (g) is the full ice season. The inset table reports the monthly mean wind direction (°). All data are from hourly records at the LSP climate station (ID 701LP0N; Environment Canada).*

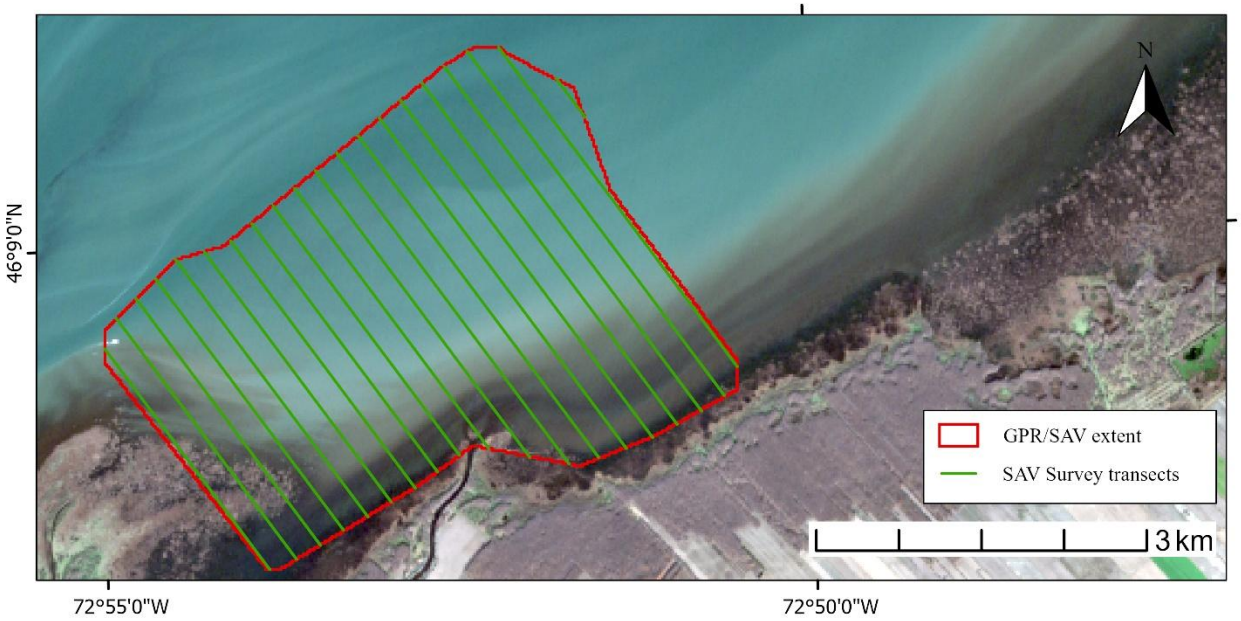


Figure S3. *Location of SAV survey transects in the southwestern portion of LSP. Basemap: Copernicus Sentinel-2 true-color imagery, November 11, 2021.*

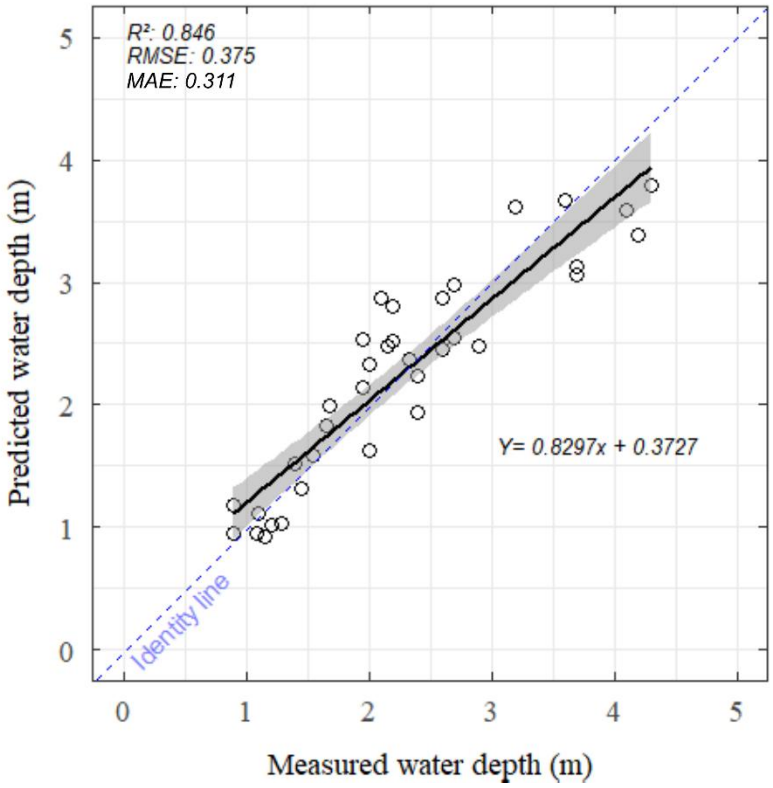


Figure S4. *Independent validation scatterplot of kriging predicted water depth (m), adjusted to daily water levels, against water depth measured at borehole locations during winter fieldwork (n=36). The 1:1 identity line (blue) and the regression line (black) are shown. Y: Regression equation; R²: coefficient of determination; RMSE: Root mean square error; and MAE: Mean absolute error.*

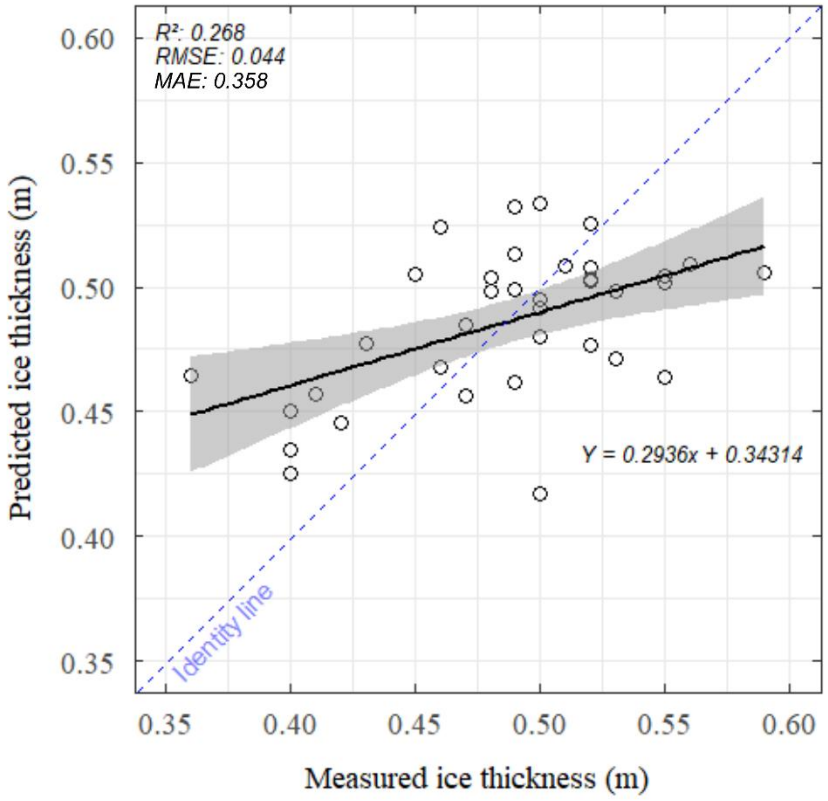


Figure S5. *Leave-one-out cross-validation scatterplot of kriging predicted ice thickness (m) against ice thickness measured at borehole locations (n=36). The 1:1 identity line (blue) and the regression line (black) are shown. Y: Regression equation; R²: coefficient of determination; RMSE: Root mean square error; and MAE: Mean absolute error.*

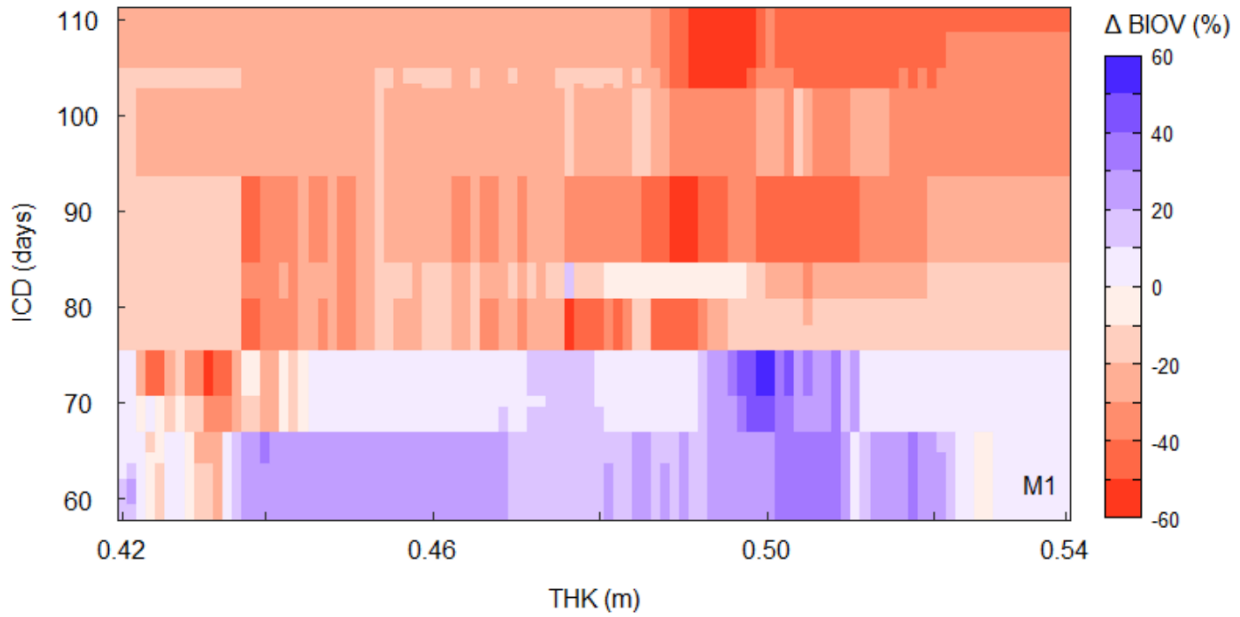


Figure S6. *Two-dimensional partial dependence plot of the modeled interaction between ICD and THK and its effect on ΔBIOV (colors), computed from M1 over a 100 × 100 predictor grid.*

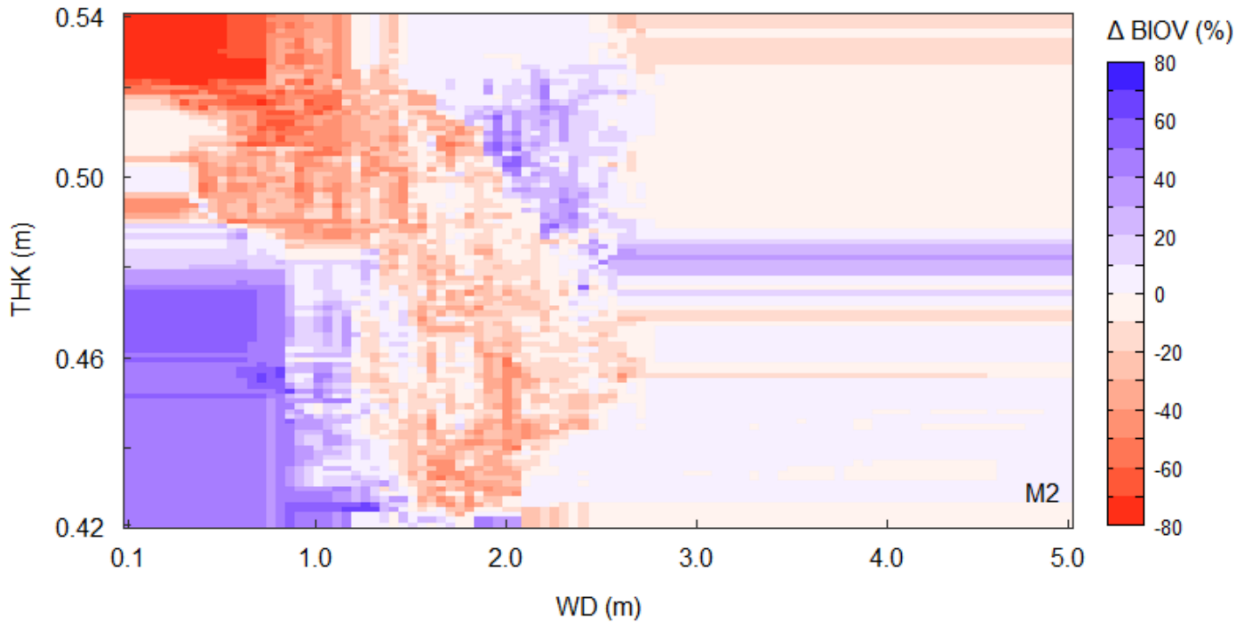


Figure S7. *Two-dimensional partial dependence plot of the modeled interaction between THK and WD and its effect on ΔBIOV (colors), computed from M2 over a 100 × 100 predictor grid. Note the wider color scale than in Figure 2.12 and Figure S6.*

Table S1. *Sentinel-2 scenes acquisition summary and per-class counts used for validation of ice-cover classification through confusion matrices.*

Dates	Cloud cover (%)	Revised (%)	Training samples (n)	Validation samples (n)	Predicted totals (fast ice/floes/water)	Reference totals (fast ice/floes/water)
2021-12-21**	0.00	0.31	491	203	(75 / 7 / 121)	(75 / 6 / 122)
2021-12-23	1.77	2.59	664	326	(69 / 49 / 208)	(74 / 43 /209)
2022-01-10*	0.00	0.15	578	256	(141 / 106 / 9)	(153 / 97 / 6)
2022-01-15*	0.00	0.00	511	218	(141 / 68 / 9)	(137 / 71 / 10)
2022-01-20*	0.00	2.47	502	197	(172 / 21 / 4)	(172 / 22 / 3)
2022-01-22*	1.59	5.78	489	251	(202 / 41 / 8)	(204 / 42 / 5)
2022-01-25	1.26	3.69	547	201	(168 / 20 / 13)	(168 / 21 / 12)
2022-01-30	0.00	1.70	520	233	(189 / 29 / 15)	(190 / 30 / 13)
2022-02-01	0.00	2.33	535	218	(178 / 22 / 18)	(176 / 24 / 18)
2022-02-09	0.00	1.86	512	241	(201 / 18 / 22)	(203 / 13 / 25)
2022-02-14	1.60	6.12	520	225	(186 / 29 / 10)	(178 / 35 / 12)
2022-02-24	0.00	1.78	527	226	(193 / 11 / 22)	(193 / 13 / 20)
2022-02-26	0.59	2.90	525	228	(185 / 31 / 12)	(181 / 35 / 12)
2022-03-03	0.00	2.09	525	228	(190 / 14 / 24)	(189 / 18 / 21)
2022-03-08**	0.00	1.84	536	217	(178 / 1 / 38)	(176 / 0 / 41)
2022-03-11**	0.00	1.15	517	235	(185 / 1 / 49)	(183 / 0 / 52)
2022-03-13	0.00	1.77	523	230	(163 / 19 / 48)	(162 / 18 / 50)
2022-03-16	0.62	4.03	508	245	(128 / 43 / 74)	(130 / 45 / 70)
2022-03-23	0.00	1.02	705	306	(118 / 32 / 156)	(119 / 22 / 165)
2022-03-28	0.00	2.88	708	293	(109 / 32 / 152)	(108 / 12 / 173)
2022-04-02	0.00	4.02	687	307	(92 / — / 215)	(99 / — / 208)
2022-04-05**	0.00	0.01	662	330	(70 / 3 / 257)	(70 / 2 / 258)
2022-04-10**	0.00	0.05	697	313	(29 / 3 / 281)	(24 / 0 / 289)
2022-04-12**	0.00	0.01	686	307	(28 / 2 / 277)	(21 / 0 / 286)

Notes. Revised = temporal gap fill (cloud-masked pixels) and channel-consistency correction in the navigation-channel (see Methods). Cloud cover and Revised are expressed as percentages of the LSP extent (370 km^2). "—" indicates no samples were available for that class on that scene. Total samples dataset was split 70/30 with a random stratified selection; per class training samples were not tracked.

**Predicted totals and reference totals (floes) n < 10; * (water) n < 10. Predicted totals are confusion matrices n per classes row and reference totals are n per column; both are from the corresponding (n) validation samples. Percent values are rounded to 0.01%.

Table S2. *Per-scene classification performance on independent validation samples. OA: overall accuracy, K: kappa coefficient, PA: Producer's accuracy, UA: User accuracy.*

Dates	OA (%)	K	Fast ice:		Floes:		Water:	
			PA (%)	UA (%)	PA (%)	UA(%)	PA (%)	UA(%)
2021-12-21	98.52	0.97	98.70	98.70	83.30	71.40	99.20	100.00
2021-12-23	94.48	0.89	90.50	97.10	86.00	75.50	97.60	98.10
2022-01-10	92.58	0.86	90.20	97.90	95.90	87.70	100.00	66.70
2022-01-15	83.94	0.67	89.10	86.50	73.20	76.50	90.00	100.00
2022-01-20	97.46	0.89	98.80	98.80	86.40	90.50	100.00	75.00
2022-01-22	97.21	0.91	98.50	99.50	90.50	92.70	100.00	62.50
2022-01-25	98.51	0.95	100.00	100.00	90.50	95.00	91.70	84.60
2022-01-30	98.71	0.96	99.50	100.00	93.30	96.60	100.00	86.70
2022-02-01	98.17	0.94	100.00	98.90	87.50	95.50	94.40	94.40
2022-02-09	96.27	0.87	99.00	100.00	84.60	61.10	80.00	90.90
2022-02-14	90.22	0.70	97.20	93.00	60.00	72.40	75.00	90.00
2022-02-24	99.12	0.97	100.00	100.00	84.60	100.00	100.00	90.90
2022-02-26	98.25	0.95	100.00	97.80	88.60	100.00	100.00	100.00
2022-03-03	98.25	0.94	100.00	99.50	77.80	100.00	100.00	87.50
2022-03-08	98.62	0.95	100.00	98.90	0.00	0.00	92.70	100.00
2022-03-11	98.72	0.96	100.00	98.90	0.00	0.00	94.20	100.00
2022-03-13	90.87	0.80	100.00	99.40	44.40	42.10	78.00	81.30
2022-03-16	95.10	0.92	96.90	98.50	84.40	88.40	98.60	93.20
2022-03-23	92.16	0.86	93.30	94.10	81.80	56.30	92.70	98.10
2022-03-28	86.34	0.77	97.20	96.30	33.30	12.50	83.20	94.70
2022-04-02	95.11	0.89	88.90	95.70	—	—	98.10	94.90
2022-04-05	98.48	0.96	98.60	98.60	50.00	33.30	98.80	99.20
2022-04-10	97.44	0.84	100.00	82.80	0.00	0.00	97.20	100.00
2022-04-12	96.42	0.77	95.20	71.40	0.00	0.00	96.50	99.60

Notes. OA, PA and UA are reported as percentages; K is unitless. Class-wise accuracy metrics (PA, UA) are shown for each class. "—" indicates no reference (validation) samples were available for that class and date. Omission error = 100% − PA; commission error = 100% − UA.

Table S1 and Table S2 are complementary and can be used to build confusion matrices.

Table S3. *Threshold values of daily ice cover fraction (%) used to define lake ice phenological phases at Lake Saint-Pierre, based on the methodology proposed by Yang et al. (2019).*

Phenological Phases	**Ice fraction criteria**	**Acronyms**
Freeze-up start	First day > 20 %	FUS
Freeze-up end	First day > 80 %	FUE
Freeze-up duration	Freeze-up end - start	FUD
Break-up start	First day < 80 %	BUS
Break-up end	First day < 20 %	BUE
Break-up duration	Break-up end - start	BUD
Complete frozen duration	BUS - FUE	CFD
Frozen duration	BUE - FUS	FD

CHAPITRE III

CONCLUSION GÉNÉRALE

3.1 Retour sur la démarche et les principaux résultats

Les communautés de végétation aquatique submergée (VAS) contribuent à de multiples fonctions écologiques dans les écosystèmes lacustres (e.g., Thomaz et al., 2025). Ces communautés ont toutefois décliné dans de nombreux lacs à l'échelle mondiale, en réponse aux pressions anthropiques qui limitent la disponibilité en lumière dans la colonne d'eau (Botrel et Maranger, 2023). Dans le cas du lac Saint-Pierre (LSP), le déclin de la VAS observé au cours des dernières décennies a jusqu'à maintenant surtout été attribué aux pressions issues du bassin versant pendant la saison de croissance (i.e., mai à septembre), notamment l'augmentation de la turbidité, les apports de nutriments et les altérations hydro-morphologiques liées à la navigation commerciale (Hudon et al., 2018; Giacomazzo et al., 2020; Laporte et al., 2023). Cependant, la présence persistante de chenaux dépourvus de VAS dans des zones par ailleurs favorables à sa croissance a conduit à envisager un rôle additionnel des conditions du couvert de glace, par des contraintes physiques ou physiologiques potentielles sur les structures végétatives hivernantes (Morin et Champoux, 2006; Lind et al., 2014). Ce rôle demeure toutefois largement inexploré en raison des défis conceptuels et logistiques associés à l'étude de la VAS pendant l'hiver (Block et al., 2019). Pour combler une partie de cette lacune empirique, une approche combinant relevés hydroacoustiques estivaux, mesures par géoradar et télédétection satellitaire a été mise en place.

Dans une démarche exploratoire, ce mémoire visait à examiner, dans une perspective d'effets saisonniers différés, les relations spatiales entre les conditions du couvert de glace hivernal et la variation interannuelle du biovolume estival de la VAS. L'étude a été menée dans un secteur du sud-ouest du LSP, portion du lac où subsiste aujourd'hui l'essentiel de la VAS (Laporte et al., 2023). Plus précisément, l'épaisseur de glace (THK) et la durée d'englacement (ICD) ont été mises en relation avec la variation interannuelle du biovolume (ΔBIOV), en examinant comment la profondeur d'eau (WD), une variable qui module à la fois les processus de formation de la glace

et la croissance de la VAS (Hudon et al., 2000; Kirillin et al., 2012), a pu intervenir dans cette association, notamment par l'espace libre sous la glace (UIC).

La distribution spatiale de ΔBIOV entre les étés 2021 et 2022 a d'abord été cartographiée à l'aide de mesures hydroacoustiques réalisées en août, au maximum saisonnier de la VAS. Les conditions du couvert de glace de la saison hivernale intercalée entre ces deux campagnes estivales ont ensuite été caractérisées. L'épaisseur de glace a été cartographiée à son maximum saisonnier, en février 2022, à partir de mesures par géoradar combinées à des observations ponctuelles par forages, tandis que la durée d'englacement a été estimée à partir d'une série temporelle d'images satellitaires classifiées. De plus, la profondeur d'eau a été cartographiée à partir de l'interpolation de données bathymétriques du Service hydrographique du Canada, puis combinée à l'épaisseur de glace utilisée pour calculer l'espace libre sous son couvert. Enfin, le changement de biovolume et les variables cryosphériques et hydro-morphologiques ont fait l'objet d'une analyse descriptive à une résolution commune de 20 m. Une modélisation par une approche de forêts aléatoires a ensuite été adoptée afin d'analyser la contribution relative des prédicteurs et de visualiser leurs effets marginaux ainsi que leurs interactions. Les objectifs spécifiques ont ainsi tous été atteints.

Les modèles de forêts aléatoires ont montré que le changement interannuel du biovolume était le plus fortement associé à la durée d'englacement parmi les prédicteurs considérés, et que les variables prédictives cryosphériques étaient étroitement liées entre elles ainsi qu'aux conditions hydro-morphologiques sous-jacentes. Les résultats du projet n'ont soutenu que faiblement l'hypothèse d'une association négative entre une plus grande épaisseur de glace et le changement de biovolume, tandis que l'hypothèse selon laquelle une durée d'englacement plus longue entraînerait un effet analogue a été partiellement soutenue. L'épaisseur de glace n'était liée au changement de biovolume que dans les zones peu profondes, mais sans tendance monotone sur la gamme d'épaisseurs de glace cartographiée, alors qu'une association négative a été trouvée pour la durée d'englacement sur presque toute la gamme de profondeurs d'eau. Les observations sous le couvert de glace, réalisées aux sites de forage, ont aussi révélé de la VAS visible à certains endroits, un espace libre sous la glace localement réduit, mais sans contact entre le couvert et le substrat, ainsi qu'une absence d'accumulation de frasil ou de glace de fond ancrée sur les structures végétatives. Ces constats suggèrent donc qu'une perturbation physique directe par la glace était peu probable en tant que mécanisme structurant la distribution de la VAS dans le secteur considéré. Par ailleurs, la glace noire représentait la majeure partie de l'épaisseur de glace mesurée, sous une

couche de neige globalement mince, soit des conditions favorables à la transmission lumineuse vers la colonne d'eau (e.g., Weyhenmeyer et al., 2022). Compte tenu des stratégies d'hivernage des espèces dominantes de la VAS (e.g., Rybicki et Carter, 2002; Adamec, 2018), la photolimitation prolongée demeure également un mécanisme physiologique peu probable pour expliquer l'association observée entre la durée d'englacement et le changement de biovolume au site d'étude. Les facteurs concomitants de la saison de croissance, marqués en particulier par une crue printanière nettement plus longue en 2022 qu'en 2021, ont vraisemblablement influencé la variabilité spatiale du changement de biovolume, avec des gains observés au large vers le centre du lac et des pertes près des rives.

Les résultats obtenus reflètent ainsi la portée d'un dispositif d'observation du changement de biovolume s'appuyant sur deux campagnes estivales séparées par une seule saison hivernale. Le modèle complet a été confondu par la colinéarité inhérente aux prédicteurs cryosphériques, ceux-ci partageant une part considérable de la variance expliquée et agissant en partie comme des proxys du gradient hydro-morphologique qui régit les processus d'englacement (e.g., Kirillin et al., 2012). La carte interpolée d'épaisseur de glace présentait par ailleurs un faible R^2 de validation croisée, malgré de faibles erreurs absolues de prédiction. De plus, les associations impliquant l'épaisseur de glace, la profondeur d'eau et l'espace libre sous la glace qui en découle ne se généralisaient pas d'un secteur à l'autre du site d'étude lorsque ces prédicteurs étaient considérés seuls. La question de recherche qui visait à déterminer si la variabilité spatiale des conditions d'englacement contribue au changement interannuel de la distribution de la VAS indépendamment du gradient hydro-morphologique demeure partiellement résolue, même si la durée d'englacement a conservé une part de sa performance prédictive d'un secteur à l'autre du site.

3.2 Retombées et perspectives

Ce projet a mis en évidence la faisabilité d'un cadre méthodologique intersaisonnier transposable à d'autres milieux fluviaux peu profonds, pour l'étude des interactions glace-VAS. Le couplage de relevés hydroacoustiques estivaux et de mesures par géoradar pendant l'hiver sur un même site, à résolution comparable, demeure une approche peu explorée, à laquelle la télédétection satellitaire optique ajoute la dimension temporelle de l'englacement. Ce cadre a permis une évaluation empirique initiale des conditions du couvert de glace et de la présence de VAS pendant l'hiver, et commence à préciser les hypothèses de longue date sur le rôle de la glace dans la persistance de

chenaux dépourvus de VAS au LSP (e.g., Morin et Champoux, 2006). Sur le plan méthodologique, l'approche par krigeage bayésien empirique avec régression, qui intègre les temps de propagation de l'onde du géoradar comme variable explicative, offre une solution adaptée pour cartographier l'épaisseur de glace dans les milieux hydrologiquement complexes, sans étalonnage préalable de la vitesse de l'onde radar, à condition de disposer d'un nombre suffisant de forages.

Le caractère exploratoire de ce projet, portant sur les interactions glace-végétation jusqu'ici peu documentées au LSP, laisse entrevoir plusieurs pistes de recherche. Une caractérisation approfondie de l'épaisseur de glace, à l'aide d'un géoradar installé sur un drone ou en collaboration avec la Garde côtière canadienne, permettrait d'étendre la couverture spatiale et d'accéder à des secteurs inaccessibles en motoneige en raison de conditions de glace variables et dangereuses. Le suivi des conditions hydrodynamiques sous le couvert de glace, incluant la production de frasil, ses voies de transport et la déviation latérale du débit associée à la congestion de glaces en dérive à la première courbe du chenal de navigation, permettrait de tester l'hypothèse selon laquelle les processus d'écoulement sous-glaciels maintiennent les chenaux dépourvus de VAS. L'ajout de variables environnementales printanières et estivales, comme les propriétés hydrologiques et physicochimiques des masses d'eau, aiderait à distinguer un éventuel effet lié à la glace de celui des conditions de la saison de croissance. Enfin, les bas marais, dominés par la végétation émergente, qui sont plus directement exposés aux perturbations physiques liées à la glace et qui offrent une structure d'habitat et des aires d'alevinage essentielles pour la faune aquatique pendant la crue printanière (e.g., de la Chenelière et al., 2014), méritent aussi d'être considérés dans de futurs travaux sur les interactions glace-végétation.

Considérant les pressions croissantes exercées sur les écosystèmes fluviaux-lacustres (Hudon et al., 2018; Botrel et Maranger, 2023), le rôle éventuel des conditions du couvert de glace sur la VAS soulève des enjeux plus larges, notamment pour la conservation des habitats aquatiques littoraux. Le déclin des herbiers au LSP a engendré des répercussions en cascade sur les niveaux trophiques supérieurs, dont l'effondrement du stock de perchaude, un des exemples les plus marquants (Giacomazzo et al., 2020; Magnan et al., 2022). Dans un contexte de changements climatiques susceptibles de diminuer la durée d'englacement et de modifier l'intensité du régime des crues printanières (Rondeau-Genesse, 2020; Woolway et al., 2020), la réponse de la VAS à ces modifications déterminera en partie sa distribution spatiale et sa capacité à se maintenir au LSP.

RÉFÉRENCES

Adamec, L. (2018). Ecophysiological characteristics of turions of aquatic plants: A review. Aquatic Botany, 148, 64-77. https://doi.org/10.1016/j.aquabot.2018.04.011

Adamec, L., Kučerová, A., & Janeček, Š. (2020). Mineral nutrients, photosynthetic pigments and storage carbohydrates in turions of 21 aquatic plant species. Aquatic Botany, 165, 103238. https://doi.org/10.1016/j.aquabot.2020.103238

Adams, W. P., & Roulet, N. T. (1980). Illustration of the Roles of Snow in the Evolution of the Winter Cover of a Lake. ARCTIC, 33(1), 100-116. https://doi.org/10.14430/arctic2550

Akselrud, C. I. A. (2024). Random forest regression models in ecology: Accounting for messy biological data and producing predictions with uncertainty. Fisheries Research, 280, 107161. https://doi.org/10.1016/j.fishres.2024.107161

Annan, A. P., Diamanti, N., Redman, J. D., & Jackson, S. R. (2016). Ground-penetrating radar for assessing winter roads. Geophysics, 81(1), WA101-WA109. https://doi.org/10.1190/geo2015-0138.1

Armellin, A. (2006). Impacts of fluctuating water levels on herpetofauna. In A. Talbot (Ed.), Water availability issues for the St. Lawrence River: An environmental synthesis (pp. 71–81). Environment Canada.

Arp, C. D., Engram, M., Bondurant, A. C., & Drew, K. A. (2022). Unusually thick freshwater ice and its impacts on aquatic resources in the National Petroleum Reserve in Alaska (NPR-A) during the winter of 2020–2021. Arctic Science, 9(2), 497-505. https://doi.org/10.1139/as-2022-0027

Arthaud, F., Toury, J., Romestaing, C., & Bornette, G. (2021). Photosynthetic and morphological traits control aquatic plant distribution according to light stress. Evolutionary Ecology, 35(5), 739-760. https://doi.org/10.1007/s10682-021-10134-9

Ashton, G. D. (Ed.). (1986). River and lake ice engineering. Water Resources Publications.

Assani, A. A. (2023). Comparison of spatio-temporal variability of daily maximum flows in cold-season (winter and spring) in Southern Quebec (Canada). Hydrology, 10(2), 44. https://doi.org/10.3390/hydrology10020044

Barbe, J. (1984). Les végétaux aquatiques : données biologiques et écologiques. Clés de détermination des macrophytes de France. Bulletin français de pisciculture, (292-293), 1-42. https://doi.org/10.1051/kmae:1984001

Bastien, R. (1976). Le détachement de la couverture de glace du Lac Saint-Pierre – coté sud: comment et pourquoi. Service d'ingénierie et de contrôle des glaces, Garde côtière canadienne

Beckers, J. F., Casey, J. A., & Haas, C. (2017). Retrievals of lake ice thickness from great slave lake and great bear lake using CryoSat-2. IEEE Transactions on Geoscience and Remote Sensing, 55(7), 3708-3720. https://doi.org/10.1109/TGRS.2017.2677583

Berrar, D. (2019). Cross-validation. In S. Ranganathan, M. Gribskov, K. Nakai, & C. Schönbach (Eds.), Encyclopedia of bioinformatics and computational biology (pp. 542-545). Academic Press. https://doi.org/10.1016/B978-0-12-809633-8.20349-X

Binzer, T., Sand-Jensen, K., & Middelboe, A. L. (2006). Community photosynthesis of aquatic macrophytes. Limnology and Oceanography, 51(6), 2722-2733. https://doi.org/10.4319/lo.2006.51.6.2722

Block, B. D., Denfeld, B. A., Stockwell, J. D., Flaim, G., Grossart, H. P. F., Knoll, L. B., ... & Hampton, S. E. (2019). The unique methodological challenges of winter limnology. Limnology and Oceanography: Methods, 17(1), 42-57. https://doi.org/10.1002/lom3.10295

Bornette, G., & Puijalon, S. (2009). Macrophytes: Ecology of aquatic plants. In eLS. John Wiley & Sons. https://doi.org/10.1002/9780470015902.a0020475

Botrel, M., & Maranger, R. (2023). Global historical trends and drivers of submerged aquatic vegetation quantities in lakes. Global Change Biology, 29(9), 2493-2509. https://doi.org/10.1111/gcb.16619

Botrel, M., Hudon, C., Biron, P. M., & Maranger, R. (2023). Combining quadrat, rake, and echosounding to estimate submerged aquatic vegetation biomass at the ecosystem scale. Limnology and Oceanography: Methods, 21(4), 192-208. https://doi.org/10.1002/lom3.10539

Botrel, M., Hudon, C., Heffernan, J. B., Biron, P. M., & Maranger, R. (2022). Climate-driven variations in nitrogen retention from a riverine submerged aquatic vegetation meadow. Water Resources Research, 58(10), e2022WR032678. https://doi.org/10.1029/2022WR032678

Bradford, J. H., Harper, J. T., & Brown, J. (2009). Complex dielectric permittivity measurements from ground-penetrating radar data to estimate snow liquid water content in the pendular regime. Water resources research, 45(8). https://doi.org/10.1029/2008WR007341

Bramburger, A. J., Ozersky, T., Silsbe, G. M., Crawford, C. J., Olmanson, L. G., & Shchapov, K. (2023). The not-so-dead of winter: underwater light climate and primary productivity under snow and ice cover in inland lakes. Inland Waters, 13(1), 1-12. https://doi.org/10.1080/20442041.2022.2102870

Breiman, L. (2001). Random forests. Machine Learning, 45(1), 5-32. https://doi.org/10.1023/A:1010933404324

Bush, E., & Lemmen, D. S. (Eds.). (2019). Canada's changing climate report. Government of Canada. https://changingclimate.ca/CCCR2019/

Callaghan, D. T., Blanchfield, P. J., & Cott, P. A. (2016). Lake trout (Salvelinus namaycush) spawning habitat in a northern lake: the role of wind and physical characteristics on habitat quality. Journal of Great Lakes Research, 42(2), 299-307. https://doi.org/10.1016/j.jglr.2015.07.001

Carmignani, J. R., & Roy, A. H. (2017). Ecological impacts of winter water level drawdowns on lake littoral zones: a review. Aquatic Sciences, 79(4), 803-824. https://doi.org/10.1007/s00027-017-0549-9

Chambers, P. A., Lacoul, P., Murphy, K. J., & Thomaz, S. M. (2008). Global diversity of aquatic macrophytes in freshwater. Hydrobiologia, 595(1), 9-26. https://doi.org/10.1007/s10750-007-9154-6

Chambers, P. A., Prepas, E. E., Hamilton, H. R., & Bothwell, M. L. (1991). Current velocity and its effect on aquatic macrophytes in flowing waters. Ecological Applications, 1(3), 249-257. https://doi.org/10.2307/1941754

Chicco, D., Warrens, M. J., & Jurman, G. (2021). The coefficient of determination R-squared is more informative than SMAPE, MAE, MAPE, MSE and RMSE in regression analysis evaluation. PeerJ Computer Science, 7, e623. https://doi.org/10.7717/peerj-cs.623

Chowdhury, E. H., Hassan, Q. K., Achari, G., & Gupta, A. (2017). Use of bathymetric and LiDAR data in generating digital elevation model over the Lower Athabasca River Watershed in Alberta, Canada. Water, 9(1), 19. https://doi.org/10.3390/w9010019

Clamen, M., & Macfarlane, D. (2018). Plan 2014: The historical evolution of lake ontario–st. lawrence river regulation. Canadian Water Resources Journal/Revue canadienne des ressources hydriques, 43(4), 416-431. https://doi.org/10.1080/07011784.2018.1475263

Clermont, M., Kinnard, C., Dubé-Richard, D., Campeau, S., Bordeleau, P. A., de Grandpre, A., ... & Roy, A. (2023). Using remote sensing to assess how intensive agriculture impacts the turbidity of a fluvial lake floodplain. Journal of Great Lakes Research, 49(6), 102240. https://doi.org/10.1016/j.jglr.2023.102240

Cohen, J. (1960). A coefficient of agreement for nominal scales. Educational and Psychological Measurement, 20(1), 37-46. https://doi.org/10.1177/001316446002000010

Congalton, R. G., & Green, K. (2019). Assessing the accuracy of remotely sensed data: principles and practices. CRC press. https://doi.org/10.1201/9780429052729

Cornacchia, L., Wharton, G., Davies, G., Grabowski, R. C., Temmerman, S., Van Der Wal, D., ... & Van De Koppel, J. (2020). Self-organization of river vegetation leads to emergent buffering of river flows and water levels. Proceedings of the Royal Society B, 287(1931), 20201147. https://doi.org/10.1098/rspb.2020.1147

Côté, J. P., & Morin, J. (2007). Principales interventions humaines survenues dans le fleuve Saint-Laurent entre Montréal et Québec au 20e siecle: 1907–2005. Rapp. Tech. RT, 141, 65. https://doi.org/10.13140/RG.2.2.28986.03523

Crossley, M. N., Dennison, W. C., Williams, R. R., & Wearing, A. H. (2002). The interaction of water flow and nutrients on aquatic plant growth. Hydrobiologia, 489(1), 63-70. https://doi.org/10.1023/A:1023298302557

Cunjak, R. A., Prowse, T. D., & Parrish, D. L. (1998). Atlantic salmon (Salmo salar) in winter:" the season of parr discontent"?. Canadian Journal of Fisheries and Aquatic Sciences, 55(S1), 161-180. https://doi.org/10.1139/d98-008

Curtarelli, M., Leão, J., Ogashawara, I., Lorenzzetti, J., & Stech, J. (2015). Assessment of spatial interpolation methods to map the bathymetry of an Amazonian hydroelectric reservoir to aid in decision making for water management. ISPRS International Journal of Geo-Information, 4(1), 220-235. https://doi.org/10.3390/ijgi4010220

Cutler, D. R., Edwards Jr, T. C., Beard, K. H., Cutler, A., Hess, K. T., Gibson, J., & Lawler, J. J. (2007). Random forests for classification in ecology. Ecology, 88(11), 2783-2792. https://doi.org/10.1890/07-0539.1

de Grandpré, A., Kinnard, C., & Bertolo, A. (2022). Open-source analysis of submerged aquatic vegetation cover in complex waters using high-resolution satellite remote sensing: An adaptable framework. Remote Sensing, 14(2), 267. https://doi.org/10.3390/rs14020267

de la Chenelière, V., Brodeur, P., & Mingelbier, M. (2014). Restauration des habitats du lac Saint-Pierre : un prérequis au rétablissement de la perchaude. Le Naturaliste canadien, 138(2), 50–61. https://doi.org/10.7202/1025070ar

Döll, P., & Zhang, J. (2010). Impact of climate change on freshwater ecosystems: a global-scale analysis of ecologically relevant river flow alterations. Hydrology and Earth System Sciences, 14(5), 783-799. https://doi.org/10.5194/hess-14-783-2010

Doyle, R. D. (2001). Effects of waves on the early growth of Vallisneria americana. Freshwater Biology, 46(3), 389-397. https://doi.org/10.1046/j.1365-2427.2001.00668.x

Drusch, M., Del Bello, U., Carlier, S., Colin, O., Fernandez, V., Gascon, F., ... & Bargellini, P. (2012). Sentinel-2: ESA's optical high-resolution mission for GMES operational services. Remote Sensing of Environment, 120, 25-36. https://doi.org/10.1016/j.rse.2011.11.026

Duarte, C. M. (1995). Submerged aquatic vegetation in relation to different nutrient regimes. Ophelia, 41(1), 87-112. https://doi.org/10.1080/00785236.1995.10422039

Duguay, C. R., Bernier, M., Gauthier, Y., & Kouraev, A. (2015). Remote sensing of lake and river ice. Remote sensing of the cryosphere, 273-306. https://doi.org/10.1002/9781118368909.ch12

Environment and Climate Change Canada (ECCC). (n.d.-a). 1981–2010 Climate Normals & Averages: Pierreville, Quebec (Station ID 7026043) [Data set]. Government of Canada. https://climate.weather.gc.ca/climate_normals/results_1981_2010_e.html?stnID=7026043

Environment and Climate Change Canada (ECCC). (n.d.-b). Historical daily climate data: Lac Saint-Pierre, Quebec (Station ID 701LP0N) [Data set]. Government of Canada. https://climate.weather.gc.ca/historical_data/search_historic_data_e.html?stnID=701LP0N

Evans, J. S., & Cushman, S. A. (2009). Gradient modeling of conifer species using random forests. Landscape Ecology, 24(5), 673-683. https://doi.org/10.1007/s10980-009-9341-0

Fisheries and Oceans Canada. (n.d.). Water levels station Lac Saint-Pierre, Quebec (Station ID 15975) [Data set]. Canadian Hydrographic Service, Government of Canada. https://www.marees.gc.ca/fr/stations/15975

Fisheries and Oceans Canada. (2018). Canadian Hydrographic Service non-navigational (NONNA) bathymetric data [Data set]. Government of Canada. https://open.canada.ca/data/en/dataset/d3881c4c-650d-4070-bf9b-1e00aabf0a1d

Frenette, J. J., Arts, M. T., & Morin, J. (2003). Spectral gradients of downwelling light in a fluvial lake (Lake Saint-Pierre, St-Lawrence River). Aquatic Ecology, 37(1), 77-85. https://doi.org/10.1023/A:1022133530244

Frenette, J. J., Arts, M. T., Morin, J., Gratton, D., & Martin, C. (2006). Hydrodynamic control of the underwater light climate in fluvial Lac Saint-Pierre. Limnology and Oceanography, 51(6), 2632-2645. https://doi.org/10.4319/lo.2006.51.6.2632

Fu, H., Liu, Z., Guo, X., & Cui, H. (2018). Double-frequency ground penetrating radar for measurement of ice thickness and water depth in rivers and canals: Development, verification and application. Cold Regions Science and Technology, 154, 85-94. https://doi.org/10.1016/j.coldregions.2018.06.017

Galley, R. J., Trachtenberg, M., Langlois, A., Barber, D. G., & Shafai, L. (2009). Observations of geophysical and dielectric properties and ground penetrating radar signatures for discrimination of snow, sea ice and freshwater ice thickness. Cold Regions Science and Technology, 57(1), 29-38. https://doi.org/10.1016/j.coldregions.2009.01.003

Giacomazzo, M., Bertolo, A., Brodeur, P., Massicotte, P., Goyette, J. O., & Magnan, P. (2020). Linking fisheries to land use: How anthropogenic inputs from the watershed shape fish habitat quality. Science of The Total Environment, 717, 135377. https://doi.org/10.1016/j.scitotenv.2019.135377

Gorelick, N., Hancher, M., Dixon, M., Ilyushchenko, S., Thau, D., & Moore, R. (2017). Google Earth Engine: Planetary-scale geospatial analysis for everyone. Remote Sensing of Environment, 202, 18-27. https://doi.org/10.1016/j.rse.2017.06.031

Gratton, L., & Dubreuil, C. (1990). Portrait de la végétation et de la flore du Saint-Laurent. Ministère de l'Environnement du Québec, Direction de la conservation et du patrimoine écologique.

Greenwell, B. M. (2017). pdp: An R package for constructing partial dependence plots. The R Journal, 9(1), 421–436. https://doi.org/10.32614/RJ-2017-016

Gregorutti, B., Michel, B., & Saint-Pierre, P. (2017). Correlation and variable importance in random forests. Statistics and Computing, 27(3), 659-678. https://doi.org/10.1007/s11222-016-9646-1

Hall, D. K., & Riggs, G. A. (2007). Accuracy assessment of the MODIS snow products. Hydrological Processes: An International Journal, 21(12), 1534-1547. https://doi.org/10.1002/hyp.6715

Hall, D. K., Riggs, G. A., & Salomonson, V. V. (1995). Development of methods for mapping global snow cover using moderate resolution imaging spectroradiometer data. Remote sensing of Environment, 54(2), 127-140. https://doi.org/10.1016/0034-4257(95)00137-P

Helminen, J., Linnansaari, T., Bruce, M., Dolson-Edge, R., & Curry, R. A. (2019). Accuracy and precision of low-cost echosounder and automated data processing software for habitat mapping in a large river. Diversity, 11(7), 116. https://doi.org/10.3390/d11070116

Hicks, F. (2009). An overview of river ice problems: CRIPE07 guest editorial. Cold Regions Science and Technology, 55(2), 175-185. https://doi.org/10.1016/j.coldregions.2008.09.006

Hodson, T. O. (2022). Root mean square error (RMSE) or mean absolute error (MAE): When to use them or not. Geoscientific Model Development Discussions, 2022, 1-10. https://doi.org/10.5194/gmd-15-5481-2022

Hudon, C. (1997). Impact of water level fluctuations on St. Lawrence River aquatic vegetation. Canadian Journal of Fisheries and Aquatic Sciences, 54(12), 2853-2865. https://doi.org/10.1139/f97-201

Hudon, C., & Carignan, R. (2008). Cumulative impacts of hydrology and human activities on water quality in the St. Lawrence River (Lake Saint-Pierre, Quebec, Canada). Canadian Journal of Fisheries and Aquatic Sciences, 65(6), 1165-1180. https://doi.org/10.1139/F08-069

Hudon, C., Cattaneo, A., Tourville Poirier, A. M., Brodeur, P., Dumont, P., Mailhot, Y., ... & de Lafontaine, Y. (2012). Oligotrophication from wetland epuration alters the riverine trophic network and carrying capacity for fish. Aquatic Sciences, 74(3), 495-511. https://doi.org/10.1007/s00027-011-0243-2

Hudon, C., Jean, M., & Létourneau, G. (2018). Temporal (1970–2016) changes in human pressures and wetland response in the St. Lawrence River (Québec, Canada). Science of the Total Environment, 643, 1137-1151. https://doi.org/10.1016/j.scitotenv.2018.06.080

Hudon, C., Lalonde, S., & Gagnon, P. (2000). Ranking the effects of site exposure, plant growth form, water depth, and transparency on aquatic plant biomass. Canadian Journal of Fisheries and Aquatic Sciences, 57(S1), 31-42. https://doi.org/10.1139/f99-232

Huo, P., Lu, P., Cheng, B., Zhang, L., Wang, Q., & Li, Z. (2022). Monitoring ice phenology in lake wetlands based on optical satellite data: A case study of Wuliangsu Lake. Water, 14(20), 3307. https://doi.org/10.3390/w14203307

IPCC. (2023). Climate change 2023: Synthesis report. Contribution of Working Groups I, II and III to the Sixth Assessment Report of the Intergovernmental Panel on Climate Change (Core Writing Team, H. Lee, & J. Romero, Eds.). IPCC. https://doi.org/10.59327/IPCC/AR6-9789291691647

Jarvis, J. C., & Moore, K. A. (2008). Influence of environmental factors on Vallisneria americana seed germination. Aquatic Botany, 88(4), 283-294. https://doi.org/10.1016/j.aquabot.2007.12.001

Jobin, B., & Brodeur, P. (2023). Changements de l'occupation du sol de la plaine inondable du lac Saint-Pierre de 1950 à 2016 et perspectives pour la restauration des milieux naturels. Le Naturaliste Canadien, 147(2), 14-26. https://doi.org/10.7202/1100079ar

Kadono, Y. (1988). Germination of the turion of Myriophyllum oguraense Miki. Aquatic Botany, 31(3-4), 355-360. https://doi.org/10.1016/0304-3770(88)90024-1

Kämäri, M., Alho, P., Colpaert, A., & Lotsari, E. (2017). Spatial variation of river-ice thickness in a meandering river. Cold Regions Science and Technology, 137, 17-29. https://doi.org/10.1016/j.coldregions.2017.01.009

Kirillin, G., & Shatwell, T. (2016). Generalized scaling of seasonal thermal stratification in lakes. Earth-Science Reviews, 161, 179-190. https://doi.org/10.1016/j.earscirev.2016.08.008

Kirillin, G., Leppäranta, M., Terzhevik, A., Granin, N., Bernhardt, J., Engelhardt, C., ... & Zdorovennov, R. (2012). Physics of seasonally ice-covered lakes: a review. Aquatic Sciences, 74(4), 659-682. https://doi.org/10.1007/s00027-012-0279-y

Kirk, J. T. O. (1994). Light and photosynthesis in aquatic ecosystems (2nd ed.). Cambridge University Press.

Knadel, M., Thomsen, A., Schelde, K., & Greve, M. H. (2015). Soil organic carbon and particle sizes mapping using vis–NIR, EC and temperature mobile sensor platform. Computers and Electronics in Agriculture, 114, 134-144. https://doi.org/10.1016/j.compag.2015.03.013

Krivoruchko, K. (2012). Empirical bayesian kriging. ArcUser Fall, 6(10), 1145.

Krivoruchko, K., & Gribov, A. (2019). Evaluation of empirical Bayesian kriging. Spatial Statistics, 32, 100368. https://doi.org/10.1016/j.spasta.2019.100368

La Violette, N. (2004). Les lacs fluviaux du Saint-Laurent: hydrologie et modifications humaines. Le Naturaliste Canadien, 128(1), 98-104.

Laporte, M., Gagnon, M. J., Bégin, P. N., Brodeur, P., Paquin, É., Mainguy, J., ... & Pouliot, R. (2023). Déclin de la végétation aquatique submergée au lac Saint-Pierre de 2002 à 2021. Le Naturaliste canadien, 147(2), 69-81. https://doi.org/10.7202/1105486ar

Lauridsen, T. L., & Lodge, D. M. (1996). Avoidance by Daphnia magna of fish and macrophytes: Chemical cues and predator-mediated use of macrophyte habitat. Limnology and Oceanography, 41(4), 794-798. https://doi.org/10.4319/lo.1996.41.4.0794

Legendre, P., & Legendre, L. (2012). Numerical ecology (3rd ed.). Elsevier.

Leppäranta, M. (2015). Freezing of Lakes and the Evolution of their Ice Cover. Springer. https://doi.org/10.1007/978-3-642-29081-7

Lévesque, A., Bissonnette, J. F., Vansintjan, A., & Dupras, J. (2024). Conflicting perspectives on ecosystem conservation in a cultivated floodplain: The role of science and the challenge of pluralism in decision-making in Lac Saint-Pierre (Quebec, Canada). Environmental Policy and Governance, 34(5), 476-489. https://doi.org/10.1002/eet.2095

Liu, C., Huang, H., Hui, F., Zhang, Z., & Cheng, X. (2021). Fine-resolution mapping of pan-arctic lake ice-off phenology based on dense sentinel-2 time series data. Remote Sensing, 13(14), 2742. https://doi.org/10.3390/rs13142742

Lind, L., Nilsson, C., Polvi, L. E., & Weber, C. (2014). The role of ice dynamics in shaping vegetation in flowing waters. Biological Reviews, 89(4), 791-804. https://doi.org/10.1111/brv.12077

Lodge, D. M. (1991). Herbivory on freshwater macrophytes. Aquatic Botany, 41(1-3), 195-224. https://doi.org/10.1016/0304-3770(91)90044-6

Madsen, J. D., Chambers, P. A., James, W. F., Koch, E. W., & Westlake, D. F. (2001). The interaction between water movement, sediment dynamics and submersed macrophytes. Hydrobiologia, 444(1), 71-84. https://doi.org/10.1023/A:1017520800568

Magnan, P. (2002). Avis scientifique sur l'état du stock de perchaudes au lac Saint-Pierre, les indicateurs biologiques utilisés pour effectuer son suivi et la pertinence de protéger la période de fraye de façon partielle ou totale. Chaire de recherche en écologie des eaux douces, Université du Québec à Trois-Rivières. Trois-Rivières.

Magnan, P., Brodeur, P., Paquin, É., Vachon, N., Paradis, Y., Dumont, P., & Mailhot, Y. (2017). État du stock de perchaudes du lac Saint-Pierre en 2016. Comité scientifique sur la gestion de la perchaude du lac Saint-Pierre. Ministère des Forêts, de la Faune et des Parcs.

Magnan, P., Paquin, É., Brodeur, P., Paradis, Y., Vachon, N., Dumont, P., & Mailhot, Y. (2022). État du stock de perchaudes du lac Saint-Pierre et du secteur pont Laviolette–Saint-Pierre-les-Becquets en 2021. Comité scientifique sur la gestion de la perchaude du lac Saint-Pierre. Ministère des Forêts, de la Faune et des Parcs.

Mailhot, Y., Dumont, P., Paradis, Y., Brodeur, P., Vachon, N., Mingelbier, M., ... & Magnan, P. (2015). Yellow perch (Perca flavescens) in the St. Lawrence River (Québec, Canada): Population dynamics and management in a river with contrasting pressures. In Biology of perch (pp. 101-147). CRC Press.

Main-Knorn, M., Pflug, B., Louis, J., Debaecker, V., Müller-Wilm, U., & Gascon, F. (2017, October). Sen2Cor for sentinel-2. In Image and signal processing for remote sensing XXIII (Vol. 10427, pp. 37-48). SPIE. https://doi.org/10.1117/12.2278218

Marcogliese, D. J., Blaise, C., Cyr, D., de Lafontaine, Y., Fournier, M., Gagné, F., Gagnon, C., & Hudon, C. (2015). Effects of a major municipal effluent on the St. Lawrence River: A case study. AMBIO, 44(4), 257-274. https://doi.org/10.1007/s13280-014-0577-9

Marion, L., & Paillisson, J. M. (2003). A mass balance assessment of the contribution of floating-leaved macrophytes in nutrient stocks in an eutrophic macrophyte-dominated lake. Aquatic Botany, 75(3), 249-260. https://doi.org/10.1016/S0304-3770(02)00177-8

McFeeters, S. K. (1996). The use of the Normalized Difference Water Index (NDWI) in the delineation of open water features. International journal of remote sensing, 17(7), 1425-1432. https://doi.org/10.1080/01431169608948714

MDDEFP (Ministère du Développement durable, de l'Environnement, de la Faune et des Parcs). (2013). Le lac Saint-Pierre : un joyau à restaurer. Gouvernement du Québec. https://www.environnement.gouv.qc.ca/eau/lac-st-pierre/doc-synthese.pdf

Michel, B., & Ramseier, R. O. (1971). Classification of river and lake ice. Canadian Geotechnical Journal, 8(1), 36-45. https://doi.org/10.1139/t71-004

Midwood, J. D., Tang, R. W., Doka, S. E., & Costa, J. M. G. (2021). Comparison of approaches for modelling submerged aquatic vegetation in the Toronto and Region Area of Concern. Journal of Great Lakes Research, 47(2), 395-404. https://doi.org/10.1016/j.jglr.2020.08.019

Morin, J., & Champoux, O. (2006). Integrated modelling of the physical processes and habitats of the St. Lawrence River. In A. Talbot (Ed.), *Water availability issues for the St. Lawrence River: An environmental synthesis* (pp. 24-39). Environment Canada.

Morin, J., & Côté, J. P. (2003). Modifications anthropiques sur 150 ans au lac Saint-Pierre: une fenêtre sur les transformations de l'écosystème du Saint-Laurent. VertigO-la revue électronique en sciences de l'environnement, (4-3). https://doi.org/10.4000/vertigo.3867

Morin, J., Leclerc, M., Secretan, Y., & Boudreau, P. (2000). Integrated two-dimensional macrophytes-hydrodynamic modeling. Journal of Hydraulic Research, 38(3), 163-172. https://doi.org/10.1080/00221680009498334

Morse, B. (2001). Winter navigation on the St. Lawrence River. In Proceedings of the International Conference on Port and Ocean Engineering under Arctic Conditions. Ottawa, Canada.

Murfitt, J., & Duguay, C. R. (2021). 50 years of lake ice research from active microwave remote sensing: Progress and prospects. Remote Sensing of Environment, 264, 112616. https://doi.org/10.1016/j.rse.2021.112616

Murfitt, J. C., Brown, L. C., & Howell, S. E. (2018). Estimating lake ice thickness in Central Ontario. Plos One, 13(12), e0208519. https://doi.org/10.1371/journal.pone.0208519

Navico Inc. (2014). BioBase-Automate mapping user reference guide. Navico Inc.

Nelson, S. A., Cheruvelil, K. S., & Soranno, P. A. (2006). Satellite remote sensing of freshwater macrophytes and the influence of water clarity. Aquatic Botany, 85(4), 289-298. https://doi.org/10.1016/j.aquabot.2006.06.003

Newete, S. W., & Byrne, M. J. (2016). The capacity of aquatic macrophytes for phytoremediation and their disposal with specific reference to water hyacinth. Environmental Science and Pollution Research, 23(11), 10630-10643. https://doi.org/10.1007/s11356-016-6329-6

Newman, R. M. (1991). Herbivory and detritivory on freshwater macrophytes by invertebrates: A review. Journal of the North American Benthological Society, 10(2), 89-114. https://doi.org/10.2307/1467571

Nichols, S. A. (1999). Distribution and habitat descriptions of Wisconsin lake plants (No. 96). Wisconsin Geological and Natural History Survey.

Nicodemus, K. K., Malley, J. D., Strobl, C., & Ziegler, A. (2010). The behaviour of random forest permutation-based variable importance measures under predictor correlation. BMC bioinformatics, 11(1), 110. https://doi.org/10.1186/1471-2105-11-110

Njoku, E. A., Akpan, P. E., Effiong, A. E., & Babatunde, I. O. (2023). The effects of station density in geostatistical prediction of air temperatures in Sweden: A comparison of two interpolation techniques. Resources, Environment and Sustainability, 11, 100092. https://doi.org/10.1016/j.resenv.2022.100092

Oliver, M. A., & Webster, R. (2014). A tutorial guide to geostatistics: Computing and modelling variograms and kriging. Catena, 113, 56-69. https://doi.org/10.1016/j.catena.2013.09.006

Orth, R. J., Dennison, W. C., Lefcheck, J. S., Gurbisz, C., Hannam, M., Keisman, J., ... & Wilcox, D. J. (2017). Submersed aquatic vegetation in Chesapeake Bay: sentinel species in a changing world. BioScience, 67(8), 698-712. https://doi.org/10.1093/biosci/bix058

Pan, J., Shen, H. T., & Jasek, M. (2020). Anchor ice effects on river hydraulics. Cold Regions Science and Technology, 174, 103062. https://doi.org/10.1016/j.coldregions.2020.103062

Parent, M., & Occhietti, S. (1988). Late Wisconsinan deglaciation and Champlain sea invasion in the St. Lawrence valley, Québec. Géographie physique et Quaternaire, 42(3), 215-246. https://doi.org/10.7202/032734ar

Pearce, R. S. (2001). Plant freezing and damage. Annals of botany, 87(4), 417-424. https://doi.org/10.1006/anbo.2000.1352

Peres-Neto, P. R., Legendre, P., Dray, S., & Borcard, D. (2006). Variation partitioning of species data matrices: Estimation and comparison of fractions. Ecology, 87(10), 2614-2625. https://doi.org/10.1890/0012-9658(2006)87[2614:VPOSDM]2.0.CO;2

Pouw, A. F., Kheyrollah Pour, H., & MacLean, A. (2023). Mapping snow depth on Canadian sub-arctic lakes using ground-penetrating radar. The Cryosphere, 17(6), 2367-2385. https://doi.org/10.5194/tc-17-2367-2023

Prowse, T. D., & Gridley, N. C. (Eds.). (1993). Environmental aspects of river ice. National Hydrology Research Institute.

Puijalon, S., Bornette, G., & Sagnes, P. (2005). Adaptations to increasing hydraulic stress: morphology, hydrodynamics and fitness of two higher aquatic plant species. Journal of Experimental Botany, 56(412), 777-786. https://doi.org/10.1093/jxb/eri063

Razy, A., Milrad, S. M., Atallah, E. H., & Gyakum, J. R. (2012). Synoptic-scale environments conducive to orographic impacts on cold-season surface wind regimes at Montreal, Quebec. Journal of applied meteorology and climatology, 51(3), 598-616. https://doi.org/10.1175/JAMC-D-11-0142.1

Renman, G. (1989). Life histories of two clonal populations of Stratiotes aloides L. Hydrobiologia, 185(3), 211-222. https://doi.org/10.1007/BF00036609

Richard, M., & Morse, B. (2008). Multiple frazil ice blockages at a water intake in the St. Lawrence River. Cold Regions Science and Technology, 53(2), 131-149. https://doi.org/10.1016/j.coldregions.2007.10.003

Roberts, D. R., Bahn, V., Ciuti, S., Boyce, M. S., Elith, J., Guillera-Arroita, G., ... & Dormann, C. F. (2017). Cross-validation strategies for data with temporal, spatial, hierarchical, or phylogenetic structure. Ecography, 40(8), 913-929. https://doi.org/10.1111/ecog.02881

Rondeau-Genesse, G. (2020). Impact des changements climatiques sur les facteurs hydroclimatiques influençant les inondations et les processus d'érosion des berges du tronçon fluvial du Saint-Laurent. Ouranos.

Rowan, G. S., & Kalacska, M. (2021). A review of remote sensing of submerged aquatic vegetation for non-specialists. Remote Sensing, 13(4), 623. https://doi.org/10.3390/rs13040623

Rudstam, L. G., VanDeValk, A. J., Adams, C. M., Coleman, J. T. H., Forney, J. L., & Richmond, M. E. (2004). Cormorant predation and the population dynamics of walleye and yellow perch in Oneida Lake. Ecological Applications, 14(1), 149-163. https://doi.org/10.1890/03-5010

Rybicki, N. B., & Carter, V. (2002). Light and temperature effects on the growth of wild celery and hydrilla. Journal of Aquatic Plant Management, 40(2), 92-99.

Saint-Laurent, D., Hähni, M., & Barrett, S. A. (2010). Analyse des sédiments contaminés de la portion sud-ouest du Lac Saint-Pierre (Québec, Canada). Revue des sciences de l'eau, 23(2), 119-131. https://doi.org/10.7202/039904ar

Scalabrini, P., & Morse, B. (2021). An early warning ice management system for the Saint Lawrence River: Increasing the reliability of winter navigation to the Port of Montreal. In Paper Presented at the 21st Workshop on the Hydraulics of Ice-Covered Rivers. https://cripe.ca/publications/proceedings/workshop-21

Schneider, S. C., Lawniczak, A. E., Picińska-Faltynowicz, J., & Szoszkiewicz, K. (2012). Do macrophytes, diatoms and non-diatom benthic algae give redundant information? Results from a case study in Poland. Limnologica, 42(3), 204-211. https://doi.org/10.1016/j.limno.2011.12.001

Scrimgeour, G. J., Prowse, T. D., Culp, J. M., & Chambers, P. A. (1994). Ecological effects of river ice break-up: a review and perspective. Freshwater Biology, 32(2), 261-275. https://doi.org/10.1111/j.1365-2427.1994.tb01125.x

Sensors & Software Inc. (2013). IceMap user's guide. Sensors & Software Inc.

Søndergaard, M., Lauridsen, T. L., Johansson, L. S., & Jeppesen, E. (2017). Nitrogen or phosphorus limitation in lakes and its impact on phytoplankton biomass and submerged macrophyte cover. Hydrobiologia, 795(1), 35-48. https://doi.org/10.1007/s10750-017-3110-x

Spencer, W. E., & Wetzel, R. G. (1993). Acclimation of photosynthesis and dark respiration of a submersed angiosperm beneath ice in a temperate lake. Plant Physiology, 101(3), 985-991. https://doi.org/10.1104/pp.101.3.985

Stevens, C. W., Moorman, B. J., Solomon, S. M., & Hugenholtz, C. H. (2009). Mapping subsurface conditions within the near-shore zone of an Arctic delta using ground penetrating radar. Cold regions science and technology, 56(1), 30-38. https://doi.org/10.1016/j.coldregions.2008.09.005

Stickler, M., & Alfredsen, K. T. (2009). Anchor ice formation in streams: a field study. Hydrological Processes: An International Journal, 23(16), 2307-2315. https://doi.org/10.1002/hyp.7349

Stocks, J. R., Rodgers, M. P., Pera, J. B., & Gilligan, D. M. (2019). Monitoring aquatic plants: An evaluation of hydroacoustic, on-site digitising and airborne remote sensing techniques. Knowledge & Management of Aquatic Ecosystems, (420), 27. https://doi.org/10.1051/kmae/2019016

Talbot, A. (Ed.). (2006). Water availability issues for the St. Lawrence River: An environmental synthesis. Environment Canada.

Tarrio, K., Tang, X., Masek, J. G., Claverie, M., Ju, J., Qiu, S., ... & Woodcock, C. E. (2020). Comparison of cloud detection algorithms for Sentinel-2 imagery. Science of Remote Sensing, 2, 100010. https://doi.org/10.1016/j.srs.2020.100010

Thomaz, S. M., Cardozo, A. L. P., Quirino, B. A., Yofukuji, K. Y., Aleixo, M. H. F., & Fugi, R. (2025). A review of the ecological role of aquatic macrophytes on freshwater fish. Hydrobiologia, 1-34. https://doi.org/10.1007/s10750-025-05819-z

Thunnissen, N. W., Collas, F. P. L., Hendriks, A. J., & Leuven, R. S. E. W. (2019). Effect of shipping induced changes in flow velocity on aquatic macrophytes in intensively navigated rivers. Aquatic Botany, 159, 103145. https://doi.org/10.1016/j.aquabot.2019.103145

Tilling, R. L., Ridout, A., & Shepherd, A. (2018). Estimating Arctic sea ice thickness and volume using CryoSat-2 radar altimeter data. Advances in Space Research, 62(6), 1203-1225. https://doi.org/10.1016/j.asr.2017.10.051

Valavi, R., Elith, J., Lahoz-Monfort, J. J., & Guillera-Arroita, G. (2019). blockCV: An R package for generating spatially or environmentally separated folds for k-fold cross-validation of species distribution models. Methods in Ecology and Evolution, 10(2), 225–232. https://doi.org/10.1111/2041-210X.13107

Valley, R. D. (2016). Spatial and temporal variation of aquatic plant abundance: Quantifying change. Journal of Aquatic Plant Management, 54, 95-101.

Valley, R. D., Drake, M. T., & Anderson, C. S. (2005). Evaluation of alternative interpolation techniques for the mapping of remotely-sensed submersed vegetation abundance. Aquatic Botany, 81(1), 13-25. https://doi.org/10.1016/j.aquabot.2004.09.002

Valley, R. D., Johnson, M. B., Dustin, D. L., Jones, K. D., Lauenstein, M. R., & Nawrocki, J. (2015). Combining hydroacoustic and point-intercept survey methods to assess aquatic plant species abundance patterns and community dominance. Journal of Aquatic Plant Management, 53, 121-129.

Vavrus, S. J., Wynne, R. H., & Foley, J. A. (1996). Measuring the sensitivity of southern Wisconsin lake ice to climate variations and lake depth using a numerical model. Limnology and Oceanography, 41(5), 822-831. https://doi.org/10.4319/lo.1996.41.5.0822

Vermaat, J. E., Santamaria, L., & Roos, P. J. (2000). Water flow across and sediment trapping in submerged macrophyte beds of contrasting growth form. Fundamental and Applied Limnology, 148(4), 549-562. https://doi.org/10.1127/archiv-hydrobiol/148/2000/549

Viana, D. S., Keil, P., & Jeliazkov, A. (2022). Disentangling spatial and environmental effects: Flexible methods for community ecology and macroecology. Ecosphere, 13(4), e4028. https://doi.org/10.1002/ecs2.4028

Vis, C., Cattaneo, A., & Hudon, C. (2008). Shift from chlorophytes to cyanobacteria in benthic macroalgae along a gradient of nitrate depletion 1. Journal of Phycology, 44(1), 38-44. https://doi.org/10.1111/j.1529-8817.2007.00429.x

Vis, C., Hudon, C., & Carignan, R. (2003). An evaluation of approaches used to determine the distribution and biomass of emergent and submerged aquatic macrophytes over large spatial scales. Aquatic Botany, 77(3), 187-201. https://doi.org/10.1016/S0304-3770(03)00105-0

Vis, C., Hudon, C., Carignan, R., & Gagnon, P. (2007). Spatial analysis of production by macrophytes, phytoplankton and epiphyton in a large river system under different water-level conditions. Ecosystems, 10(2), 293-310. https://doi.org/10.1007/s10021-007-9021-3

Watson, C. J., Mazzei, R., Bourgeois, B., Smedbol, É., Guiraud, N., Félix-Faure, J., ... & Proulx, R. (2024). Towards sustainable agricultural landscapes: Lessons from an interdisciplinary research-based framework applied to the Saint Lawrence floodplain. Basic and Applied Ecology, 80, 11-22. https://doi.org/10.1016/j.baae.2024.07.005

Webster, R., & Oliver, M. A. (2007). Geostatistics for environmental scientists. John Wiley & Sons. https://doi.org/10.1002/9780470517277

Weiss, D. J., Atkinson, P. M., Bhatt, S., Mappin, B., Hay, S. I., & Gething, P. W. (2014). An effective approach for gap-filling continental scale remotely sensed time-series. ISPRS Journal of Photogrammetry and Remote Sensing, 98, 106-118. https://doi.org/10.1016/j.isprsjprs.2014.10.001

Weyhenmeyer, G. A., Obertegger, U., Rudebeck, H., Jakobsson, E., Jansen, J., Zdorovennova, G., ... & Zdorovennov, R. (2022). Towards critical white ice conditions in lakes under global warming. Nature communications, 13(1), 4974. https://doi.org/10.1038/s41467-022-32633-1

Wong, J., Han, L., Bancroft, J., & Stewart, R. (2009). Automatic time-picking of first arrivals on large seismic datasets. CREWES, Univ. Calgary, Calgary, AB, Canada, Tech. Rep, 26, 14.

Woolway, R. I., Kraemer, B. M., Lenters, J. D., Merchant, C. J., O'Reilly, C. M., & Sharma, S. (2020). Global lake responses to climate change. Nature Reviews Earth & Environment, 1(8), 388-403. https://doi.org/10.1038/s43017-020-0067-5

Wright, M. N., & Ziegler, A. (2017). ranger: A fast implementation of random forests for high dimensional data in C++ and R. Journal of Statistical Software, 77, 1-17. https://doi.org/10.18637/jss.v077.i01

Wu, C., Wu, S., Wu, X., Zhang, Y., Feng, K., Zhang, W., & Zhao, Y. (2023). Hydrodynamics affected by submerged vegetation with different flexibility under unidirectional flow. Frontiers in Marine Science, 9, 1041351. https://doi.org/10.3389/fmars.2022.1041351

Yang, Q., Song, K., Wen, Z., Hao, X., & Fang, C. (2019). Recent trends of ice phenology for eight large lakes using MODIS products in Northeast China. International Journal of Remote Sensing, 40(14), 5388-5410. https://doi.org/10.1080/01431161.2019.1579939

Yang, X., Pavelsky, T. M., & Allen, G. H. (2020). The past and future of global river ice. Nature, 577(7788), 69-73. https://doi.org/10.1038/s41586-019-1848-1

Yang, X., Pavelsky, T. M., Bendezu, L. P., & Zhang, S. (2021). Simple method to extract lake ice condition from Landsat images. IEEE Transactions on Geoscience and Remote Sensing, 60, 1-10. https://doi.org/10.1109/TGRS.2021.3088144

Yang, Y., Leppäranta, M., Cheng, B., & Li, Z. (2012). Numerical modelling of snow and ice thicknesses in Lake Vanajavesi, Finland. Tellus A: Dynamic Meteorology and Oceanography, 64(1), 17202. https://doi.org/10.3402/tellusa.v64i0.17202

Yu, W., Wang, L., Ma, X., Li, J., Li, Z., Wang, H., ... & Yu, D. (2025). Restoration of submerged vegetation modulates microbial communities to decrease nitrogen and phosphorus loads in sediment-water systems. Water Research, 269, 122835. https://doi.org/10.1016/j.watres.2024.122835

Zhang, X., Flato, G., Kirchmeier-Young, M., Vincent, L., Wan, H., Wang, X., Rong, R., Fyfe, J., Li, G., & Kharin, V. V. (2019). Changes in temperature and precipitation across Canada. In E. Bush & D. S. Lemmen (Eds.), Canada's changing climate report (pp. 112-193). Government of Canada.